UCLouvain

École polytechnique de Louvain

Myemouse project: Quantifying white matter and myelin loss in rodent brains

Histology validation and a software tool to process data

Authors: **Nicolas Bioul, Eliott Henaut**
Supervisor: **Benoît Macq**
Readers: **Nicolas Delinte, Quentin Dessain, Laurence Dricot, Sébastien Jodogne**
Academic year 2021–2022
Master [120] in Mathematical Engineering

Keywords

corpus callosum, cuprizone, Digital Imaging and Communications in Medicine (DICOM), Microstructure Fingerprinting, Histology, Microstructure, Magnetic Resonance Imaging (MRI), myelin, Neuroimaging Informatics Technology Initiative (NifTi).

Abstract

To this day, there is a need for accurate quantitative non-invasive biomarkers to monitor myelin pathology in vivo and differentiate myelin alterations from other pathological aspects such as inflammation and axonal loss. Magnetic Resonance Imaging (MRI) measurements such as T2, magnetization transfer ratio, and radial diffusivity, which are commonly used, have demonstrated sensitivity but not specificity. The latter can be achieved by registering histology data to MRI. A new Python tool has been developed that easily allows data plug-in from Bruker machines into a novel pipeline that will convert, process and exhibit interesting features from microstructural algorithms. These results have been analysed and confirmed by histology images on the Corpus callosum (CC) of cuprizoned mice during the Myemouse Project led from January 2020 to August 2022. In future studies, this tool may prove reliable in predicting with accuracy myelin loss within small mammal brains.

Contents

Introduction **1**

1 Theoretical background **4**
1.1 Magnetic Resonance Imaging 4
1.1.1 Magnetic Resonance Imaging (MRI) metrics 4
1.1.2 Multi-echo T2 7
1.1.3 Contrast 10
1.2 Diffusion Weighted Magnetic Resonance Imaging 12
1.2.1 Diffusion Imaging Generalities 12
1.2.2 Pulse Gradient Spin Echo 13
1.2.3 Diffusion tensor imaging (DTI) 16
1.3 Microstructural multi-compartment models 18
1.3.1 NODDI 18
1.3.2 Fingerprinting 20
1.4 Elikopy 22
1.5 Artifacts in Magnetic Resonance Imaging 25
1.6 Miniature mouse model 25
1.6.1 Cuprizone model 25
1.6.2 Ethical statement 27
1.7 Histology 28
1.8 Anatomy 30
1.8.1 Decomposing the brain 30
1.8.2 Neuronal grid 35

2 Convert and process pipeline **37**
2.1 Myemouse Project Parameters 37
2.2 Main conversion Pipeline 39
2.2.1 From the machine to organized folders 39
2.2.2 Capturing the essential files 42
2.3 Data correction process 43
2.3.1 Denoising 43
2.3.2 Motion correction 46
2.3.3 Brain extraction 50

2.4 Atlas 54

3 Analysis, comparison and discussion **57**
3.1 Histology Analysis 57
3.1.1 The cingulum problem 57
3.1.2 Time and Diets analysis 62
3.2 DMRI analysis 68
3.2.1 First conclusions 73
3.2.2 DTI 74
3.2.3 NODDI 78
3.2.4 Fingerprinting 83

Conclusion **89**

A brain extraction **101**

B Polynomial interpolation and approximation **102**
B.1 Polynomial interpolation 102
B.1.1 Different interpolations 102
B.1.2 About Lagrange interpolation 104
B.1.3 About Hermite's interpolation 106
B.1.4 Differentiation 107
B.2 $\infty-$norm 107
B.3 2-norm 114
B.3.1 Inner product spaces 114
B.3.2 Best approximation of the 2-norm 115

C Acquisition parameters **120**

D Miscellaneous results **131**
D.1 Cingulum Analysis results 131
D.2 Histology data 135

List of Figures

1 *Where our project lies* 2

1.1 *Proton spin* [9] 4
1.2 *Application of RF-pulse wave on y axis* [72] 5
1.3 *Percentage of proton equilibrium recovery; T1 relaxation* [72] 6
1.4 *Percentage of protons aligned with B_0; T2 relaxation* [72] 6
1.5 *Phase shift: line is the signal before phase shift and dot is the signal after (sum is null)* [72] 7
1.6 *First RF-pulse applied* [72] 8
1.7 *After RF-pulse, the spins are out of phase*[72] 8
1.8 *Second RF-pulse applied in the opposite direction* 8
1.9 *The spins return to equilibrium position* 8
1.10 *T2 curve for 1 line* [72] 9
1.11 *echo T2 multi-line* [72] 10
1.12 *heatMap of TR/ TE from* [26] 11
1.13 *signal influence by TR and TE* 11
1.14 *Contrast following TR and TE: TR and TE short lead to T1 contrast; TR and TE long lead to T2 contast.*[72] 12
1.15 *Factor of b* 14
1.16 *Diffusion's signal* 14
1.17 *Example of Diffusion-weighted EPI brain images ($b = 1000$). Diffusion gradients were applied in the three axes: slice selection (a), frequency coding(b) and phase coding(c). A fourth image (sometimes called trace image) is reconstructed from the combination of the three previous images (d).* 15
1.18 *Summary of DTI parameters from (Gholizadeh et al., 2019) [22]* 17
1.19 *Diffusion models for NODDI in comparison with DTI. NODDI considers constrained diffusion in intra and extra cellular compartments as well as free diffusion in cerebrospinal fluid (CSF). (Barritt et al. 2018)* [4] 19
1.20 *Summary of the Microstructure Fingerprint algorithm modus operandi*[50] . 22
1.21 *The ElikoPy pipeline's key processing phases are shown in this diagram.* [13] 23
1.22 *The ElikoPy toolbox uses the following folder structure.* [13] 24
1.23 *Molecular structure of cuprizone* 26
1.24 *Luxol Fast blue stain on mouse brain* 29
1.25 *Luxol Fast Blue molecule from DiscoFineChem* 29

1.26 *Mouse brain Anatomy* 30
1.27 *The composition of the Neuron grid* 36

2.1 *Timeline summarizing the mice regimes, the MRI acquisition sessions and the histology periods.* 38
2.2 *Multi-shell representation for MRI* 39
2.3 *DtiEpi constant* 40
2.4 *DtiEpi intermittent* 40
2.5 *DtiEpi spiral* 40
2.6 *reverse-enconding* 41
2.7 *Structure diagram* 42
2.8 *first step denoising vs last step denoising* 44
2.9 *The denoising step is essential as it clears all the snowy particles (left image). The right image is therefore ready to be used.* 45
2.10 *Image to be corrected* 49
2.11 *Corrected image* 49
2.12 *Seed location* 50
2.13 *Seed calculation* 51
2.14 *Filling using a function called in* `Mask_Wizard` 51
2.15 *A sequence of Opening/Closing* 52
2.16 *Volume reference unit for opening an closing. Ball of radius=7* 52
2.17 *Mask overlay on data* 53
2.18 *Mask apply on data* 53
2.19 *Distinguishing the ROI on Magnetic Resonance Imaging* 54
2.20 *Volume 179 on acquisition 41 (Group 3, mouse 4 at time 2)* 55
2.21 *CC drawn on MRIcron [52] over Figure* 2.20 55
2.22 *Illustration of the coregistration of two images. The z axis is pointing out of the paper.* 55
2.23 *DTI map, FA-RGB which depicts the general direction (x,y,z) of fibers with one of the three colors (or a mix)* 56
2.24 *Empirical mask (red) and refined mask (blue) on brain slice 179 of acquisition 41.* 56
2.25 *Final CC mask on DTI's RGB map.* 56

3.1 *Isolating the cingulum around the CC on a group 1 control mouse* 58
3.2 *Isolating the cingulum around the CC on a group 3 12 week Cuprizone mouse* 58
3.3 *Analysis protocol on group 1 control mouse cingulum and CC. Red, green and blue correspond with RGB respectfully. Yellow lines represents a basic approximation of the intensity function. The x axis represents the pixels from the image and the y-axis represents the absolute value of RGB intensity* -255 60
3.4 *Difference between Group 1 control and Group 2 Cuprizone 6 weeks, 3 Cuprizone 12 weeks and Group 4 remission mice intensities for RGB with cingulum.* 61

3.5 *Difference between Group 1 control and Group 2 Cuprizone 6 weeks, 3 Cuprizone 12 weeks and Group 4 remission mice intensities for RGB without cingulum.* 61
3.6 *RGB myelin intensity with cingulum* 62
3.7 *RGB myelin intensity without cingulum* 62
3.8 *Legendre approximation of the mean pixel intensity for each group* 64
3.9 *Oriented histology corpus callosum in order to match DW-MRI orientation* 65
3.10 *Segmented histology data in order to visualize difference parts of the CC* . . 65
3.11 *Difference in myelin levels between group 1 and groups 2, 3 and 4 as a function of CC section* 66
3.12 *Time* $T = 1$ *using DTI's* `FA` *map* 69
3.13 *Time* $T = 2$ *using DTI's* `FA` *map* 69
3.14 *Time* $T = 3$ *using DTI's* `FA` *map* 69
3.15 *Mean of anisotropie for all mouse base on FA of DTI* 69
3.16 *Group 1 using DTI's* `FA` *map* 70
3.17 *Group 2 using DTI's* `FA` *map* 70
3.18 *Group 3 using DTI's* `FA` *map* 70
3.19 *Group 4 using DTI's* `FA` *map* 70
3.20 *Mean of anisotropie for all mouse base on FA of DTI* 70
3.21 *Mouse 1 using DTI's* `FA` *map* 71
3.22 *Mouse 5 using DTI's* `FA` *map* 71
3.23 *Group 1 : control* 71
3.24 *Mouse 12 using DTI's* `FA` *map* 71
3.25 *Mouse 11 using DTI's* `FA` *map* 71
3.26 *Group 2 : 6 week of cuprizone* 71
3.27 *Volume 197 (mouse 5 Time* $T = 1$*)* 72
3.28 *Volume 282 (mouse 5 Time* $T = 1$*)* 72
3.29 *Artifacts on mouse 5* 72
3.30 *Volume 188 (mouse 11 Time* $T = 1$*)* 72
3.31 *Volume 278 (mouse 11 Time* $T = 1$*)* 72
3.32 *Artifacts on mouse 11* 72
3.33 *DTI's FA map for T=1* 73
3.34 *DTI's FA map for T=2* 73
3.35 *DTI's FA map for T=3* 73
3.36 *Mean of anisotropy for all mice based on DTI's FA map* 73
3.37 *Mean of axial diffusivity for selected mice based on DTI's AD map* 75
3.38 *Mean of radial diffusivity for selected mice based on DTI's RD map* 76
3.39 77
3.40 77
3.41 77
3.42 77
3.43 *Mean of anisotropy for selected mice based on DTI's FA map* 77
3.44 78

3.45 78
3.46 78
3.47 *Error of DTI's FA map for selected mice* 78
3.48 79
3.49 79
3.50 79
3.51 79
3.52 *Mean of intra-cellular fraction for selected mice based on NODDI's* `F_intra` *map* 79
3.53 80
3.54 80
3.55 80
3.56 *Error of NODDI's* `F_intra` *map* 80
3.57 81
3.58 81
3.59 81
3.60 81
3.61 *Mean of extra-cellular fraction for selected mice based on NODDI's* `F_extra` *map* 81
3.62 *Mean of isotropic fraction for selected mice based on NODDI's Fiso map* . 82
3.63 *Mean of intra-cellular volume fraction for selected mice based on NODDI's* `icvf` *map* 83
3.64 *Mean of Cerebrospinal fluid fraction for selected mice based on MF's* `frac_csf` *map* 84
3.65 85
3.66 85
3.67 85
3.68 85
3.69 *Mean of pop 0 fraction for selected mice based on MF's* `frac_f0` *map* . . . 85
3.70 85
3.71 85
3.72 85
3.73 *Error of MF's* `frac_f0` *map* 85
3.74 86
3.75 86
3.76 86
3.77 86
3.78 *Mean of population fraction for selected mice based on MF's* `fvf_tot` *map* 86
3.79 87
3.80 87
3.81 87
3.82 *Error of MF's* `fvf_tot` *map* 87
3.83 *DTI's* `FA` *map* 87

3.84 *NODDI's* `F_intra` *map* . . . 87
3.85 *MF's* `fvf_tot` *map* . . . 87
3.86 *comparison into histology and MRI for group 3* . . . 87

A.1 *Opening* . . . 101
A.2 *Closing* . . . 101

D.1 *RGB analysis on group 1 mice with cingulum* . . . 131
D.2 *RGB analysis on group 1 mice without cingulum* . . . 131
D.3 *RGB analysis on group 2 mice with cingulum* . . . 132
D.4 *RGB analysis on group 2 mice without cingulum* . . . 132
D.5 *RGB analysis on group 3 mice with cingulum* . . . 132
D.6 *RGB analysis on group 3 mice without cingulum* . . . 132
D.7 *RGB analysis on group 4 mice with cingulum* . . . 132
D.8 *RGB analysis on group 4 mice without cingulum* . . . 132
D.9 *RGB intensity difference between group 1 and group 2 with cingulum* . . . 133
D.10 *RGB intensity difference between group 1 and group 2 without cingulum* . . . 133
D.11 *RGB intensity difference between group 1 and group 3 with cingulum* . . . 133
D.12 *RGB intensity difference between group 1 and group 3 without cingulum* . . . 133
D.13 *RGB intensity difference between group 1 and group 4 with cingulum* . . . 133
D.14 *RGB intensity difference between group 1 and group 4 without cingulum* . . . 133
D.15 *RGB intensity difference between group 2 and group 3 with cingulum* . . . 134
D.16 *RGB intensity difference between group 2 and group 3 without cingulum* . . . 134
D.17 *RGB intensity difference between group 2 and group 4 with cingulum* . . . 134
D.18 *RGB intensity difference between group 2 and group 4 without cingulum* . . . 134
D.19 *RGB intensity difference between group 4 and group 3 with cingulum* . . . 134
D.20 *RGB intensity difference between group 4 and group 3 without cingulum* . . . 134
D.21 *Mean histology data for each group with empiric mean in yellow and Legendre polynomial of degree 50 in gray.* . . . 135
D.22 *empiric averaging of the signal* . . . 136
D.23 *Difference in myelin levels between group 4 and groups 2 and 3 as a function of CC section* . . . 137
D.24 *Difference in myelin levels between group 2 and group 3 as a function of CC section* . . . 138

Acronyms

AD Axial Diffusivity. 17, 74–76

ADC Apparent diffusion coefficient. 13, 15

BIDS Brain Imaging Data Structure. 23, 24

bval b value. 13, 38–40, 46

bvec b vector. 38, 39

CC Corpus callosum. ii, vi, vii, ix, 1, 3, 25, 26, 30, 34, 35, 54–61, 64–70, 76, 81, 83, 84, 86, 87, 136–138

CSF Cerebrospinal fluid. v, viii, 14, 15, 17–21, 75, 78, 81–84

DICOM Digital Imaging and Communications in Medicine. i, 2, 23, 38–40, 89

DNN Deep neural networks. 21

DTI Diffusion tensor imaging. iii, 12, 16–18, 43, 68, 74

DW-MRI Diffusion-weighted magnetic resonance imaging. vii, 12, 14, 16, 20, 21, 24, 64, 65, 68, 74

FA Fractional anisotropy. 17, 69, 70, 74–78, 91

JSON JavaScript Object Notation. 25

LFB Luxol Fast Blue. 28, 29, 57, 62

MD Mean Diffusivity. 76

MPPCA Marchenko-Pastur Principal Component Analysis. 43, 45

MRI Magnetic Resonance Imaging. i–iii, vi, 1–4, 10, 13, 16, 25, 27, 38–40, 42, 43, 52, 54, 57, 68, 89, 91

MS Multiple sclerosis. 3, 25–27, 30, 37

MSME Multi-Slice-Multi-Echo. 40–42

NifTi Neuroimaging Informatics Technology Initiative. i, 2, 25, 39, 40, 43, 49, 71

OPC Oligodendrocyte progenitor cells. 26, 27, 67

PCA Principal component analysis. 23, 43–45

PGSE Pulse gradient echo spin. 13, 14

RD Radial Diffusivity. 17, 74–76

RF-pulse Radio Frequency pulse. v, 5–8, 10, 13

ROI Region Of Interest. vi, 30, 50, 54

SVZ Subventricular zone. 1

TE Echo Time. v, 7, 9–12

TR Repetition/Relaxation Time. v, 9–12

Acknowledgements

For starters, we owe a deep sense of gratitude to Benoit Macq who commisioned the Myemouse study and followed our work from beginning to end; overseeing developements and suggesting leads.

In this mighty task, he was supported by two of his assistants, Nicolas Delinte and Quentin Dessin whom we bothered almost daily and to whom we also owe much respect and admiration. Without them, this study would have been set back for months.

We also would like to thank Gaëtan Rensonnet who started us on this study and whose work was essential to our developments.

We owe many thanks to Nicolas J. who took the acquisitions and made himself available to answer our questions.

A special thanks as well to Eric Henaut, Kelly Kamborian, Céline Everaert, Amandine Evrard and Lorenzo Barbuscia for their help reading, explaining and correcting this thesis.

Finally we wish to thank our parents (some of which are aforementioned) and loved ones who, although did not always understand our work, pushed us to the end. Thank you all.

Introduction

Many sciences are involved in the study of the human body, which is a fascinating entity that never ceases to astound because certain aspects are still a mystery to science. Philosophers, theologians, doctors, and a slew of other thinkers have spent centuries attempting to explain the myriad of phenomena that occur in the human body and mind. It is obvious that tremendous progress has been made in our modern age; we now understand why smoking is bad for one's health and why drinking alcohol can cause brain damage. However, man's unsatisfied hunger for knowledge drives us to go even further, not only to understand the causes and consequences of certain phenomenon, but also to quantify them and even cure them or prognosticate their growth and behavior in order to prevent them from occurring. Nestled within the branches of all these various disciplines, the subject of this thesis will examine certain brain phenomena, bring them to the forefront and tie them together in the hope that numerous leaves and fruits will form, grow and develop. Future generations will be able to rise even higher, perched on the solid base of the strong branches we have nurtured. Biology, computer science, and applied mathematics, three fields that are essential in our modern world, will be used together and serve as the tools for this present study.

This study is only a small portion of a broader research project that incorporates many different departments within the university. In order to achieve the study's ultimate purpose in neuro-imaging, physicists, biologists, software developers, and other professionals have frequently been called upon to help. Our thesis aims to apply PhD G. Rensonnet's fingerprinting algorithm (Rensonnet et al., 2019) [49] to a special study involving mice fed with Cuprizone. Cuprizone is a drug that leads to demyelination of the corpus callosum (CC) and activates progenitor cells in the adjacent subventricular zone (SVZ), a stem cell niche which contributes to remyelination. The healthy SVZ contains semi-activated microglia and constitutively expresses the pro-inflammatory molecule galectin-3 (Gal-3) suggesting the niche uniquely regulates inflammation. The idea is to show that the fingerprinting algorithm allows us to see damage in axons according to theory. In other words, to show that the pipeline can accurately project the damage under initial conditions [23].

Moreover, despite increasing efficiency in computer programs, too few algorithms, applications and pipelines exist, that can process Magnetic Resonance Imaging (MRI) straight out of the machine and then apply microstructural algorithms such as Neurite Orientation Dispersion and Density Imaging (NODDI) (Zhang et al., 2012)[78] and Microstructure Fingerprinting (Rensonnet et al., 2019) [49] on the cleaned data. One of our missions was to design a specific pipeline to treat data out of the Bruker machine that UCLouvain possesses

on it's Brussel's campus. In terms of pipeline, this means a script that will run on data output by the Bruker machine and that will perform conversions from Digital Imaging and Communications in Medicine (DICOM) to Neuroimaging Informatics Technology Initiative (NifTi), denoise each acquisition, motion correct them using a co-registration tool and extract the mask in order to be able to launch microstructural algorithms on them. Therefore, we will need knowledge in 3 different disciplines in order to lead a successful study. They say an image is sometimes worth more than 1000 words. We have summarized our project within science in Figure 1.

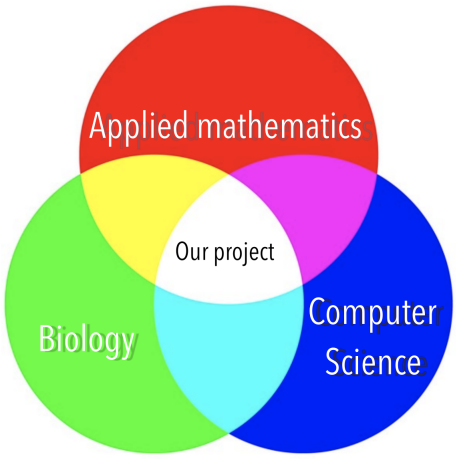

Figure 1: *Where our project lies*

While our project will unfold later on, we will need knowledge from these three major disciplines to aid us in our endeavor. It's ironic in a way; one must trade knowledge for knowledge. Nothing in our life is given away for free. As part of our project, we will investigate the anatomy of small rodents (namely mice although an easy transposition would generalise the concept to small rodents), which will lead us deep into the realm of biology. After that, with the use of mathematical tools, we will develop a computer software to better explore and analyze it based on collected biological data. This thesis and its associated research are part of a broader study that is currently being carried out at the Catholic University of Louvain-la-Neuve in collaboration with the University of Brussels (ULB), coordinated by Professor Benoit Macq and with the assistance of Anne Des Rieux and many other associates and partners.

In order to accomplish this, we will compare images of mice captured using several imaging modalities. Cuprizone was administered to these mice in order to modify the quantity of myelin present in their brains. The modalities chosen include MRI and multi-echo T2, both of which were performed in Brussels by our competent biotech team on a Bruker 11.7 Tesla machine. On the basis of this data, our task will be to transform the raw data in a file capable of being read by the fingerprinting algorithm (Rensonnet et al.,2019)[49] pipeline.

In addition, we used the histology images also provided by our biotech team as a second source of information. The end of the project will compare data from MRI images processed with the fingerprinting algorithm with the histology images from the same mice.

On a more practical level, the study of brain diseases is a crucial challenge in our day and the study of the effect of each disease on important parts of our brain may be the key to solving or preventing diseases such as Multiple sclerosis (MS), Alzheimer's or even drug abuse. Therefore, the study of the Corpus callosum (CC) becomes a vital piece of information. However one does not dissect a human brain from a cognitive human. Before any of this can be transposed to humans, tests must be run on smaller animals; namely rodents in this case. Small mammals have a similar brain structure which will allow easy transposition for later findings. Therefore artificial situations giving rise to Multiple sclerosis (MS) configurations (or other diseases for that matter) in the rodents brain must occur. Once these artificial situations are put in place, images of their brains will be taken and a study using fingerprinting and other software will be carried out in order to assess and quantify the damage. In this thesis, our task will be to connect the data output by the Bruker machine (MRI acquisition machine) with that of the fingerprinting pipeline input. Furthermore, using our histology pictures, we will co-register the fingerprinting output with the histology data to ensure that the results are accurate and consistent and allow the competent people to draw conclusions from this data

Chapter 1

Theoretical background

For a proper understanding, we will begin with some reminders. In the course of this study, we will use the term voxel to describe the volume cell of a 3D image. The word voxel derives from the terms volume and cell that have been concatenated. A voxel is to a 3D image what a pixel is to a 2D picture, and various imaging techniques use it like Magnetic Resonance Imaging (MRI), multi-echo T2, histology... that we will discuss hereafter.

1.1 Magnetic Resonance Imaging

Magnetic Resonance Imaging (Vetter and Kastler, 2018)[72] is a medical imaging technique that provides views of the interior of the body in a non-invasive manner. The idea is to determine the proton density of water in a brain voxel and as we know the density of water molecules (H_2O) in an axon or in the spinal fluid we know what the voxel contains.

We must concentrate on a single brain voxel to become familiar with the physics of the MRI. First, the proton (which is positive charged) spins and at the same time generates a magnetic moment (which can be compared to a little magnet). In general, the orientation of its magnetic fields is random, and as a result, the sum of its magnetic fields is zero ($\Sigma\mu = 0$). See left of Figure 1.1

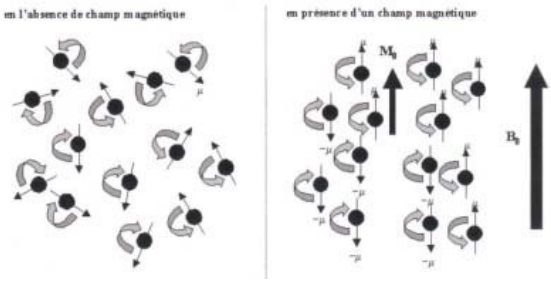

Figure 1.1: *Proton spin* [9]

1.1.1 Magnetic Resonance Imaging (MRI) metrics

In the presence of a magnetic field (B_0), protons orient themselves according to the direction of the field; some in the same direction (parallel or upward), others in the opposite direction

(anti-parallel or downward). The sum of the parallel magnetic fields minus the sum of the anti-parallel magnetic fields gives a macroscopic field ($M = \Sigma\mu^*$) see on right Figure 1.1. Indeed, a certain number of protons are in excess in parallel (by example two parts per million for a field at 0.5 Tesla).

The magnetic field M grows as a function of the proton density and the field intensity B_0. So for a magnetic field twice as high, there will be an excess of twice as many protons pointing upward. And since it is a percentage, the more protons the observed matter contains, the higher the amount of information.

Note that the protons do not align perfectly with the axis of B_0 but oscillate around it, at an angular frequency $w_0 = \gamma B_0$ called the Larmor frequency. This determines the accuracy.

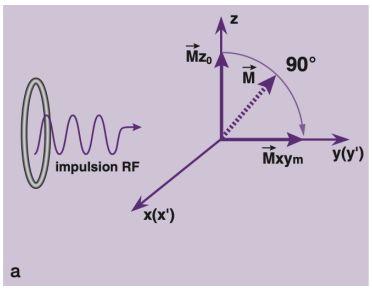

Figure 1.2: *Application of RF-pulse wave on y axis* [72]

However, as the macroscopic field M is almost aligned with the (much larger) B_0 field, it is impossible to measure the field M, as is because of the indisociablility between the two magnetic fields. Measuring M becomes possible if the M component is rotated on a perpendicular axis. To do this, we need to energise our system. We use a Radio Frequency pulse (RF-pulse) wave in the plane perpendicular to B_0 (see Figure 1.2).

By resonating with this RF-pulse wave, the field M will switch axis. Depending on the intensity or the exposure time, the field M is in the plane perpendicular to B_0 (90° rotation) or in the opposite direction (180° rotation). At the end of the excitation (RF-pulse), the vector M (while precessing around B_0) will return to a steady state quickly. This phenomenon is called relaxation and can be seen a a syringe filled with air one compresses and releases. The syringe will return to it's equilibrium after a certain time. There are two ways of measuring this relaxation time. On the one hand, the longitudinal relaxation ($T1$): gradual transition from high energy to low energy protons (anti-parallel $\mapsto$ parallel) i.e. the transition between the perpendicular position to B_0 to the parallel position (on Figure 1.2 from the y axis to the z axis) . On the other hand, the transversal relaxation ($T2$): the loss of magnetic field in perpendicular to B_0. This implies that these measure, being similar, are not computed at the same time. The $T1$ measure is computed as the field M returns towards it's equilibrium after the Radio Frequency pulse (the B_0 axis) and the $T2$ measure is computed while applying the RF-pulse (meaning while M is shifted toward the y axis).

As the magnetic moments return to the direction of the static field B_0, the oscillating signal they emit decreases until it disappears when all the magnetic moments are longitudinally aligned again. The time it takes for the nuclear magnetic moments to regain their longitudinal alignment is called the longitudinal relaxation time and is noted T1 (see Figure 1.3). The evolution of the longitudinal magnetisation "regrowth" can be given after applying

the RF-pulse excitation that caused all the magnetic moments to flip at time $t = 0$:

$$M(t) = M(\infty) \times (1 - e^{\frac{-t}{T1}}) \tag{1.1}$$

This relaxation phenomenon (i.e. return to equilibrium) follows an exponential dynamic, it would take an infinite time for all the spins to be aligned, which is why the time T1 is defined as the time taken to recover 63% of the longitudinal magnetisation to equilibrium (Kastler, 2018)[72].

This T1 relaxation time depends on the molecular agitation in the tissue being observed. If the molecular agitation is very low, the hydrogen atoms will take time to return to equilibrium. If the agitation of the water molecules is very high, as is the case in liquids such as cerebrospinal fluid, regrowth is also slow. On the other hand, if the agitation is moderate (i.e. with a time constant around the Larmor frequency) as in fat or white matter, then the T1 time is relatively short. These different T1s are around 1 second for a B_0 field of 3 Tesla. A second phenomenon is influenced by molecular agitation: whereas in theory, the magnetic moments should all rotate coherently around the axis of B_0, i.e. with a constant phase difference, molecular agitation means that the atoms will not be in the same physico-chemical environment at all times, and therefore their Larmor frequency will not be perfectly equal to the theoretical Larmor frequency either. As a result, the various magnetic moments will likely to be out of phase with one another. In turn, this results in a gradual decrease in the signal associated with their synchronous rotation over time, which is referred to as the transverse relaxation time (T2).

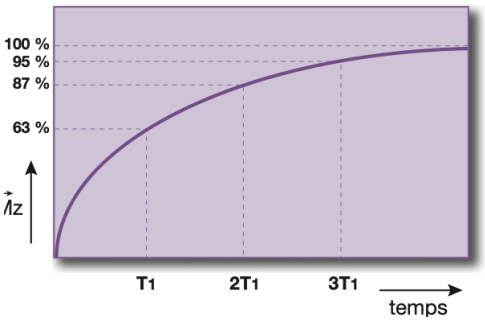

Figure 1.3: *Percentage of proton equilibrium recovery; T1 relaxation* [72]

This T2 time measures the disappearance of the transverse magnetisation, i.e. the magnetisation resulting from the fact that the magnetic moments are synchronous in their rotation in the transverse plane, perpendicular to B_0, where they were brought by the RF-pulse oscillating excitation wave. Again, this is a phenomenon that follows an exponential law (this time decreasing see Figure (see Figure 1.4)):

$$M(t) = M(0) \times e^{\frac{-t}{T2}} \tag{1.2}$$

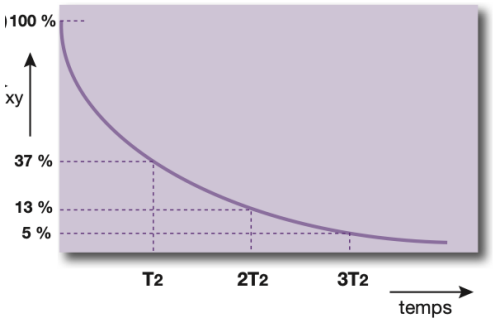

Figure 1.4: *Percentage of protons aligned with B_0; T2 relaxation* [72]

1.1.2 Multi-echo T2

The disparities present within the spins even after the application of the B_0 field, causes phase shifts following the 90° RF-pulse. However, it is possible to avoid this phase shift by applying an RF-pulse wave with a 180° phase. If, after a time $\frac{TE}{2}$ ($\frac{TE}{2}$ = half echo time), once the 90° RF-pulse has been applied (the spins have already shifted phase), a 180° RF-pulse is applied, this will reverse the phase shifts (mirror image) without changing the direction of rotation. The faster spins will now be behind the slower ones and, as the precession speeds (and the direction of rotation) remain the same, after the same amount of time, the spins will be (almost) in phase again, generating a spin echo signal (see Figure 1.5). The time of the operation is therefore two half echo time, so one Echo Time (TE).

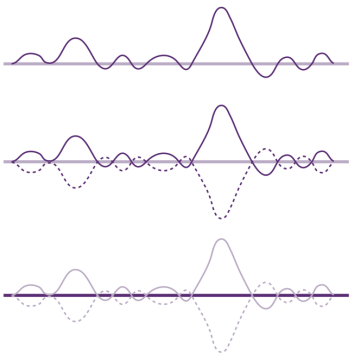

Figure 1.5: *Phase shift: line is the signal before phase shift and dot is the signal after (sum is null)* [72]

To understand this better, let's take the example of two riders. The first is much faster than the second. In the first stage of the race, the first rider will run a distance x_1 and the second a distance x_2 ($x_1 > x_2$). Then we reverse the direction of the race. After exactly the same time as the first phase, the first rider will have completed a distance $-x_1$ and the second $-x_2$. They will both be back at the starting point (in phase). The measurement is taken at all TE time steps to get the maximum signal intensity. The phase shift due to spin-spin relaxation is not corrected by the 180° RF-pulse: the vector is slightly smaller after one TE time. In order to establish the chronology of events, we will explain the sequence of operations step by step:

(a) At time t = 0, the 90° impulse is applied which tilts M in the transverse plane and the transverse magnetisation is maximal. This section of time would be the moment to compute $T2$ (Figure 1.6)

(b) The spins go out of phase quickly ($T2\times$ curve), the transverse magnetisation disappears quickly (Figure 1.7).

(c) At time t = TE/2, application of the 180° pulse, the spins rephase.(Figure 1.8).

(d) At time t =TE, the spins are rephased: the signal reappears as an echo and can be measured. (Figure 1.9).

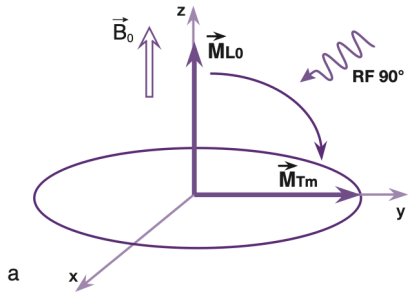

Figure 1.6: *First RF-pulse applied* [72]

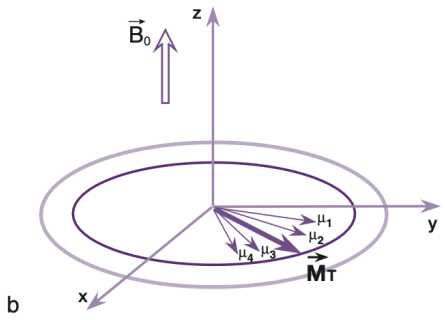

Figure 1.7: *After RF-pulse, the spins are out of phase*[72]

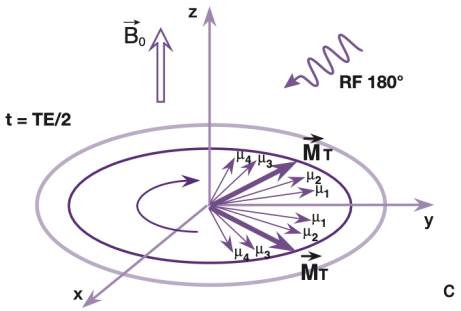

Figure 1.8: *Second RF-pulse applied in the opposite direction*

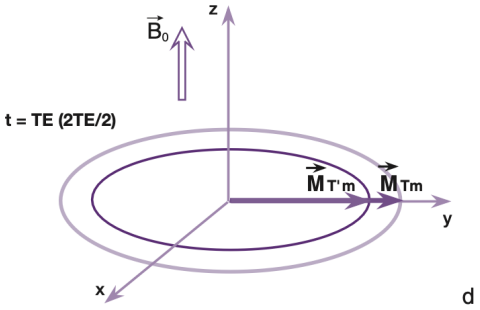

Figure 1.9: *The spins return to equilibrium position*

In order to receive a signal at the second echo, it is possible to apply a second 180° pulse, then a third 180° pulse in order to gain a signal at the third echo, and so on until the signal disappears completely at time T2.

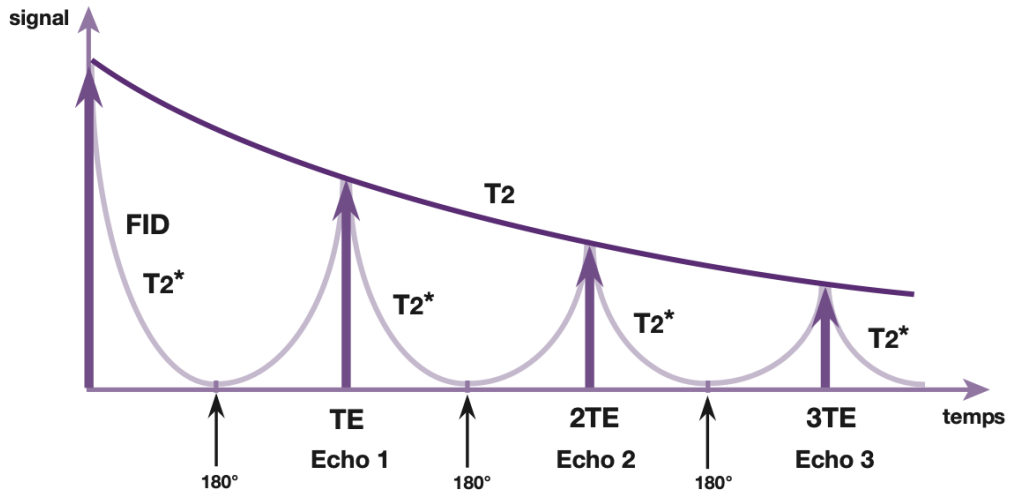

Figure 1.10: *T2 curve for 1 line* [72]

It should be noted that the cycle we just described is simply one row of the image matrix, and that it corresponds to the Fourier plane. To produce the following lines (a complete cycle corresponds to an image with 128 or 256 lines), it will be necessary to repeat the cycle of 90° and 180° pulses for each line. The Echo Time (TE) corresponds to the measurement time, and the Repetition/Relaxation Time (TR) relates to the interval between two 90° pulses or two primary cycles in this series of events. As a result, the TR not only corresponds to the "passing time" from one line to the other, but it also corresponds to the time required for the longitudinal magnetisation to be repelled.

As a result, there are numerous TE during a TR session (when compared to TR, TE duration is often insignificant; TE equals approximately 1/20th of TR). It is the Fourier plane that will later be used to gain access to the image in the future.

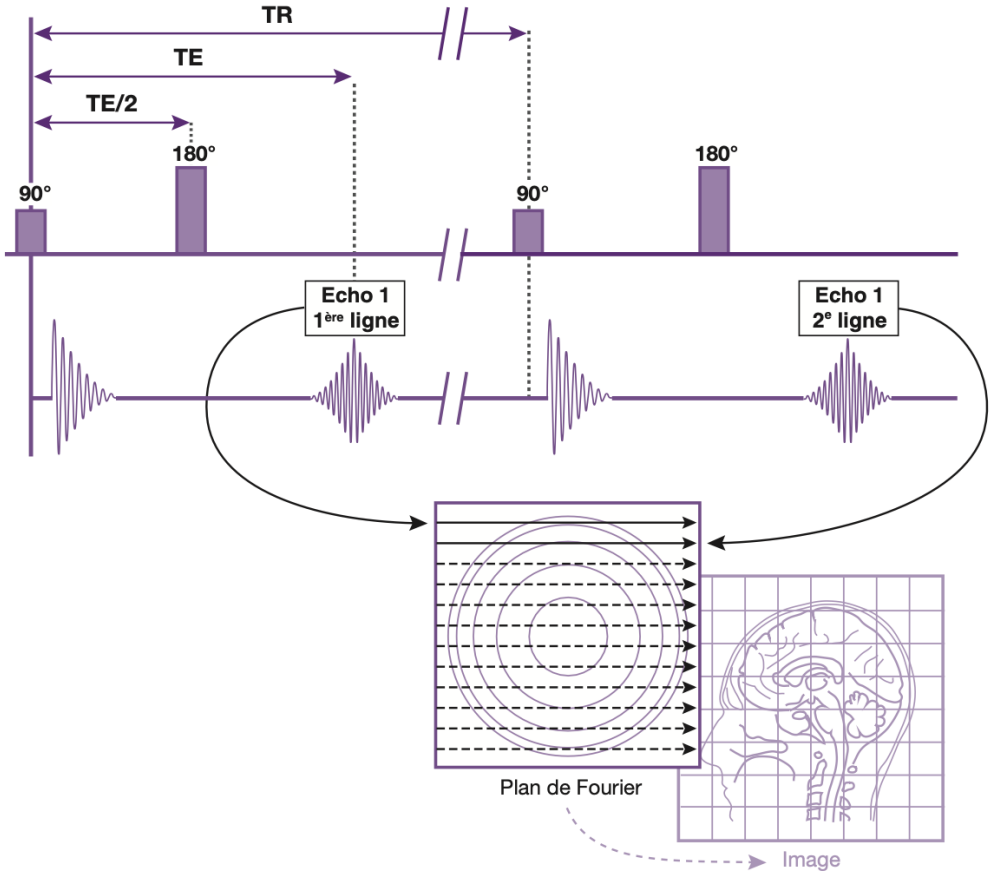

Figure 1.11: *echo T2 multi-line* [72]

Spin echo is the most often utilized imaging procedure in the world. It produces images of exceptional quality, whose T1 and T2 weighting can be determined by making an informed decision between the TR and TE parameters. Although this sequence in it self is quite short, the full process does have certain drawbacks, one of which being its length (requiring at least 128 or 256 TR lines). The full process will require 128 or 256 short sequences as each sequecne represnts an image row (see Figure 1.11).

1.1.3 Contrast

In an MRI sequence, we know that the 90° and 180° RF-pulse elemental cycle must be repeated to create a signal in the transverse plane and measure it. The Repetition/Relaxation Time (TR) is the "passing time" from one line to the other. During each TR interval, the longitudinal magnetisation M_L of each of the tissues grows back according to their respective T1. The Repetition/Relaxation Time therefore also corresponds to the "regrowth time" or recovery time of the longitudinal magnetisation.

If the TR is long (compared to the T1 of the tissues concerned: 2 s), the longitudinal magnetisation grows back to its equilibrium level at the end of each cycle (98% growth if $TR = 4 \times T1$). But the tissues have "almost" completely regained their equilibrium longitudinal magnetization. Although they have different T1 regrowth rates, they can no longer be distinguished by their T1.

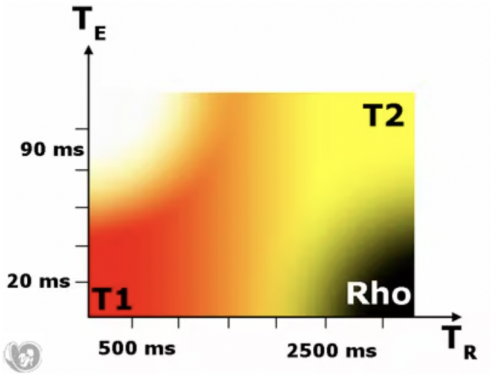

Figure 1.12: *heatMap of TR/ TE from* [26]

If the TR is short (less than or close to the T1 of the tissues concerned: 0.5 s), the longitudinal magnetisation regrowth curve is interrupted and the longitudinal magnetisation does not recover its initial level at the end of each cycle (63% regrowth if $TR < T1$). Tissue A at shorter T1 grows back faster than tissue B at longer T1: the signal of tissue A will be higher (whiter) than that of B (darker). The white/black difference will appear as contrast on the image: the tissues are distinguished by their T1.

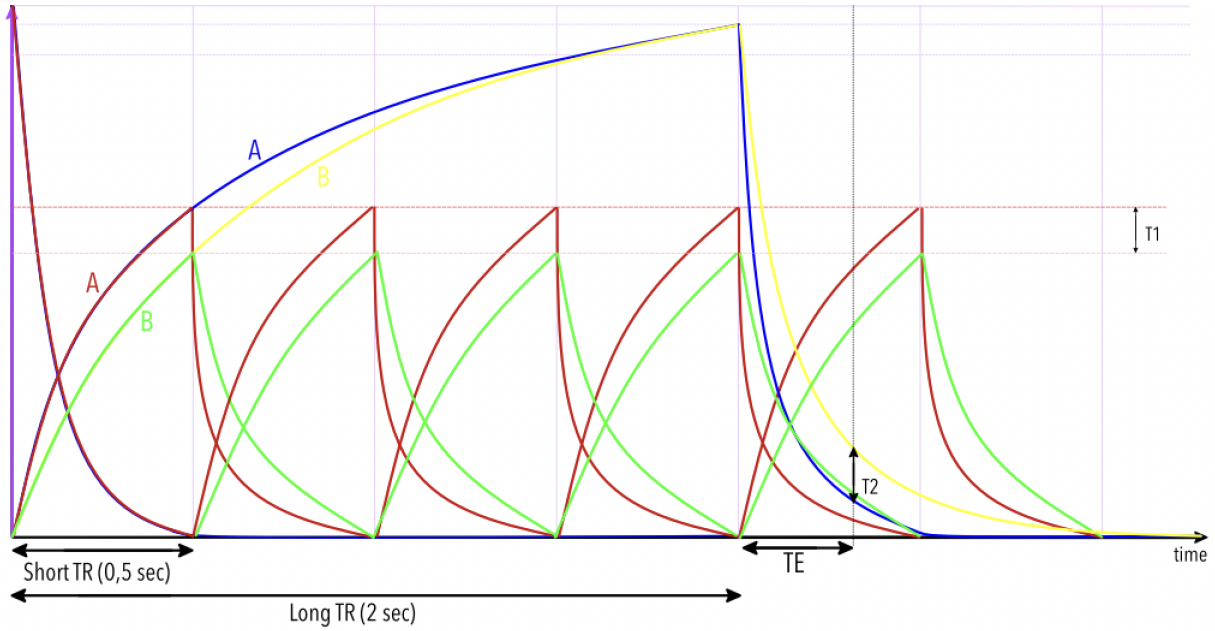

Figure 1.13: *signal influence by TR and TE*

In the spin echo sequence, the signal decays rapidly in T2* and the 180° pulse allows decay in true T2; then the signal is collected in the TE time echo.

If the TE is short ($< 20 - 30$ ms), the differences in decay rate do not have time to be expressed. The two tissues, although having different decay rates, are not well separated: they cannot be distinguished by their T2.

If the TE is longer ($> 80 - 100$ ms) (i.e. "adapted" to the decay rates of the tissues), tissue A with longer T2 decays more slowly than tissue B with shorter T2: the signal of

tissue A (measured during the echo) will be higher (whiter) than that of B (darker). The white/black difference will appear as contrast on the image: the tissues are distinguished by their T2.

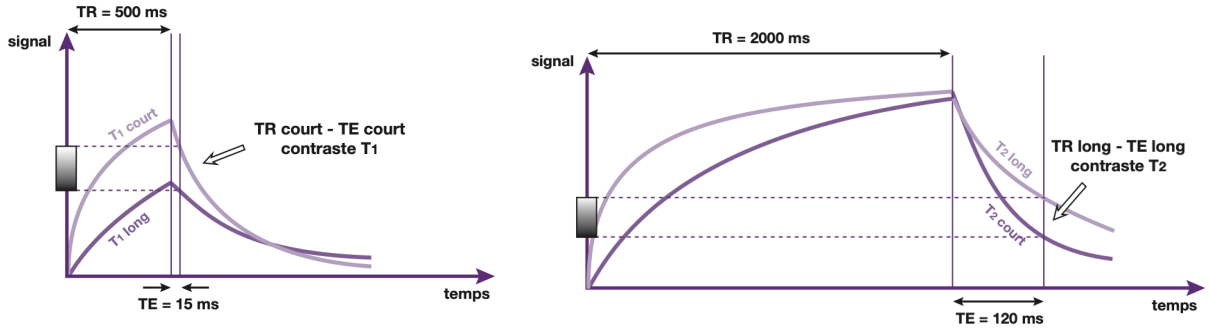

Figure 1.14: *Contrast following TR and TE: TR and TE short lead to T1 contrast; TR and TE long lead to T2 contast.*[72]

1.2 Diffusion Weighted Magnetic Resonance Imaging

Diffusion-weighted magnetic resonance imaging also known as DW-MRI, is a technique used in MRI that does not require the patient to undergo any sort of invasive procedure in order to generate contrast. This technique makes use of the natural process of diffusion that molecules go through, most notably water. Brownian motion is a type of random thermal movement that occurs in water molecules. This movement is not free but is constrained by the environment, which can include macromolecules, fibers, and membranes. Because of this, water molecule diffusion is a valuable tool for early detection of diseased tissues, with a greater specificity than typical MRI sequences because it allows investigation into the effect of brain connections. Diffusion tensor imaging (DTI), a subtype of DW-MRI, has seen widespread application in recent years for the purpose of mapping white matter tractography in the brain.

1.2.1 Diffusion Imaging Generalities

In order to highlight the microscopic motions of water in tissues, diffusion imaging is used. Water molecules do not remain motionless in a biological medium; rather, they are constantly agitated by a process known as "Brownian motion". These random molecule movements, which can be more or less intense depending on the environement, are what distinguish molecular diffusion from other types of diffusion. As a result, the freer the water is in a given region, the easier it is for molecules to move around and the larger the amount of molecular agitation (high diffusion). In a functioning brain, the type of diffusion refers to the diffusion of water with a Gaussian displacement pattern.

It characterizes the water displacement in the extra-cellular space defined by cellular membranes of soma, glial cells and other bodies; it is often referred to as "hindered diffusion"[15]. On the contrary, the molecular agitation is diminished in specific sections of the tissues as a result of the obstructions that prevent these movements from occurring (reduced diffusion). Water diffusion in restricted geometries is often referred to as "restricted diffusion".

Restricted diffusion describes the water in the intracellular space, which is bounded by axonal or dendritic membranes, and is characterized by a non-Gaussian pattern of displacement. Diffusion MRI is often used to measure neurite morphology by separating intracellular and extracellular water.

If there is a gradient in the magnetic field, the movements of hydrogen protons induce phase shifts, which diminish the signal in MRI. These phase shifts become even more significant as the speed of the protons increases. As a result, the agitation of water molecules will have that very same effect on the signal i.e. protons in water moclecules wil induce phase shifts. Additional gradients are introduced in a series in order to draw attention to these minute molecular movements and, as a result, to obtain "diffusion-weighted" images, which are then analyzed. "Diffusion gradients" are applied on either side of the 180° RF-pulse pulse to get the desired effect.

1.2.2 Pulse Gradient Spin Echo

Pulse gradient echo spin (PGSE) is the most common sequence used to measure how water molecules move through the images. This changed spin echo sequence is made up of two additional diffusion gradients (see Fig 1.15). The first gradient is put on after the 90° pulse and is used to get the magnetization out of phase. The second gradient is put on after the 180° pulse and is used to get the magnetization back into phase. The PGSE sequence has several parameters :

- Δ :time between the two diffusion gradients.
- δ duration of the diffusion gradients.
- g magnitude of the diffusion gradients.

These parameters are physically represented in Figure 1.16 (and with other variables Figure 1.15) are summarized under a single scalar that characterizes the Pulse gradient echo spin (PGSE) sequence, the bval (s/mm^2) which is defined by the Stejskal-Tanner[1] equation: (Huisman, 2010) [25]:

$$b = (\gamma \times g \times \delta)^2(\Delta - \delta/3) \tag{1.3}$$

[1]The Stejskal-Tanner equation as defined by (Skejtal and Tanner, 1965)[61] is often written to be $\ln(\frac{S(2\tau)}{S(0)}) = -\gamma^2 D\delta^2(\Delta - \frac{1}{3}\delta)g^2$ However if we define b as being $b = -\frac{(\ln(S(2\tau)) - \ln(S(0)))}{D}$ then we find the above equation derived from Skejtal and Tanner's original form. This last equation will be used when trying to calculate the Apparent diffusion coefficient (ADC).

Where γ = gyromagnetic ratio, G = amplitude of the gradient, τ = time of application of the gradient, and T = time between the application of the two diffusion gradients. b is expressed in s/mm^2 and will vary from 0 to about $2,500 s/mm^2$ in our study (although throughout the medical field, it is not uncommon to find much higher values). Increasing the value of b increases the sensitivity of the sequence to molecular diffusion. This b value will return in the next section while discussing the PGSE; we will refer to it as b value.

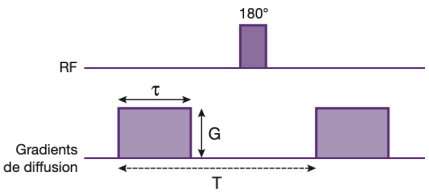

Figure 1.15: *Factor of b*

Most frequently, images are acquired with a b value of 0 and 1000 $[s/mm^2]$. The Diffusion-weighted magnetic resonance imaging are weighted by the way water molecules move along the direction of the diffusion gradients. To deal with anisotropic diffusion, the imaging process is usually done more than once in different directions. In cerebrospinal fluid (CSF), diffusion is globally isotropic, which means that the signal is the same no matter how the diffusion gradients are oriented. However, in axons, diffusion is very anisotropic. A water molecule in an axon is more likely to move along the direction of the axon than in a direction that is perpendicular to it.

In practice, a diffusion sequence is comprised of the sequential application of three sequences with diffusion gradients in the axes of slice selection, phase encoding, and frequency encoding, respectively: three images are generated per slice, with diffusion weighting in each corresponding axis. In theory, a decrease in diffusion in the direction of the diffusion gradient will result in a hypersignal in the picture produced from the diffusion axis that is decreasing in diffusion. One can reconstruct a fourth image from the combination of the three preceding images: this processing involves taking an average of each pixel from the three diffusion images and maintaining the hypersignal only if it is present in all three axes of the image.

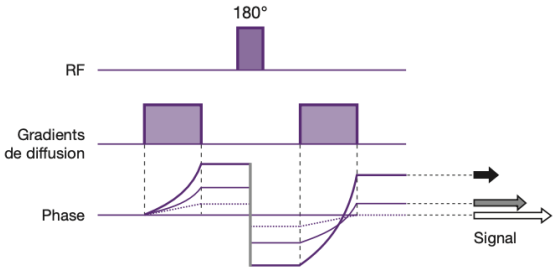

Figure 1.16: *Diffusion's signal*

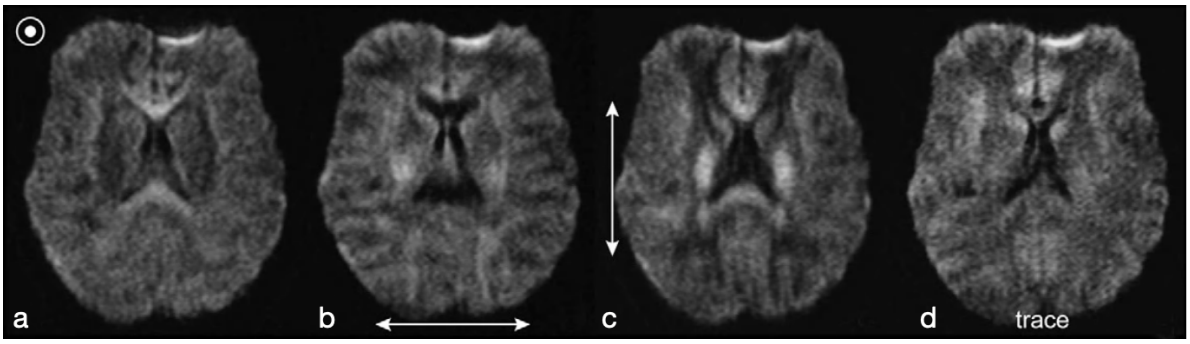

Figure 1.17: *Example of Diffusion-weighted EPI brain images ($b = 1000$). Diffusion gradients were applied in the three axes: slice selection (a), frequency coding(b) and phase coding(c). A fourth image (sometimes called trace image) is reconstructed from the combination of the three previous images (d).*

The phenomenon of molecular diffusion is comparable in all directions of space for the grey matter or cerebrospinal fluid (CSF) (isotropic diffusion), but is particular for the white matter. The white matter is characterised by a fibre arrangement: the diffusion of water molecules is facilitated along the axonal fibres but reduced perpendicular to the fibres (anisotropic diffusion). Thus, a hypersignal may indicate a perpendicular arrangement of the white matter fibres with respect to the diffusion gradient, hence the importance of applying these gradients in the three planes of space.(Le Bihan and Warach, 1995) [35]

Another parameter that can be measured in diffusion imaging is the Apparent diffusion coefficient (ADC) (which note by variable D): it allows a more accurate assessment of the anomalies of diffusion. The attenuation Att of the signal due to the diffusion of water molecules in biological tissues is, in fact, characterised by the following relationship:

$$Att = e^{-b \times D}$$

Where b is the gradient factor seen previously and D is the Apparent diffusion coefficient. D is expressed in mm^2/s (the opposite unit to b). This value is lower than that of pure water because of the obstacles encountered by water molecules in tissues (cell membranes, molecular barriers, etc.) which slow down diffusion. To calculate D, at least two diffusion imaging acquisitions are required: an acquisition with no diffusion gradient ($b = 0$), giving a signal S_0, and an acquisition with diffusion gradients of a given value b producing a signal S (knowing, as we have seen previously, that a high value of b allows the differences in diffusion speed to be better highlighted). The value of D is then given by the following relation also called the Stejskal-Tanner equation (Stejskal and Tanner, 1965)[61]:

$$log(\frac{S}{S_0}) = -b \times D \tag{1.4}$$

The ADC of different biological tissues can thus be calculated. It is actually derived from equations 1.3 as previously stated in the footnote of equation 1.3.

1.2.3 Diffusion tensor imaging (DTI)

After the DW-MRI data have been recorded, the information about tissue microstructure that is encoded in the observed diffusion signal must be retrieved using models. DTI is the model that is used the majority of the time. Although diffusion is tensorial, the goal in many circumstances is to use diffusion anisotropy in white matter to determine axon direction and magnitude or degree of anisotropy. Tensors reside in a material or tissue and do not move when the coordinate system that describes them is rotated. The ellipsoid is a physical representation of a tensor (of rank 2) that has historical significance in the development of diffusion anisotropy imaging in MRI. DTI is based on the concept of modeling the diffusion of water molecules in each voxel using a symmetric positive semi-definite three-by-three diffusion tensor called D. This allows for an analysis of the diffusion of water molecules in three dimensions. Diffusion MRI is based on tensors, which are geometric quantities with mathematical and scientific implications.

$$\begin{bmatrix} D_{xx} & D_{xy} & D_{xz} \\ D_{yx} & D_{yy} & D_{yz} \\ D_{zx} & D_{zy} & D_{zz} \end{bmatrix}$$

The components of this matrix that are diagonal correspond to diffusivities along the three orthogonal axes of the scanner, but the ones that are off-diagonal relate to the correlation between displacements along those orthogonal axes (Johansen-Berg and Behrens, 2013)[32]. The following diagonalization with eigenvalues are possible like in this matrix:

$$D = Q\Lambda Q^{-1} \text{ with } \Lambda = \begin{bmatrix} \lambda_1 & 0 & 0 \\ 0 & \lambda_2 & 0 \\ 0 & 0 & \lambda_3 \end{bmatrix} \tag{1.5}$$

As previously stated, it is common practice to think of the diffusion tensor in terms of an ellipsoid, which is a surface that represents the distance from the origin that a molecule would diffuse to with an equal probability. An "internal reference frame," also known as the eigensystem, can be obtained by the use of the diffusion tensor formalism. The eigenvectors are responsible for determining the primary axes of the ellipsoid, and the diffusion distance in a given amount of time, t, (which is proportional to the square root of the diffusivity), determines the lengths of the principal axes (Johansen-Berg and Behrens, 2013)[32].

In order to estimate the diffusion tensor, which is symmetric, it is necessary to have a minimum of six gradient directions, in addition to the base signal (that is, without diffusion). This base signal is referred to as the b0 volume since its b-value is equal to zero [s/mm2]. In practice, more than six gradients and one b0 are gathered since having more information allows for better correction of the huge number of artifacts and noise impacting diffusion datasets. In addition, having more information allows for more accurate reconstruction of the original data. (Alexander et al. 2007)[1]

A number of metrics that may be used to reflect the current condition of the brain's microstructure can be derived from the diffusion tensor. The mean diffusivity (MD) is

calculated by taking the average of the eigenvalues of the diffusion tensor.

$$MD = \frac{\lambda_1 + \lambda_2 + \lambda_3}{3} \tag{1.6}$$

This number indicates the degree to which the movement of water molecules inside a particular voxel is inhibited. It is possible to get anisotropy indices by computing the Axial Diffusivity (AD)

$$AD = \lambda_1 \tag{1.7}$$

and the Radial Diffusivity (RD)

$$RD = \frac{\lambda_2 + \lambda_3}{2} \tag{1.8}$$

and comparing the results of these computations. They both represent the mean diffusivity in their respective directions, which are axial and radial. However, the Fractional anisotropy (FA) meter is by far the most often used DTI metric. The FA values range from 0 to 1, with 0 indicating that all of the eigenvalues are equal $\lambda_1 = \lambda_2 = \lambda_3$ and that the diffusion is isotropic (for example, in the Cerebrospinal fluid (CSF)), and 1 indicating that one direction λ_1 is largely dominant for the diffusivity and that the diffusion is strongly anisotropic.

$$\text{FA} = \sqrt{\frac{3 * [(\lambda_1 - MD)^2 + (\lambda_2 - MD)^2 + (\lambda_3 - MD)^2]}{2 * (\lambda_1^2 + \lambda_2^2 + \lambda_3^2)}} \tag{1.9}$$

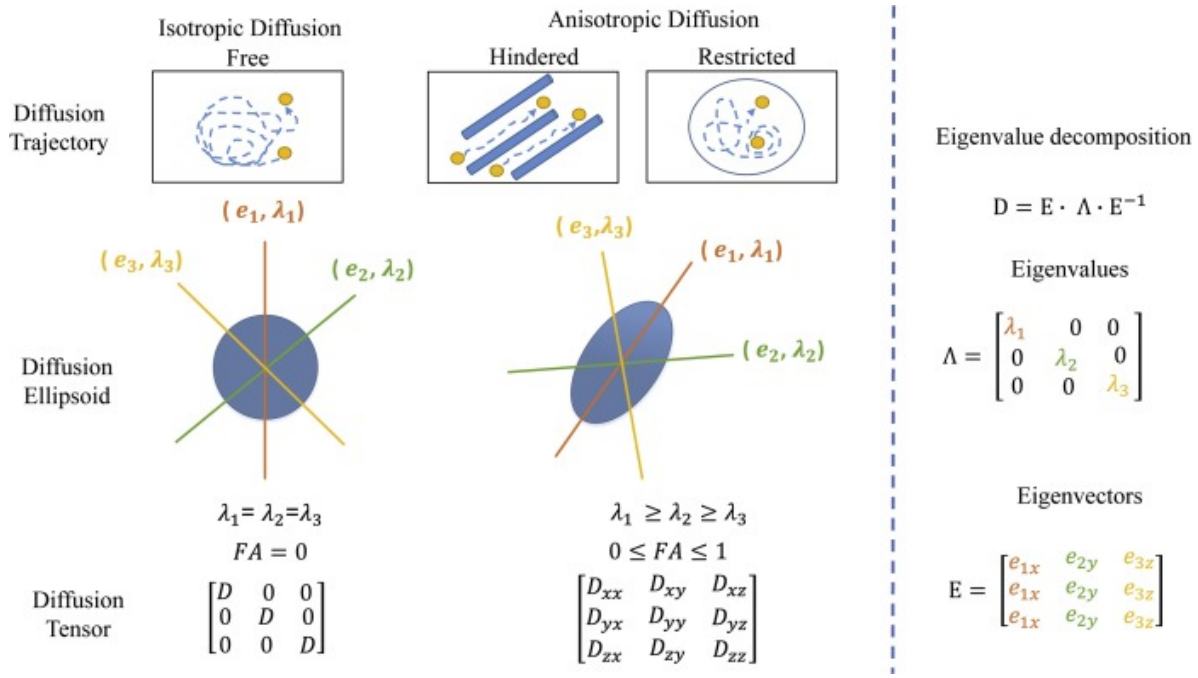

Figure 1.18: *Summary of DTI parameters from (Gholizadeh et al., 2019) [22]*

The DTI has several benefits; it is an easy-to-understand model that can be modified in a short amount of time. It also gives helpful clinical metrics that are related to biological characteristics, such as myelination or tissue organization. Having said that, the model does have some drawbacks. It is challenging to interpret, as a shift in a DTI statistic cannot be traced back to a particular shift in the microstructure. The metrics can only provide indirect measurements of the brain's microstructure, because the same DTI qualities could be exhibited by many structures that have significantly different properties. In addition to this, it does not take into consideration fascicle crossing, which happens anywhere from 60 to 90 percent of the time in voxels. The model cannot capture intricate fascicle patterns.

1.3 Microstructural multi-compartment models

1.3.1 NODDI

Neurite Orientation Dispersion and Density Imaging (NODDI) (Zhang et al., 2012)[78] is a multi-compartment microstructural model that differentiates three types of brain tissue environments: intra-cellular, extra-cellular, and CSF compartments.

- **CSF compartement**: space occupied by fluid that flows in and around the hollow spaces of the brain and spinal cord, and between two of the meninges (see cerebrospinal fluid).
- **Intra-cellular compartement**: The intracellular compartment is the region enclosed by the membrane of neurites.
- **Extra-cellular compartement**: The extra-cellular compartment is the space around neurites that is populated by several types of glial cells as well as cell bodies in gray matter (soma).

Each of these compartments is modeled separately and has an effect on how water moves through the system (Le Bihan, 1995)[35]. They each make a normalized MR signal on its own, and the superposition principle is used to add up all of the signals. This means that the total normalized signal A can be written as

$$A = (1 - \nu_{iso})(\nu_{ic}A_{ic} + (1 - \nu_{ic})A_{ec}) + \nu_{iso}A_{iso} \tag{1.10}$$

where A_{ic} and ν_{ic} are the intracellular compartment's normalized signal and volume fraction; A_{ec} is the extracellular compartment's normalized signal; and A_{iso} and ν_{iso} are the CSF compartment's normalized signal and volume fraction. Each compartment's tissue and signal model is described below.

CSF compartment model: The space inhabited by cerebrospinal fluid is referred to as the CSF region. It is represented as an isotropic gaussian diffusion with d_{iso} diffusivity.

$$A_{iso} = e^{-bd_{iso}} \tag{1.11}$$

Where A_{iso} represents the normalized attenuation signal, b are the gradient direction and d_{iso} represents the isotropic diffusivity.

Intra-cellular model: In order to reflect both the highly confined character of diffusion perpendicular to neurites and the unconstrained nature of diffusion along them, we model this space as a set of sticks, i.e. cylinders of zero radius. Over all conceivable stick orientations $\mathbf{n}$, the total signal of this compartment is given by:

$$A_{ic} = \int_{\mathbb{S}^2} f(\mathbf{n}) \underbrace{e^{-bd_{||}(\mathbf{q}\cdot\mathbf{n})^2}}_{\text{Individual stick signal}} d\mathbf{n} \qquad (1.12)$$

where $\mathbf{q}$ and b are the gradient direction and b-value of diffusion-weighting, respectively; $f(\mathbf{n})d\mathbf{n}$ gives the probability of finding sticks along orientation $\mathbf{n}$; $e^{-bd_{||}(\mathbf{q}\cdot\mathbf{n})^2}$ gives the signal attenuation due to unhindered diffusion along a stick with intrinsic diffusivity $d_{||}$ and orientation $\mathbf{n}$. The Watson distribution is chosen because it is the simplest orientation distribution that can capture the dispersion in orientations (Mardia and Jupp, 1990)[38]. Thus giving us:

$$f(\mathbf{n}) = M(\frac{1}{2}, \frac{3}{2}, \kappa)^{-1} e^{\kappa(\mu,\mathbf{n})^2} \qquad (1.13)$$

where M is a confluent hypergeometric function, μ is the mean orientation, and κ is the concentration parameter that measures the extent of orientation dispersion about μ.

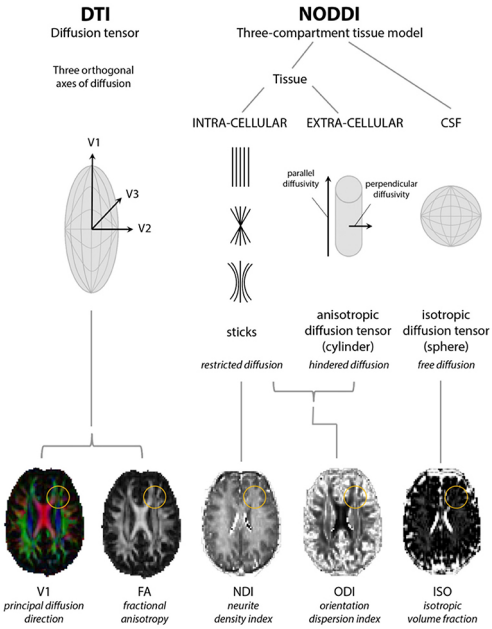

Figure 1.19: *Diffusion models for NODDI in comparison with DTI. NODDI considers constrained diffusion in intra and extra cellular compartments as well as free diffusion in cerebrospinal fluid (CSF). (Barritt et al. 2018)* [4]

Extra-cellular model: The extracellular compartment is the region around neurites that is populated by several types of glial cells as well as cell bodies in gray matter (soma). The existence of neurites slows but does not prevent water molecules from diffusing in this area, hence it is described with simple (Gaussian) anisotropic diffusion. The normalized attenuation signal is given by:

$$A_{ec} = e^{-b\mathbf{q}^T(\int_{\mathbb{S}^2} f(\mathbf{n})D(\mathbf{n})d\mathbf{n})\mathbf{q}}$$

$D(\mathbf{n})$ is a cylindrically symmetric tensor with the principal direction of diffusion $\mathbf{n}$, diffusion coefficients $d_{||}$ parallel to $\mathbf{n}$ (fixed to the same value as the intrinsic free diffusivity of the intra-cellular compartment) and $d_{\perp} = d_{||}(1 - \nu_{ic})$ perpendicular to $\mathbf{n}$. The diffusion is described by a tensor since the diffusion perpendicularly to the axon is not neglected anymore for this compartment. When setting the parameters, refer to (Zhang et al., 2012)[78] page

1003 on protocol optimization.

Advantages of NODDI :

- NODDI has the ability to capture useful clinical metrics that relate to biological features: for instance neurites densities or orientations.
- NODDI gives more insight on the image than DTI because of its fundamental model; the three compartments.

Limitations of NODDI :

- It does not account for the radial diffusivity of the axons.
- Some parameters such as $d_{||}$ and d_{iso} require a manual assigning that can lead to biased values of the estimated parameters.
- Does not account for crossing fascicles while it occurs in 60% to 90% of the voxels (Jeurissen et al., 2013)[31]. The model cannot capture complex configurations of fascicles.

1.3.2 Fingerprinting

Rensonnet G. (Rensonnet et al., 2019)[49] developed a model that uses Monte Carlo simulations and dictionary matching to determine which parameters best reflect the subsurface microstructure in each voxel. In a manner analogous to that of the DIAMOND (Scherrer et al.,2016)[55] model, each voxel is taken to be composed of a variety of structures (such as fascicles and an extra-axonal compartment) which are combined based on the superposition principle. Let a white matter voxel be composed by the independant contribution of K fascicles with principle unit direction $u_1 \ldots, u_k$ and occupying a fractionnal amount of space $\nu_1, \ldots, \nu_k$ within the physical volume of the said voxel. These fascicles also occupy a partial volume ν_{csf} of the Cerebrospinal fluid. For this given voxel, the DW-MRI signal S is given by:

$$S = M_0 \cdot \Big(\sum_{i=1}^{K} \nu_i A_{fasc}(\Omega_k, \mathbf{T}_k, \mathbf{u}_k; \mathbf{g}) + \nu_{csf} A_{csf}(D_{csf}, \mathbf{T}_{csf}; \mathbf{g}) \Big) \tag{1.14}$$

$$= \sum_{i=1}^{K} \omega_k A_k + \omega_{csf} A_{csf} \tag{1.15}$$

With M_0 taken to be the net initial transverse magnetization of the voxel detected by the scanner, $\omega_k := M_0 \nu_k$ is the Nuclear magnetic resonance apparent signal weight of the contribution of the k-th fascicle and $A_{fasc}(\Omega_k, \mathbf{T}_k, \mathbf{u}_k; \mathbf{g})$ is the normalized DW-MRI signal of

the k-th fascicle modeled by Monte Carlo simulation for an orientation $\mathbf{u}_k$, microstructural parameters Ω_k, Nuclear magnetic resonance relaxation parameters $\mathbf{T}_k$ (e.g. T1, T2) and gradient profile $\mathbf{g}$. The set $[A_{fasc}(\Omega, \mathbf{T}, \mathbf{u}; \mathbf{g}_i)]_{i=1}^{M}$ is defined by (Rensonnet et al, 2019)[49] as a fingerprint. Within the CSF compartement, water is assumed to diffuse freely with diffusivity coeffcient D_{csf}.

The algorithm starts with a precomputing step. Using criteria that are justified by tissue biology, a discrete sampling of N points in the Ω space of microstructural parameters is carried out. This model depicts the fascicles as a hexagonal packing of impermeable cylinders, each of which has a radius of r and a spacing of s.

A dictionary F^0 is then produced through the use of a large number of Monte Carlo simulations, each of which is run for a different possible combination of tissue parameters. Therefore, every column of the newly formed dictionary (shown in Figure 1.20) represents a fingerprint that is inextricably linked to the underlying microstructural structure of a voxel.

$$F^0 = [A_1^0, \ldots, A_N^0] \text{ with } A_j^0 = [A_{fasc}(\Omega_j, \mathbf{T}_k, \mathbf{u}_k; \mathbf{g}_i)]_{i=1}^{M}$$

After that, a powerful pattern matching algorithm is used to individually compare each voxel to the fingerprint (or set of fingerprints) that provides the most accurate interpretation of the signal y. (the input diffusion data of the subject, see the left side of Figure 1.20). The associated tissue parameters can then be derived from the fingerprints that have been acquired. Taking a look at the illustration in Figure 1.20, the signal y may be most accurately approximated by the fascicles a_1 and a_5, with each column representing a fraction α and β of the signal, respectively.

When there are numerous fascicles present, the microstructure fingerprinting model applies the superposition approximation to determine how Diffusion-weighted magnetic resonance imaging (DW-MRI) signals are distributed across the space. It is generally accepted that the signal that results from crossing fascicles is equivalent to the total of the signals that result from each fascicle operating independently.

Advantages of MF :

- Model with multiple compartments that takes into account several fascicles per voxel and is able to handle fascicles that cross over one another.
- Monte Carlo simulations simulations of the random walk of water molecules are known to provide near ground truth for DW-MRI signals, and experiments have shown that it exhibits results that are generally more specific and decipherable than metrics obtained with forward signal models such as NODDI or DIAMOND (Rensonnet et al., 2019)[49].
- In a wide variety of synthetic, in vivo, and ex vivo tests, it provides tissue parameters that may be relied upon and are physically decipherable.
- Increased model complexity can still be computationally solved with the help of the superposition approximation for crossing fascicles and accelerated approaches based on DNN.

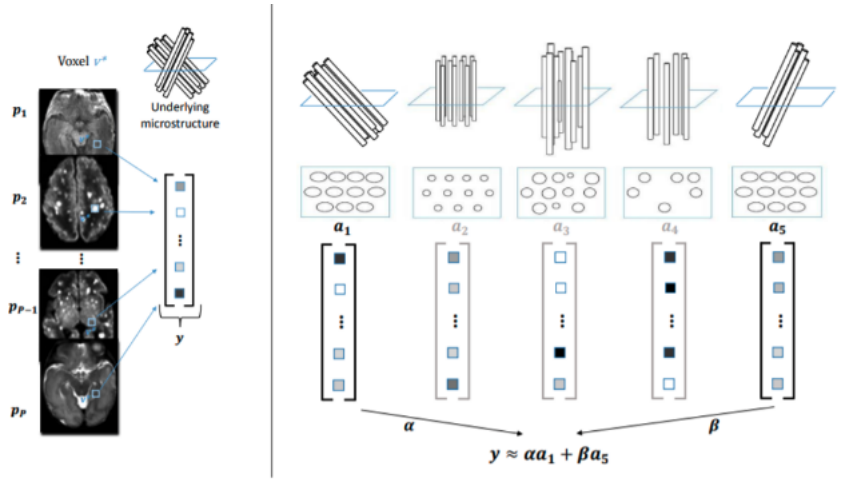

Figure 1.20: *Summary of the Microstructure Fingerprint algorithm modus operandi*[50]

Limitations of MF :

- Cost in terms of computations incurred during the production of the dictionary (i.e. precomputing steps).
- The model does not yet account for the permeability of membranes, the undulation of axons, or the presence of glial cells.
- The MF metrics are estimated voxel wise, which means that in practice there are no guarantees that the fascicles that are labeled into a particular compartment will be labeled the same way for another brain or between adjacent voxels. This is because in practice there are no guarantees that the MF metrics will be accurate.

1.4 Elikopy

ElikoPy is a novel pipeline that was developed by (Dessain and Simon,2021)[13]. It is a dedicated diffusion magnetic resonance imaging (dMRI) toolbox that was developed to correct all common known dMRI artifacts. In addition, (Dessain and Simon, 2021)[13] placed a particular emphasis on the adaptability of the pipeline to large-scale population studies. Python is used as the basis for the implementation, which relies mostly on the Diffusion Imaging in Python (DIPY) package (Garyfallidis et al., 2014)[21], as well as the Dmipy package (Fick et al., 2019)[18], and the MicrostructureFingerprinting (MF) module (Rensonnet et al., 2019)[49]. In addition to this, it makes use of the potential offered by the FSL software (Jenkinson et al., 2012)[30], Freesurfer (Fischl, 2012)[19], Advanced Normalization Tools (ANTs) (Avants et al., 2009)[3], Itktools (Yushkevich et al., 2016)[77], Mrtrix3 (Tournier et al., 2019)[69], and Distribution of 3D Anisotropic Microstructural Environments in Diffusion Compartment Imaging (DIAMOND) (Scherrer et al., 2016)[55].

ElikoPy is completely open-source and is made available to the public on Github. This pipeline supports as input the traditional Digital Imaging and Communications in Medicine (DICOM) format as well as the increasingly popular Brain Imaging Data Structure (BIDS) format (Gorgolewski et al., 2016). Additionally, this pipeline supports the Neuroimaging Informatics Technology Initiative (NIfTI) format. The high-level workflow that is supported by ElikoPy is depicted in Figure 1.21 below.

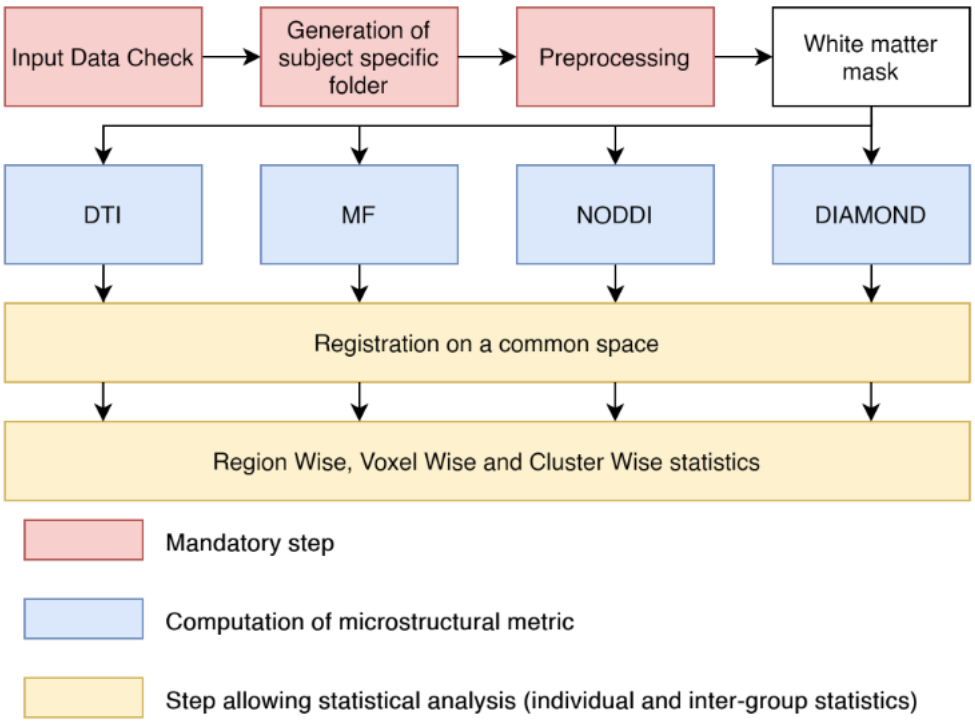

Figure 1.21: *The ElikoPy pipeline's key processing phases are shown in this diagram.* [13]

In the first step of the auditing process, the data that have been processed with ElikoPy are checked to make sure that the image dimensions match the dimensions of the b-value and b-vector files, as well as the acquisitions parameters and index files. This is done by using a diverse set of functions defined in the Elikopy API. If all goes according to plan, a separate folder for each subject's data will be created. After that, preprocessing can be utilized to make adjustments to and improvements upon the raw image. This includes the extraction and slicing of the brain, denoising based on Principal component analysis (PCA) using the Marchenko-Pastur distribution, suppression of Gibbs ringing artifacts in image space, estimation and correction of the susceptibility induced field, modeling and correction of subject movements, and bias field correction as a final step. After the preprocessing is complete, a white matter mask that is registered on the diffusion data can be obtained by using a T1 image or it can be computed directly from the diffusion data by segmenting an anisotropic power (AP) map (Dell'Acqua et al., 2014)[12]. Both of these methods are described in (Dessain and Simon, 2021)[13].

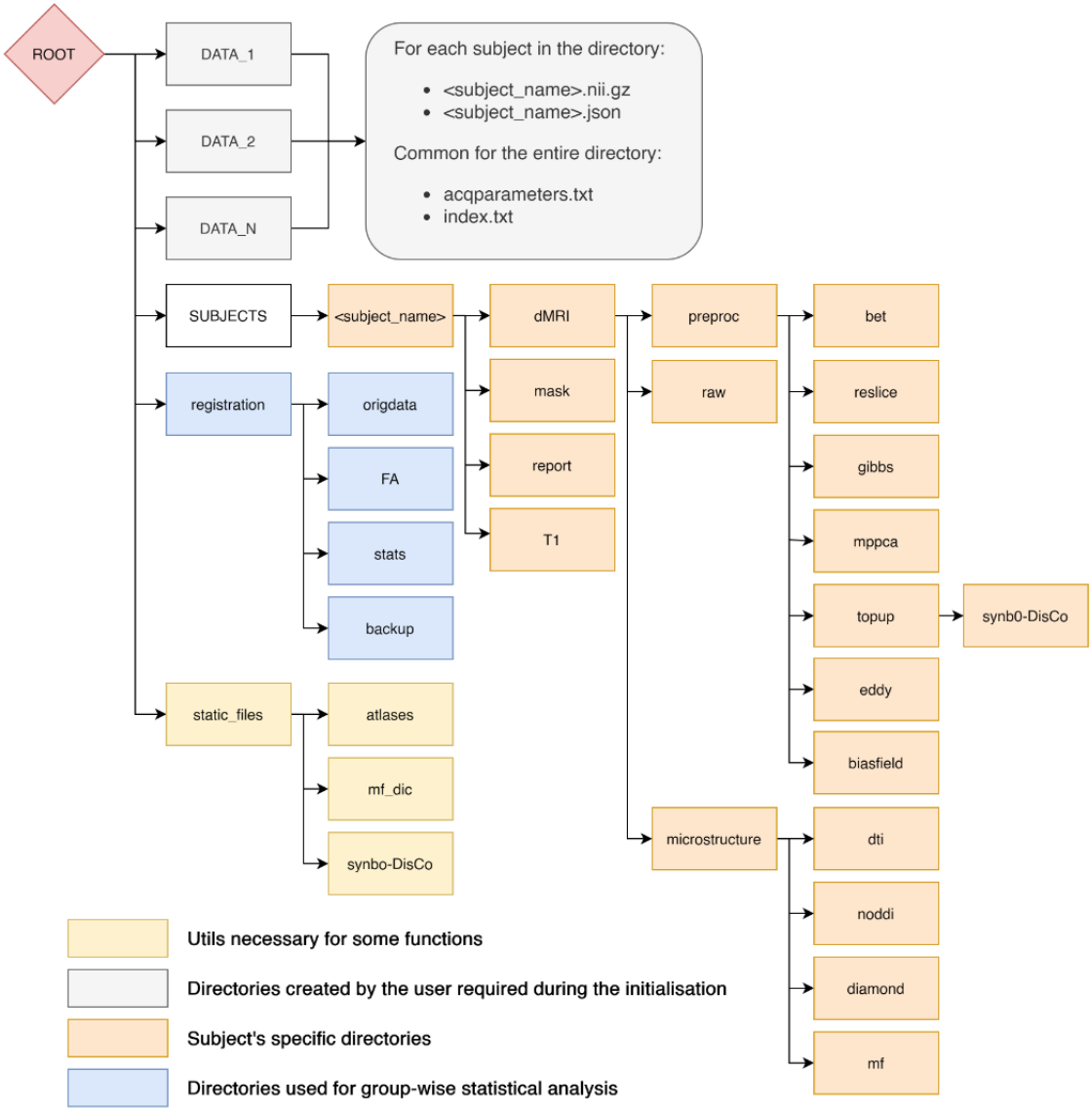

Figure 1.22: *The ElikoPy toolbox uses the following folder structure.* [13]

Alternately, rather than the collection of data folders, a path to a Brain Imaging Data Structure (BIDS) folder tree can be used to establish the library rather than the folder collection. ElikoPy will dynamically separate the subjects into different classes based on their metadata if the folder tree in question is one of the types described above (based on the acquisition parameters and the slice acquisition timing specification). Based on the BIDS naming pattern, ElikoPy will also determine which DW-MRI and structural T1 pictures should be copied into the subjects folder. Each valid subject that is represented in the data folders will have their own subfolder within the subjects folder. There are a

total of three JavaScript Object Notation (JSON) files located within these subfolders. The list of subjects who have raw data that are invalid can be found in the subj error`.json` file. The list of acceptable subjects and their corresponding subject types can be found in the subject list `.json` file. JSON can be thought of as a dictionary that assigns each topic's subfolder to the appropriate data class. The result of each preprocessing and processing function that was carried out on the patient associated with the subdirectory can be found in its own subdirectory within the subjects folder. The output includes both NifTi files and log files, in addition to a few extra files that are associated with the particular functions. The registration folder includes group-wise statistics and voxel-wise data for each registered metric. The folder also includes diffusion metrics that have been registered to a common space. Last but not least, the MF dictionary and Synb0-DisCo atlases can be found in the library's static files folder. These files are required for certain processing steps of the library. A few adjustments on the Elikopy pipeline have been made by its developers in order for us to adapt the whole pipeline to the data output by our own. This has rendered Elikopy to be a rodent friendly MRI analysis tool in studies involving mice and other small creatures.

1.5 Artifacts in Magnetic Resonance Imaging

In Magnetic Resonance Imaging (MRI), a visual artifact, also known as an anomaly seen during visual representation, is referred to as an MRI artifact. It is a feature that can be seen in an image but is not physically present in the object that is being portrayed. During an MRI, a wide variety of abnormalities may appear; some of these artifacts may compromise the diagnostic accuracy, while others may be misinterpreted with pathology. It is possible to divide artifacts into three categories: those connected to the patient, those depending on the signal processing, and those related to the hardware (machine). An extensive list of known artifact have been reported on `Wikipedia`.

1.6 Miniature mouse model

Pre-clinical trials are often carried out on non human subjects before being tested on actual human beings. A very useful tool often implemented is the miniatur mouse model where diseases or disease-like symptoms are carried out on small mammals. Before any tests on apes or larger scale mammals such as pigs, mice and more generally rodents are the first subjects to be induced. For this study, the mouse model is very useful as we wish to analyse the demyelination of the Corpus callosum (CC) under Multiple sclerosis or Alzheimer and the cuprizone model has many similarities with real life observations in humans.

1.6.1 Cuprizone model

A number of complicated diseases have their roots in the demyelination or remyelination of the central nervous system, including Multiple sclerosis, Alzheimer's disease, schizophrenia (Davis, et al., 2003)[11], and traumatic brain injury (Brun and Englund, 1986)[8], (Kinnunen

et al., 2011)[34]. Disease progression and therapy efficacy could benefit from non-invasive, precise monitoring of demyelination and remyelination, which could be non-invasive. There is still a lot of work to be done in this field, despite the fact that biomarkers have come a long way (Galvin et al., 1976)[20],(Tomioka and Matsui, 2014)[67]. Cuprizone intoxication and recovery in mice has proven to be a useful tool for testing biomarker candidates for myelin alterations. Although cuprizone intoxication is characterized by extremely predictable dynamics and patterns in the brain, its molecular and cellular neuropathology has been widely investigated (Praet et al., 2014)[47]. An overdose of cuprizone causes OPC death and subsequent demyelination, especially in the CC and superior cerebral peduncles (Skripuletz et al., 2011)[58]. After five weeks of cuprizone feeding, the CC is completely demyelinated. Even after six weeks on a cuprizone diet, around half of the axons had spontaneous remyelination (Matsushima and Morell, 2001)[41]. Second complete demyelination occurs after 10 weeks and minor remyelination occurs at 12 weeks after cuprizone feeding. Remyelination of the CC occurs almost completely within six weeks following the cessation of acute or chronic intoxication (Matsushima and Morell, 2001)[41], (Skripuletz et al., 2008)[59]. OPC loss results in a significant inflammatory reaction. While microgliosis declines swiftly after the first three weeks of intoxication, astrogliosis remains elevated for weeks after the peak of 4.5–5 weeks (Matsushima and Morell, 2001)[41]; (Praet et al., 2014)[47]. Studying mice treated with cuprizone has the advantage of allowing researchers to compare in vivo MR biomarkers such as transverse relaxation time T2 or magnetization transfer ratio with histology, immunohistochemistry, or electron micrographs in order to identify prospective myelin biomarkers.

The requirement for in vivo investigations is critical for understanding the complicated interplay between different cells and dissecting the pathogenic pathways that contribute to the initiation and progression of disease. This is particularly essential in the case of Multiple sclerosis, which involves a large number of cell types from both the immune system and the central nervous system.

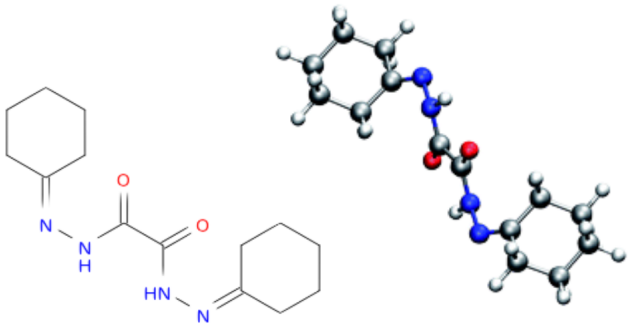

Figure 1.23: *Molecular structure of cuprizone*

It is also vital to conduct animal experiments throughout the preclinical phase of drug research in order to evaluate the toxicity and efficacy of novel medications. Despite the fact that mice and rats do not appear to be affected by Multiple sclerosis, mice and rats have been employed extensively in research on demyelination and axonal degeneration. This is despite the fact that the disease affects only humans. Consequently, models of the inflammatory cascade or demyelinating insults in the central nervous system have been constructed to recreate the primary pathogenic pathways that occur in the true disease. From (Patergnani et al., 2015) [46], Cuprizone [oxalic acid bis(cyclohexylidene hydrazide) or Bis(cyclohexanone)oxaldihydrazone] is a copper-chelating agent that is selective and sensitive. Cuprizone is used to cause toxic demyelination similar to that seen in Multiple sclerosis patients (Torkildsen et al., 2008)[68]. Young mice are fed a food containing $0.2-0.3$ percent cuprizone for 5–6 weeks in this relatively simple and effective model, which results in progressive demyelination in multiple brain areas. When mice are transferred to a normal diet, the demyelination process is reversed due to Oligodendrocyte progenitor cells (OPC)s' spontaneous remyelination (Van der Sar et al., 2012) [70]. Cuprizone administration causes significant OPC destruction, as well as microglial activation and severe astrocytosis (Pasquini et al., 2007)[44]. In the Myemouse project, the cuprizone model was used on different groups of mice. Depending on the group number, some mice were fed the drug during a certan time period, others were not. The precise model for the Myemouse project will be described in the following section.

1.6.2 Ethical statement

Before we go any further, we must express an ethical statement in regards to the mice that have been used for this study. In order to acquire histology and MRI data, the mice were placed under certain conditions and in the case of histology, perform a lethal procedure on them in order to acquire certain slices of their brains. According to the European legislation on animal protection and welfare:
The protection and welfare of animals is an area covered by a wide range of EU legislation. This includes the protection of wildlife, zoo animals, farm animals, animals in transport and animals used for scientific purposes. Animal studies, whether for the development or production of new medicines, for physiological studies, for studying environmental effects or for the testing of chemicals or new food additives, must be carried out in compliance with EU legislation.
We wish to declare that, in order to carry out this study, our rodents were treated in accordance with *DIRECTIVE 2010/63/EU OF THE EUROPEAN PARLIAMENT AND OF THE COUNCIL* and it's amendments for late 2019 experiments *REGULATION (EU) 2019/1010 OF THE EUROPEAN PARLIAMENT AND OF THE COUNCIL.*

We also would like to say, for our part, that the killing of certain mice is quite regrettable, but in our opinion vital as it is a necessary illness for a greater good in our world. Most scientific discoveries in biology have seen the light of day with the help of these little mammals. To them, we will be eternally grateful. We lastly would like to state that

the killing of the said mammals was carried out according to Article 6 of *DIRECTIVE 2010/63/EU*

1.7 Histology

Histology, formerly called microscopic anatomy, is the branch of biology and medicine that studies biological tissues using a microscope (Alturkistani et al., 2015)[2]. In histology, cells and tissues of animals and plants are studied by staining and sectioning them, and then viewing them under the microscope (electron or light microscope). To investigate the properties of tissues and the microscopic structures of cells, scientists employ a variety of techniques. Forensic investigations, autopsy, diagnosis, and education are all examples of situations in which histological examinations are applied. Furthermore, histology is widely employed in medicine, particularly in the study of damaged tissues to aid in the treatment of patients (Black, 2012)[7]. It takes five steps to complete the process of histological staining. These steps are as follows: fixation; processing; embedding; sectioning; and staining (Titford, 2009)[66]. Chemical, molecular biology assays, and immunological procedures have cumulatively resulted in significant advancements in the techniques employed for histological staining, which has considerably aided the study of organs and tissues in their natural environments (Shostak, 2013)[57]. Today, there exists a wide variety of stains that are used to identify different characteristics. For example, the gram stain is a sequential staining technique invented for differentiating bacterial species. The Giemsa stain is commonly-used in hematology for its superior ability to stain bone marrow, plasma cells, and mast cells. The Sudan Black dye stains lipid-containing structures like triglycerides and lipoproteins, a dark black or brown color. The Prussian blue stain is useful for identifying iron stores in the body. Myelin in nerve tissue can be visualized using the Luxol Fast Blue (LFB) staining method.

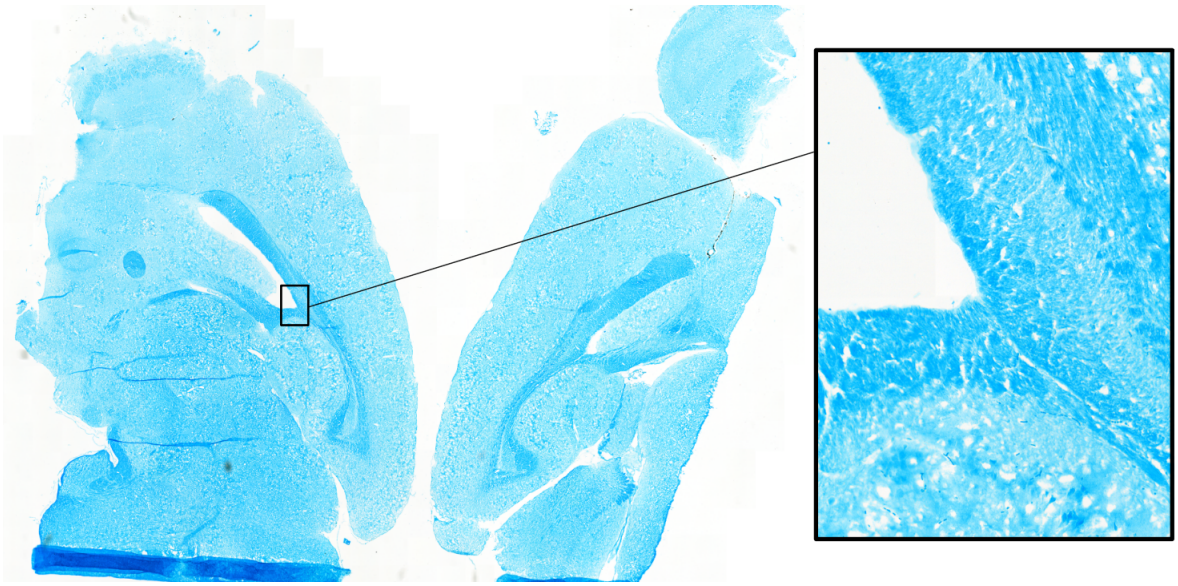

Figure 1.24: *Luxol Fast blue stain on mouse brain*

With this stain, it is possible to see myelin as well as the fatty substance in the brain known as white matter, which includes the axons of nerve cells, and to distinguish between them.

LFB staining, as a result, enables for the differentiation of white matter from grey matter in the brain. The acid-base process that causes LFB staining is straightforward. Luxol Fast Blue is a copper phthalocyanine dye that has been sulphonated. Alcohol dissolves this dye, and the dye is attracted to the bases found in the phospholipids of myelin, causing it to bind to them. A 95 percent ethanol solution is used to clean away any excess dye from the tissue segment, after which it is differentiated with lithium carbonate and 70 percent ethanol until the grey matter is colorless. The myelin is stained blue-green and the neurons are stained purple when using the rapid luxol blue staining method. When identifying basic neuronal structures in the brain and spinal cord (such as in this study), this staining technique is often utilized.

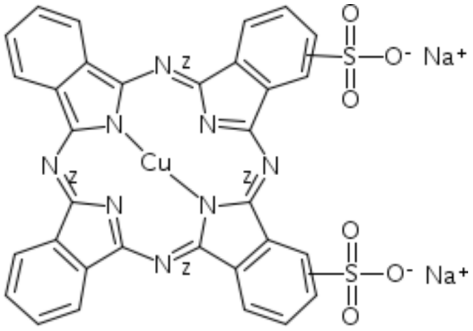

Figure 1.25: *Luxol Fast Blue molecule from DiscoFineChem*

However, before any analysis, let it be noted that a major drawback of LFB is the reaction time. Depending on the time difference between initial staining and observation, the staining intensity will vary. A short reaction time means a lighter blue intensity while a long reaction time will mean a deeper shade of blue. This means that two factors are involved in LFB staining; the presence of myelin and the time difference between staining and observation. This will be important in further section when analysis of LFB stained brains slices will be

carried out.

1.8 Anatomy

The mouse is the most commonly-used animal model in neuroscientific research, which is bolstered by the widespread usage of transgenic mouse models. Animal discoveries are confirmed in humans, and the exchange of information between both domains is critical to our understanding of the human brain.
Many prominent research institutes and collaborations have emerged as a result of advanced technologies like single-cell transcriptomics, epigenetic profiling, and diffusion MRI, with the goal of creating complete human or mouse brain atlases with data on gene expression, connectivity, and cell types. Using these projects, we will be more capable of building artificial intelligence tools in order to locate certain parts of the brain. We will be especially interested with Corpus callosum (CC) located between the cerebral cortex and the Hippocampus. When a subject is diagnosed with MS, lesions within the CC partially account for cognitive and upper-extremity dysfunction(Ozturk et al. 2010)[43]. Analysing the cuprizone mouse model in light of this fact may help us understand the underlying principles of CC degeneration from MS.

1.8.1 Decomposing the brain

Among the different parts of the brain we can distinguish different Region Of Interest (ROI) as shown Figure 1.26.

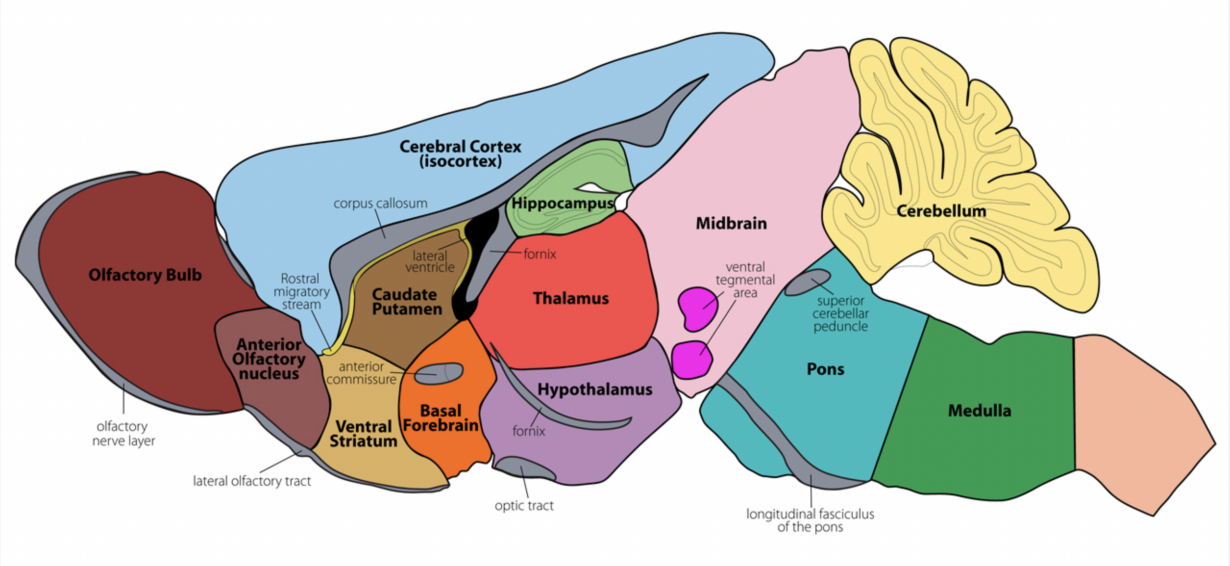

Figure 1.26: *Mouse brain Anatomy*

Cerebellum: A key component of the hindbrain of all vertebrates is known as the

cerebellum, which derives its name from the Latin word for "small brain." In most animals, the cerebellum is a smaller structure than the cerebrum; however, in other species, such as the mormyrid fish, it can be as large as or even larger than the cerebrum (Hodos, 2009) [24]. In humans, the cerebellum is an essential component in the process of controlling movement. It is possible that it is involved in some cognitive activities as well, such as attention and language, as well as emotional control, such as regulating fear and pleasure responses,(Wolf, 2009)[73],(Schmahmann, 2009)[56], although the functions connected to movement are the ones that have the greatest evidence to support them. The human cerebellum does not play a role in the initiation of movement, but it does contribute to coordination, precision, and accurate timing. The cerebellum receives input from the sensory systems of the spinal cord as well as from other parts of the brain, and it integrates this information in order to fine-tune motor activity. In humans and other mammals, dysfunctions in fine movement, equilibrium, posture, and motor learning can result from injury to the cerebellum.

Cerebral Cortex: In humans and other mammals, the cerebral cortex, also known as the cerebral mantle, is the outer layer of neuronal tissue of the cerebrum of the brain. The six-layered neocortex makes up the majority of the cerebral cortex, with allocortex accounting for only 10% (Strominger, 2012)[63]. The longitudinal fissure that divides the cerebrum into the left and right cerebral hemispheres separates it into two cortices. The corpus callosum connects the two hemispheres beneath the cortex. The cerebral cortex is the central nervous system's greatest neuronal integration location (Saladin, 2011)[53]. Attention, perception, awareness, thought, memory, language, and consciousness all rely on it. The cerebral cortex is folded in most mammals, with the exception of small mammals with small brains, to provide more surface area in the cranium's constrained volume. Cortical folding is important for the wiring of the brain and its functional organization, in addition to reducing brain and cranial volume. There is no folding and the cortex is smooth in mammals with small brains (as rodents). (Fernandez, 2016)[16], (Rakic and Pasko, 2009)[48]. Movement in the motor cortex and sight in the visual cortex are examples of cortical functioning.

Thalamus: The thalamus (from Greek $\theta\alpha\lambda\alpha\mu o\zeta$, "chamber") is a massive gray matter mass found in the diencephalon's dorsal portion (a division of the forebrain). Nerve fibers project in all directions from the thalamus to the cerebral cortex, allowing for hub-like information exchanges. It has various roles, including conveying sensory signals to the cerebral cortex, including motor signals, and regulating awareness, sleep, and alertness. It is a paramedian symmetrical structure with two halves (left and right) located between the cerebral cortex and the midbrain in the vertebrate brain. It is the principal result of the diencephalon during embryonic development, as first recognized by Swiss embryologist and anatomist Wilhelm His Sr. in 1893. [33]

Olfactory Bulb: The olfactory bulb, also known as the bulbus olfactorius in Latin, is a neuronal structure located in the forebrain of vertebrates that plays an important role in olfaction, also known as the sense of smell. It relays information about smells to other parts

of the brain, such as the amygdala, the orbitofrontal cortex, and the hippocampus, where it is involved in emotional processing, memory formation, and new information acquisition. The bulb is composed of two separate structures, which are referred to as the primary olfactory bulb and the accessory olfactory bulb. Both the piriform cortex of the primary olfactory cortex and direct projections from the main olfactory bulb to particular amygdala locations are involved in the connection between the amygdala and the main olfactory bulb. A parallel pathway is formed by the auxiliary olfactory bulb, which is located on the dorsal-posterior area of the main olfactory bulb. If the olfactory bulb is damaged or destroyed, the patient will experience ipsilateral anosmia. Irritative lesions of the uncus, on the other hand, might cause olfactory and gustatory hallucinations. On the other hand, the olfactory bulb also gets "top-down" information from other parts of the brain, including the amygdala, neocortex, hippocampus and others. Its potential functions can be placed into four non-exclusive categories (Mori, 2005)[42]:

1 discriminating among odors

2 enhancing sensitivity of odor detection

3 filtering out many background odors to enhance the transmission of a few select odors

4 permitting higher brain areas involved in arousal and attention to modify the detection or the discrimination of odors.

Hypothalamus: The hypothalamus (from Ancient Greek $\upsilon\pi o$(hupó) 'under', and $\theta\alpha\lambda\alpha\mu o\zeta$ (thálamos) 'chamber') is a region of the brain that contains a number of small nuclei with a range of activities. Through the pituitary gland, the hypothalamus is responsible for establishing a connection between the neurological system and the endocrine system, which is among the most significant roles it plays. The hypothalamus is a component of the limbic system and can be found below the thalamus in the brain. According to the language of neuroanatomy, it is the region of the diencephalon that is located in the ventral section. The hypothalamus is present in the brains of all vertebrates (Laurence et al., 2021)[36] It is around the size of an almond (about 2cm depending on the kind of almond) in human beings and the size of a flee (around 1mm) in mice. Certain metabolic processes and other actions of the autonomic nervous system are controlled by the hypothalamus, which is responsible for the regulation of these processes. It is responsible for the synthesis and release of certain neurohormones, which are referred to as releasing hormones or hypothalamus hormones. These hormones, in turn, either promote or inhibit the pituitary gland's production of hormones. The hypothalamus is responsible for regulating critical parts of parenting and attachment behaviors, as well as body temperature, thirst, and appetite. (NCI Dictionary of Cancer Terms from National Cancer Institute) exhaustion, the importance of sleep, and circadian rhythms (Saper et al., 2005)[54]

Hippocampus: One of the most important parts of the brains of humans and other animals is called the hippocampus, which derives its name from the Greek word for seahorse.

Both sides of the brain include a hippocampal formation, one on each side in humans and other mammals. The hippocampus is a part of the limbic system and plays a vital function in the consolidation of information from short-term memory to long-term memory. It also plays a role in the spatial memory that facilitates navigation. Both in humans and in other primates, the hippocampus is found in the allocortex, and it sends neuronal projections into the neocortex(Martin, 2021)[40]. The hippocampus is a structure that may be found in all vertebrates. It is also known as the medial pallium (Bingman,2009)[6]. The hippocampus proper, also known as Ammon's horn, and the dentate gyrus are the two primary interlocking elements that make up this structure in human beings [10]. The hippocampus is one of the first regions of the brain to undergo damage in Alzheimer's disease (and other forms of dementia);(Dubois et al., 2016)[14] short-term memory loss and disorientation are listed among the early signs of the disease. Other conditions that can cause damage to the hippocampus include oxygen deprivation (hypoxia), encephalitis, and epilepsy that affects the medial temporal lobe. Anterograde amnesia is the inability to acquire new memories and to keep those memories intact. It can occur in people who have suffered substantial damage to both of their hippocampi.
The hippocampus has frequently been utilized as a model system for the study of neurophysiology. This is due to the fact that the numerous neuronal cell types are neatly organized into layers within the hippocampus. Long-term potentiation, is a type of neuronal plasticity that was first discovered to take place in the hippocampus. This structure has also been the focus of a significant amount of research. It is generally agreed upon that long-term potentiation is one of the primary neuronal mechanisms in the brain that is responsible for the storage of memories. The hippocampus, which is a component of the brain system that is important for spatial memory and navigation, has been the subject of substantial research using rats as model animals. The hippocampi of rats and mice include a large number of neurons that respond as place cells. This means that these neurons release bursts of action potentials whenever the animal travels through a particular region of its surroundings. Place cells in the hippocampus have substantial interactions with head direction cells, the activity of which functions as an inertial compass, and it is conjectured that place cells in the adjacent entorhinal cortex have interactions with grid cells.

Caudate putamen: The putamen (Latin for "nutshell") is a circular structure near the base of the forebrain (telencephalon). The dorsal striatum is made up of the putamen and the caudate nucleus. It's also one of the basal nuclei's constituent structures. The putamen is related to the substantia nigra, globus pallidus, claustrum, and thalamus, as well as several parts of the cerebral cortex, via multiple routes. The putamen's principal purpose is to control and impact many types of learning by regulating movement at various stages (e.g. preparation and execution). Its actions are carried out by GABA, acetylcholine, and enkephalin. The putamen also has a function in neurodegenerative diseases like Parkinson's disease.

Midbrain: The midbrain (mesencephalon in Greek) is considered part of the brainstem. Its substantia nigra is closely associated with motor system pathways of the basal ganglia. The human mesencephalon is archipallian in origin, meaning that its general architecture

is shared with the most ancient of vertebrates. Dopamine produced in the substantia nigra and ventral tegmental area plays a role in movement, movement planning, excitation, motivation and habituation of species from humans to the most elementary animals such as insects. Laboratory house mice from lines that have been selectively bred for high voluntary wheel running have enlarged midbrains.[13] The midbrain helps to relay information for vision and hearing.

Fornix: The fornix (Latin for "arch") is a C-shaped bundle of nerve fibers in the brain that serves as the hippocampus's main output tract. The fornix also transports afferent fibers from the diencephalon and basal forebrain to the hippocampus. The limbic system includes the fornix. While its specific function and importance in brain physiology are still unknown, surgical transection — the severing of the fornix along its whole length – has been shown in humans to cause memory loss. There is some controversy about which types of memory are impacted by this impairment, however recall memory has been found to be more closely related than recognition memory. Damage to the fornix can make it harder to recall long-term knowledge like specifics from past events, but it has little influence on the capacity to recognize items or circumstances.

Corpus callosum (CC): The Corpus callosum is a substantial bundle of nerve fibers that connects the two hemispheres of the brain. This connection guarantees that both sides of the brain are able to communicate with each other and transmit information to one another. This neural highway facilitates the continuous exchange of information involving the senses, the motor system, and the cognitive processes between the two hemispheres of the brain. An average CC has somewhere in the neighborhood of 300 million axons, often known as nerve fibers. It is around ten centimeters in length at the midline and can be found in the white matter of the cerebrum. This neural bridge is the greatest white matter structure in the brain and only evolved in placental mammals, who are the only mammals to have given birth. If the CC is severed, the two halves of the brain are unable to interact with one another in an effective manner, which can lead to the impairment or loss of a wide variety of abilities, including changes in visual perception, speech, and memory. In cases of untreatable epilepsy, a surgical procedure called severing the CC is sometimes done as a last resort in order to halt seizures from spreading across the brain.

Cingulum: The cingulum is a nerve tract — a bundle of axons – that connects the cingulate gyrus in the brain to the entorhinal cortex in the brain, providing communication between limbic system components. It runs from the frontal lobe's subcallosal gyrus beneath the rostrum of the corpus callosum to the temporal lobe's parahippocampal gyrus and uncus, forming the white matter core of the cingulate gyrus. Afferent fibers from the regions of the thalamus associated with the spinothalamic tract reach cingulum neurons. Here, function and structural changes are linked, implying that any change in this structure will result in a change in function, notably behavioral due to its emotional function. This, together with the fact that the cingulum is a key component in learning to correct errors, suggests that the cingulum is involved in pain evaluation and reinforcement of pain-relieving behavior.

Cingulotomy is a type of psychosurgery that involves severing the anterior cingulum. It is used to treat depression and OCD. The cingulum is important in this study because, being placed right next to the CC, it may affect our analysis on histology data. This will be developed later on. The cingulum was one of the first brain structures to be discovered.

1.8.2 Neuronal grid

Neurons, along with the glial cells that provide structural and metabolic support, are the main components of the nervous system. The central nervous system, which comprises the brain and spinal cord, and the peripheral nervous system, which includes the autonomic and somatic nervous systems, comprise the nervous system. The bulk of neurons in vertebrates are found in the central nervous system, although some are found in peripheral ganglia, and many sensory neurons are found in sensory organs like the retina and cochlea. Axons in the peripheral nervous system can form fascicles, which make up nerves (like strands of wire make up cables). Tracts are clumps of axons in the central nervous system.

Neurons are highly specialized for cellular signal processing and transmission. Because of the range of activities they serve in different regions of the nervous system, their shape, size, and electrochemical characteristics vary greatly. A neuron's soma, for example, might be anywhere from 4 to 100 micrometers in diameter.

- The soma are the neuron's body. The nucleus is where the majority of protein synthesis takes place. The nucleus can have a diameter of 3 to 18 micrometers.
- The dendrites of a neuron are cellular extensions with several branches. The overall shape and structure is referred to as a dendritic tree figuratively. The dendritic spine is where the majority of the input to the neuron occurs.
- The axon is a finer, cable-like projection that can span tens, hundreds, or even thousands of times the soma diameter in length. The axon is responsible for carrying nerve signals out from the soma as well as some sorts of information back to it. Many neurons have only one axon, but this axon can — and generally does — branch extensively, allowing communication with a large number of target cells.
- The axon terminal is found at the end of the axon farthest from the soma and contains synapses. Synaptic boutons are specialized structures where neurotransmitter chemicals are released to communicate with target neurons. In addition to synaptic boutons at the axon terminal, a neuron may have en passant boutons, which are located along the length of the axon.

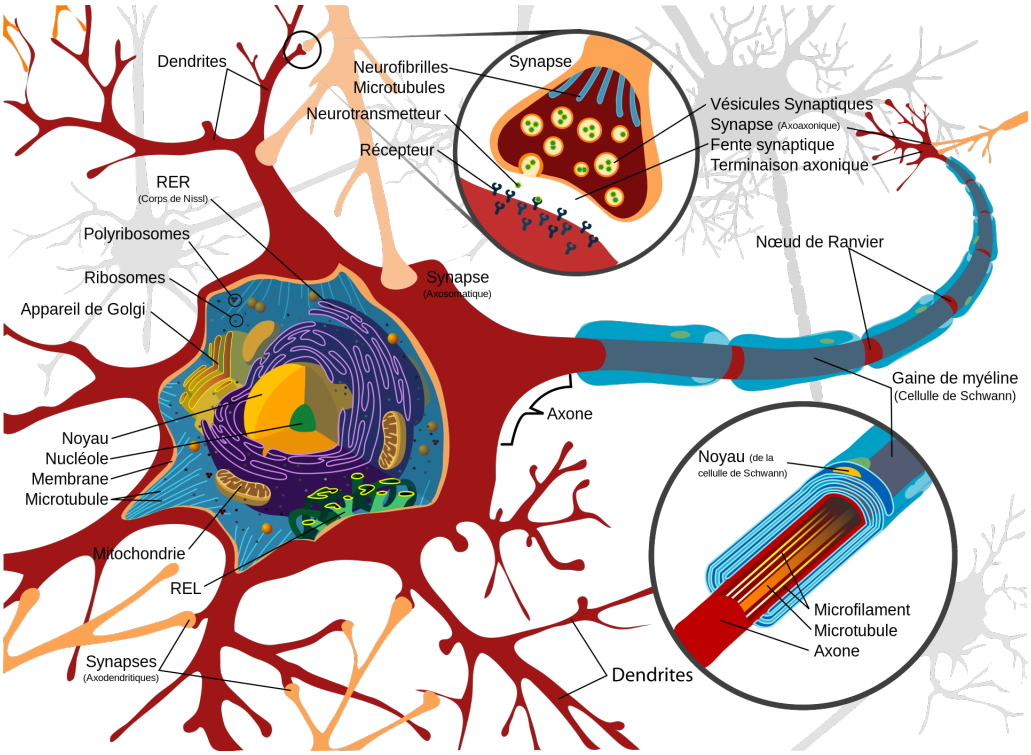

Figure 1.27: *The composition of the Neuron grid*

The conventional conception of the neuron assigns specific functions to each of its anatomical components; yet, dendrites and axons frequently act in ways that contradict their so-called primary purpose (AM Roberts, 2010)[51]. The central nervous system's axons and dendrites are normally only one millimeter thick, but the peripheral nervous system's are significantly thicker. The soma have a diameter of 10–25 micrometers and are often not much bigger than the cells nuclei they contain. A human motor neuron's longest axon can be almost a meter long, extending from the base of the spine to the toes.

Chapter 2

Convert and process pipeline

This section will be devoted to the pipeline that was written for the Myemouse project. Its main goal is to process data output by the Bruker machine and preprocess it before we input it in micro-structural algorithms in a general manner. As any medical study, before tryouts on humans, research often uses small mammals such as rodents to carry out experiments or specific research on induced diseased (when this is possible). The Myemouse project aims to evaluate de myelin degeneracy within the mice brain by using (Rensonnet et al,2019)[49] fingerprinting pipeline and confirming the findings with histoligical data acquired on the said mice. The further goal of this study is to use fingerprinting in human cases of drug abuse or Multiple sclerosis in order to better understand it, predict it and if possible cure it. In order to lead this experiment, a specific model was selected to best capture the myelin loss. A certain number of mice were fed cuprizone, a drug specifically used to induce myelin loss in rodents.

2.1 Myemouse Project Parameters

Over a theoretical period of 12 weeks (in reality due to Covid-19, the experiment spanned over 16 weeks), 24 mice were divided into four distinct groups and subjected to four different treatment regimes, as represented in Figure 2.1. This was done in order to investigate the variation in myelin within the corpus callosum and the health between mice fed with cuprizone and mice fed with a healthy diet. As stated in Section 1.6.1, the cuprizone model will induce a MS-like myelin depletion in the mouse's brain.

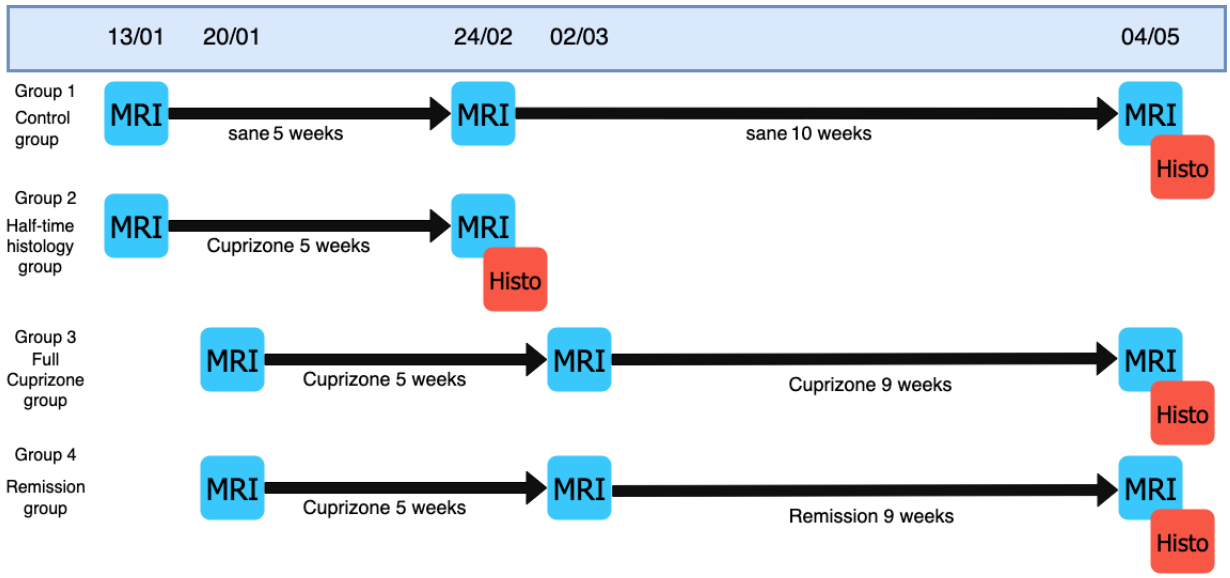

Figure 2.1: *Timeline summarizing the mice regimes, the MRI acquisition sessions and the histology periods.*

Three of the groups consisted of mice that had been fed curprizone for a specific period of time, while one group served as a control. More specifically, at a specific point in time, MRI images of each individual mouse were acquired; and following the last acquisition, the mice were perfused with a lethal injection, their nervous systems (i.e. their brains and spinal cords) were extracted, and they were immediately frozen in preparation for the histological investigation. In addition, the mice were numbered in accordance with the stamping pattern depicted on this image, which was summarized in the 2.1. Furthermore, for the MRI acquisitions, three main acquisitions were carried out. Prior to those acquisitions, a localizer scan and a multiple slice T2-weighted scan were carried out, respectively, in order to position correctly the mice and to determine the slice of interest.

It should be noted that the acquisition file type for all medical images is DICOM. Most machine export in DICOM. The machine we used for the Magnetic Resonance Imaging, (the Bruker 11.7 Tesla BioSpin MRI 117/155 ParaVision 6.0.1), is no exception. It should also be noted that this machine has a specific feature; it is limited by an image acquisition of 400 000 voxels divided between the three directions (x, y, z). Thus our MRI images will be in the form of $200 \times 200 \times 10$ images.

A particularity of our data is that each dataset is taken from several shells. A shell is an acquisition range with a certain b value that is associated to a three-dimensional space vector (bvec). In each shell, a sequence of 32 images are taken with the same bval. Each image is taken with different bvec i.e space vectors oriented in different directions. The reprentation of a shell acquisition can be seen in Figure 2.2 where each white dot in the single shell configuration represents an acquisition with three different space vectors. The same bval is kept through the shell. In our case, we have multiple shells combined

(represented in the muti shell scheme). The ball of color show each shell for different bval. Therefore we can imagine a bval of 750 for the red dots (there are 32 for 32 space different space directions), a bval of 1000 for the green balls (again 32 of them) and a bval of 1200 for the blue balls. The fact that the radius seems to grow when the bval grows is just an illustration to better understand and the real mechanics of the MRI are better represented in the combined multi-shell scheme in Figure 2.2 where all the dots are on the same sphere.

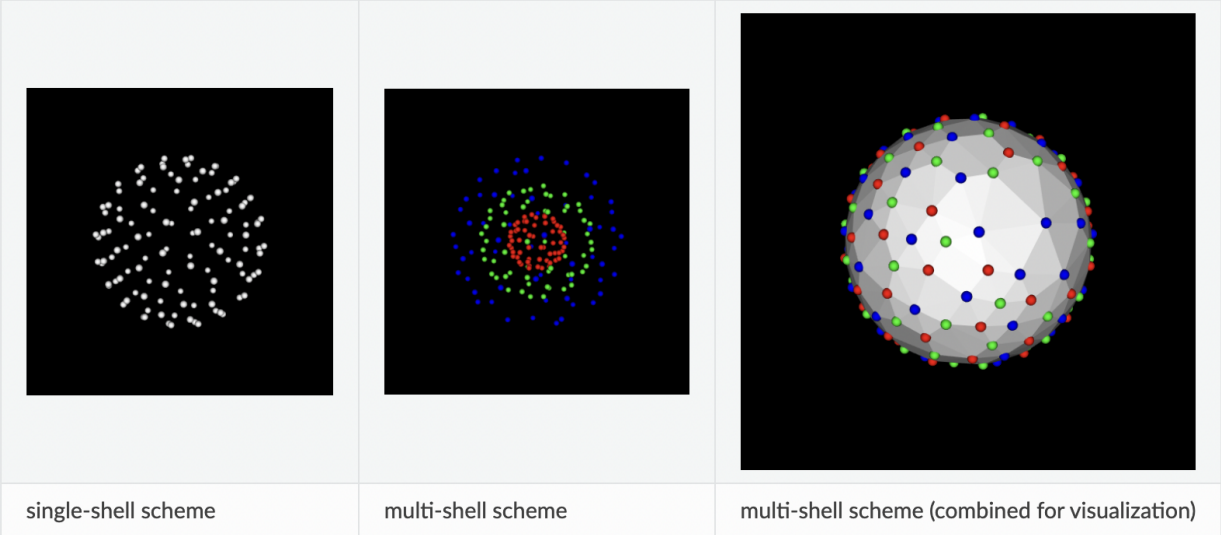

Figure 2.2: *Multi-shell representation for MRI*

We worked with four shells (i.e four different bval) (700, 1500, 2000, 2500) 2.2. For the first two shells (700, 1500), we have 64 bvec and for the last two (2000, 2500), we have 128. The Bruker machine can take only 32 bvec and always begin with a B_0 localiser (3 bval=0). So, we finally have 13 shells separeted by B_0 localisers for a total of 424 acquisitions (i.e 424 bvec) associated to one of the four bval.

$$\begin{aligned} 424\ b_{val} =& B_0 + 1\ b_{val}(0) + 2 \times [B_0 + 32\ b_{val}(700)] + 2 \times [B_0 + 32\ b_{val}(1500)] \\ &+ 4 \times [B_0 + 32\ b_{val}(2000)] + 4 \times [B_0 + 32\ b_{val}(2500)] \end{aligned}$$

2.2 Main conversion Pipeline

2.2.1 From the machine to organized folders

An important part of this study was to make sense and clean up the wad of files output by the machine after each acquisition. The very first step that needs to be done is to convert the DICOM files into files known as Neuroimaging Informatics Technology Initiative (NifTi) files, which are more straightforward to process and examine. In the field of biomedical analysis, this modification has been practiced for some time; hence, we based our conversion on previously completed studies.

In addition, the Bruker system that we utilized filed these distinct shells in separate files, despite the fact that they were captured using the same mouse. Therefore, in order to convert our data, we would go through all of our files and convert each one of them individually into NifTi. However, we were also required to combine the shells that were part of the same transaction. And most importantly, locate the bvals as well as the corresponding bvectors in order to construct an accurate NifTi file.

Once we were familiar with the structures and functions, this work was not difficult, but it was exceedingly time-consuming and tedious. In the end, despite the fact that we had successfully resolved each issue one at a time, the NifTi files were of poor quality. This was due to the fact that the conversion function that we made use of was incompatible with the DICOM files produced by the Brukere machine.

After relaying this information to the doctoral candidates who were in charge of watching us, they searched the available literature and came up with a ready-made function that was practically identical to what we want.

Now, in order to convert our files, we will use the open source Bruker2nifti function (Ferraris, 2017)[17].

Once this step is done, we go through the freshly converted files and classify them according to their acquisition methods: DtiEpi, FLASH, RARE, MSME, FieldMap, nmr-suDtiEpi.

- DtiEpi : Echo planar (EPI) for diffusion tensor imaging (DTI) is the fastest acquisition method in MRI (100 ms/slice), but with limited spatial resolution. It is based on: an excitation pulse, possibly preceded by a preparation of the magnetization, a continuous acquisition of the signal in the form of a train of gradient echoes (single shot or segmented acquisition), and reading and phase gradients adapted for the spatial coding of the image, with several possible trajectories (constant or intermittent phase coding gradient, spiral acquisition...)

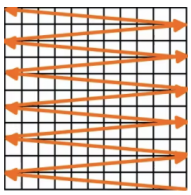

Figure 2.3:
DtiEpi constant

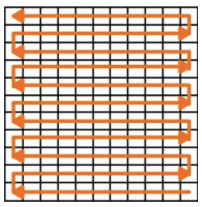

Figure 2.4:
DtiEpi intermittent

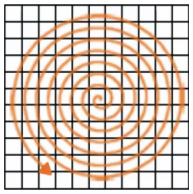

Figure 2.5:
DtiEpi spiral

- FLASH : Fast low angle shot Magnetic Resonance Imaging (FLASH MRI) is a particular sequence of magnetic resonance imaging with a short repetition time. It is the generic form of steady-state free precession imaging. It is used as a three-dimensional acquisition to visualise complex anatomical structures (such as the brain) with unprecedented high spatial resolution in three dimensions and in arbitrary view directions.

- RARE : Rapid Imaging with Refocused Echoes, which is also known as Fast Spin-Echo (FSE) or Turbo Spin-Echo (TSE) depending on the manufacturer, is a well established technique for rapid imaging that speeds up image acquisition by acquiring more than one k-space line per repetition. RARE is also known as "Rapid Imaging with Refocused Echoes." A pulse is used to refocus dephasing spins into an echo at the beginning of a RARE-type sequence, which is the same method that is employed at the beginning of the well-known spin-echo sequence.

- MSME : Multi-Slice-Multi-Echo is a T2 acquisition method, as described in section 2.1.1, on multiple slice simultaneously.

- FieldMap : This is an acquisition that makes it possible to process field mapping using methods like SPM and FSL. After image processing, it is used to correct offline any distortion that may have occurred. The gradient echo approach is used to acquire two single T2-weighted images that are taken by the field mapping scanner.

- nmrsuDtiEpi : It is exactly the same as DtiEpi but the only difference is in the acquisition settings, which involve multiplying the phase-encoding vector by a factor of -1. Because of this, we refer to them as reverse-enconding. This acquisition is used to avoid stretching or contracting in all three directions of space. The fig. 2.6 is an example with vector $[0.12, 1, -0.07]$ and $[-0.12, -1, 0.07]$ as reverse. Where we can see a large distortion along the y-axis.

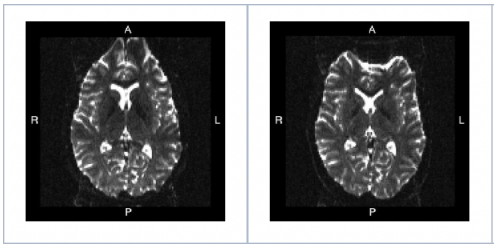

Figure 2.6: *reverse-enconding*

2.2.2 Capturing the essential files

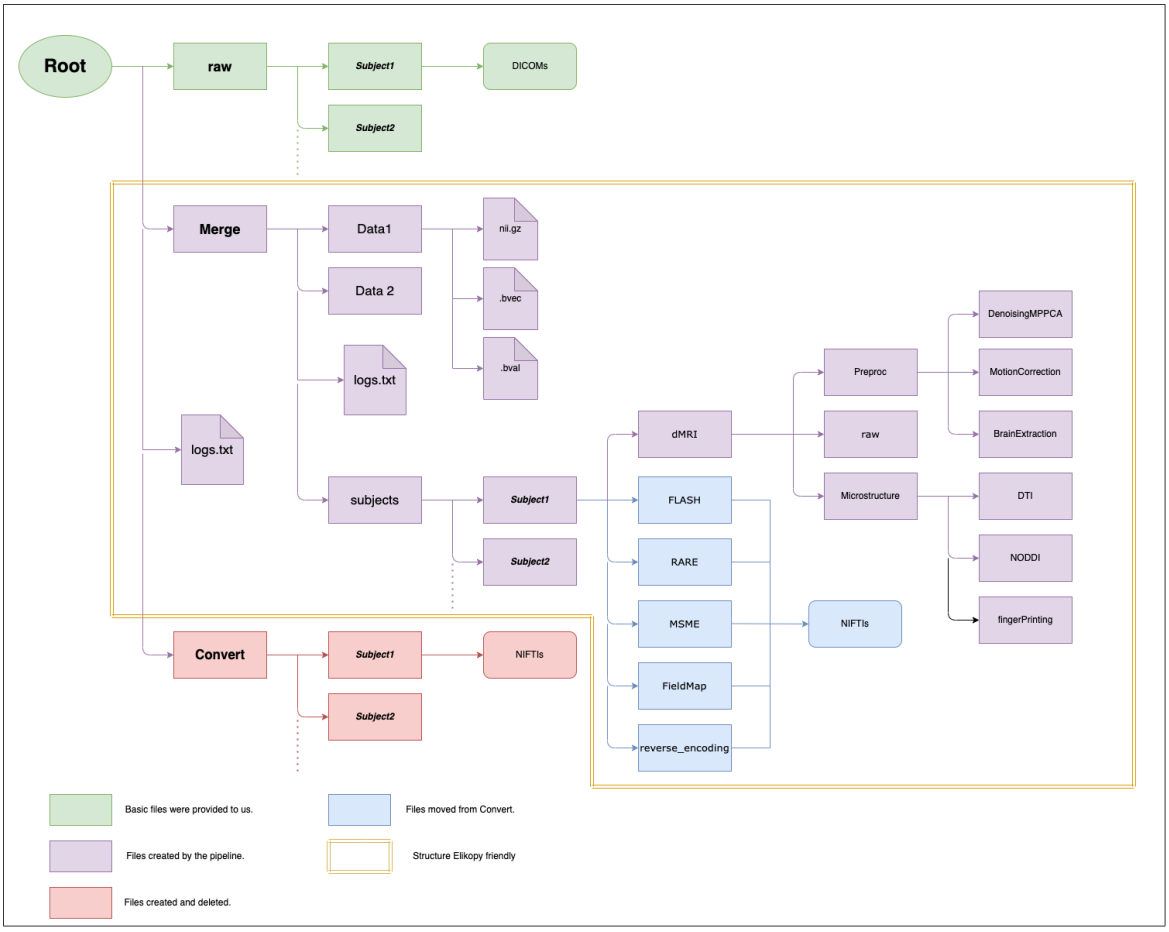

Figure 2.7: *Structure diagram*

With studies like this one and a growing number of MRI files, there is a need for cleanliness and order in our file hierachy. In order to loose as many useless files as possible and only capture the essential; a strategy was set in place to channel and concentrate all important files to one specific central location. This central location is the `Merge` directory that will stand as laying stone for the Elikopy compatible structure. However, important files as discribed in the previous section (such as `MSME`, `FLASH` or `FieldMap`) need to be kept. Therefore, once these essential files have been moved (in light blue Figure 2.7), the `Convert` files in red will be deleted from computer space in order to save memory. In this study, this file alone took about 100 gigabites. Needless to say, if we can delete unused or useless files, the program will execute and save memory.

2.3 Data correction process

2.3.1 Denoising

Context

The newly NifTi converted and relocated images are still full of noise. The point of creating the Elikopy compatible set-up is to run prepared algorithms (such as DTI) on our data set. However, before this set, we must denoise, correct and extract the brain. This will also be done by our program once again mimicking the Elikopy structure. In order to lead a valid microstructural analysis, it is first necessary to remove any noise that would parasite all following procedures. The following section will explain the denoising procedure and explore the mathematical aspects. Furthermore it will justify the order of preprocessing applications (denoise, motion correct and extract) that has been implemented.

Explanation

The input images are denoised by applying the Marchenko-Pastur Principal Component Analysis (MPPCA) approach that is implemented in DIPY. This is done in order to remove the noise that is commonly observed in MRI. We decided to go with this approach since it is an algorithm for denoising that is both quick and accurate, and it does not cause the image to become blurry or produce artifacts.

Figure 2.8 represents the denoising step at two different moments of the process. On the left, the denoising step is the very first preprocessing step to be executed. as a result, the image is clear. On the right, the denoising step is carried out at the very end in order to decrease execution time as the noisy image is now reduced to the brain. Clearly the left side yields better results. It is now evident that the denoising step must be carried out before any other preprocessing step. But why? Because it is dependent on the noise being uncorrelated both spatially and among progressive acquisitions, it is essential that the denoising step be conducted at the primary stage of the pipeline. Performing this step after a step that utilizes interpolation to recreate pictures would result in correlated noise and a failure of the assumptions that MPPCA removes only thermal noise without modifying anatomical features. Under the framework of the random matrix theory-based method of Principal component analysis noise reduction, this assumption is carried out.

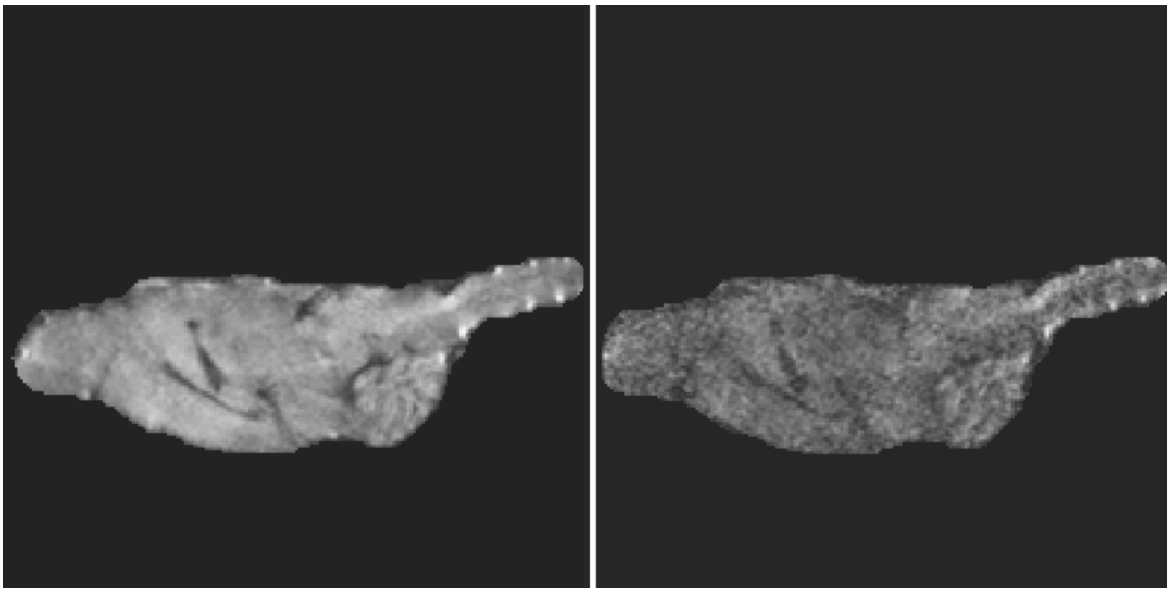

Figure 2.8: *first step denoising vs last step denoising*

The denoising process relies on PCA of a $M * N$ matrix X, with rows representing M voxels within a sliding window, and columns representing N weighted magnitude MR measurements in each voxel. This matrix is assumed large (i.e. $R = \min(M, N) >> 1$).

$$\Sigma_X = \frac{1}{N} X X^T = U \Lambda^2 U^T$$

Σ_X is the matrix that represents the covariance of X; U is an orthonormal matrix that may be used to produce uncorrelated data; Λ is the matrix that represents the eigenvalues of Σ_X, and is the matrix that represents the correlation in the space of uncorrelated data.

The dMRI data is very redundant because of correlations between the diffusion weighted signals, and it may be interpreted as a linear combination of a few $P << R$ linearly independent sources. This is because the correlations between the signals are what cause the diffusion weighting. Therefore, if there was no background noise present, PCA would only produce P eigenvalues that were not zero. In actuality, there are no data that are devoid of noise. The noise travels through the PCA, and all of the R eigenvalues are not zero (which indicates that the matrix has a rank of R). However, despite the fact that the noise is unpredictably distributed, the contribution that it makes to the histogram of eigenvalues becomes predictable when P is smaller than R. The part of PCA eigenvalues due to Gaussian noise with variance σ^2 and zero mean is given by the Marchenko-Pastur distribution :

$$p(\lambda|\sigma, \gamma) = \frac{\sqrt{(\lambda_+ - \lambda)(\lambda - \lambda_-)}}{2\pi\gamma\lambda\sigma^2} \text{ if } \lambda_- < \lambda < \lambda_+$$

It is important to keep in mind that the degree of noise can cause some of the P significant eigenvalues to fall into the MP bulk and become indistinguishable from noise. This happens depending on the quantity of noise.

In practice, the noise has a Rician (i.e. module of a complex gaussian) distribution rather than a Gaussian one . Therefore, it is consistent with a distribution with L degrees of freedom that has a mean that is not zero.

The PCA theory may be used to create an estimate of the noise variance after denoising if it is assumed that the M lowest eigenvalues have been cancelled out.

$$\tilde{\sigma}^2 = \sigma^2 - P_\sigma = \sigma^2 - \Sigma_{i=P+1}^{M} \frac{\lambda_i}{M}$$

After denoising, the SNR is expressed as a scale in $\sqrt{\frac{M}{P}}$. The value of P cannot be determined in advance and will be based on the degree to which the data are redundant.

Finally, it is important to note that in order to expedite the process of applying this very complex algorithm to each of our images, we made use of a multi-treading method who launches a MPPCA by shell . And despite all of that, this phase of the preparation is still the most time-consuming phase of the entire preprocessing.

The implementation of the MPPCA algorithm on our mouse brains is depicted in the figure that is presented below.

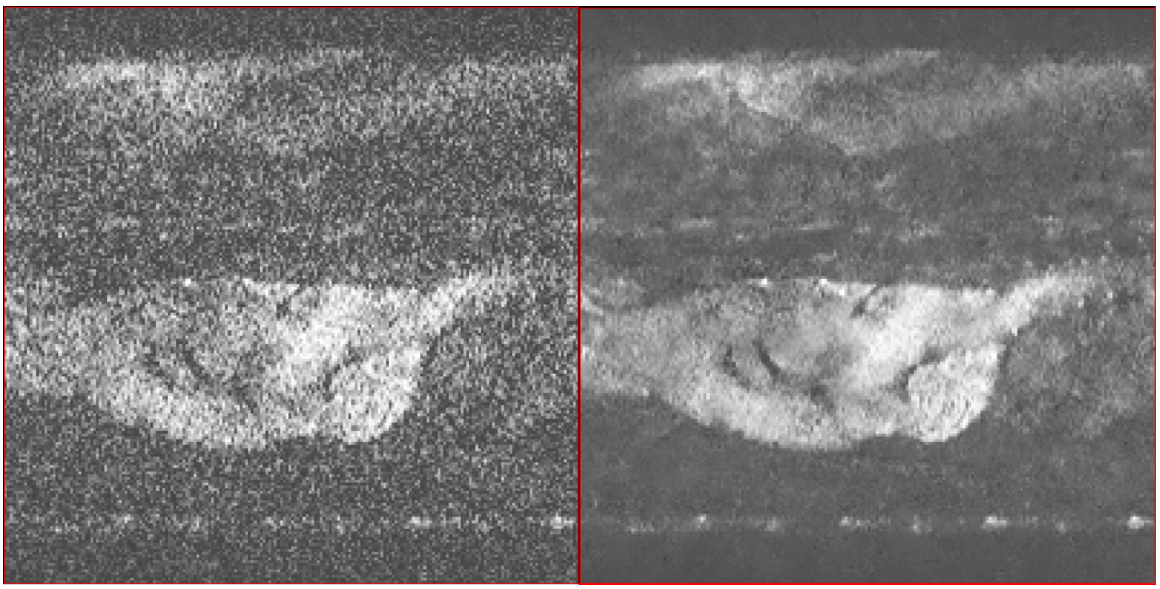

Figure 2.9: *The denoising step is essential as it clears all the snowy particles (left image). The right image is therefore ready to be used.*

Code and parameters

```
from dipy.denoise.localpca import mppca
denoised = mppca(data, patch_radius)
```

This is the function used to denoise our images. It is taken from the Diffusion Imaging in Python (DIPY) package (Garyfallidis et al., 2014)[21] and is quite reliable for such problems.

1 `data` : The brain data of the image.

2 `patch_radius` : The size of the sliding window. The default is 2.

For one mouse, this function take on average 1 hours 30 minutes and 20 seconds on a MackBook Pro (processor : dual-core Intel i7 with 3,5 GHz).

2.3.2 Motion correction

Context

During the acquisition process, it is possible for the pictures to shift slightly from shell to shell as a result of a minor change in calibration, a jolt, or the mouse's breathing. In order to overcome this problem, we performed a motion correction. We take as reference the first image of bval = 0, then we calculate the recalibration by affine transformation on the bval = 0 of the following shell. Then we apply this transformation to the whole shell in order to realign it to the first one. And we follow this procedure for each of the subsequent shells.

Explanation

Before going into detail, a quick word on affine transformations.

In theory, transformation function can be a complicated non-linear function, but in practice, we know that the scanner collects data on a regular grid. This means that the relationship between (i,j,k) and (x,y,z) is linear and can be encoded by a diagonal 3 by 3 matrix. A zoom can be applied as follows using the matrix below. The first dimension will then be scaled by p, the second by q and the third by r units:

$$\begin{bmatrix} x \\ y \\ z \end{bmatrix} = \begin{bmatrix} pi \\ qj \\ rk \end{bmatrix} = \begin{bmatrix} p & 0 & 0 \\ 0 & q & 0 \\ 0 & 0 & r \end{bmatrix} \begin{bmatrix} i \\ j \\ k \end{bmatrix}$$

The scaling of a point is a special case of this matrix where $p = q = r = \beta$ and the previous equation can simply be rewritten as:

$$\begin{bmatrix} x \\ y \\ z \end{bmatrix} = \beta \begin{bmatrix} i \\ j \\ k \end{bmatrix}$$

We can also apply a rotation matrix R_α. Rotations can take place around the 3 axis $\bar{\mathbf{x}}$,$\bar{\mathbf{y}}$ and $\bar{\mathbf{z}}$. We can then define each R for each axis; for example, a rotation by θ radians around

the third array axis, a rotation by ϕ radians around the second array axis and a rotation by γ radians around the first array axis are given by the matrices:

$$R_z = \begin{bmatrix} cos(\theta) & -sin(\theta) & 0 \\ sin(\theta) & cos(\theta) & 0 \\ 0 & 0 & 1 \end{bmatrix} \; R_y = \begin{bmatrix} cos(\phi) & 0 & sin(\phi) \\ 0 & 1 & 0 \\ -sin(\phi) & 0 & cos(\phi) \end{bmatrix} \; R_x = \begin{bmatrix} 1 & 0 & 0 \\ 0 & cos(\gamma) & -sin(\gamma) \\ 0 & sin(\gamma) & cos(\gamma)) \end{bmatrix}$$

Once these matrices are defined, one can express the rotation a point in the inertial referential as follows:

$$\begin{bmatrix} x \\ y \\ z \end{bmatrix} = R_\alpha \begin{bmatrix} i \\ j \\ k \end{bmatrix}$$

Where the parameter α represents one of the three axis around which the point revolves. In the same manner, we can apply a shear with the matrix:

$$\begin{bmatrix} x \\ y \\ z \end{bmatrix} = \begin{bmatrix} 1 & C_x & 0 \\ C_Y & 1 & 0 \\ 0 & 0 & 1 \end{bmatrix} \begin{bmatrix} i \\ j \\ k \end{bmatrix}$$

All of this transformation can be made with one unique matrix by matrix multiplication. Name this matrix M.

$$M = \begin{bmatrix} p & 0 & 0 \\ 0 & q & 0 \\ 0 & 0 & r \end{bmatrix} \begin{bmatrix} cos(\theta) & -sin(\theta) & 0 \\ sin(\theta) & cos(\theta) & 0 \\ 0 & 0 & 1 \end{bmatrix} \begin{bmatrix} 1 & C_x & 0 \\ C_Y & 1 & 0 \\ 0 & 0 & 1 \end{bmatrix} = \begin{bmatrix} p * cos(\theta) & -C_x * sin(\theta) & 0 \\ C_y * sin(\theta) & q * cos(\theta) & 0 \\ 0 & 0 & r \end{bmatrix}$$

However, translation, another transformation, is not obtained by multiplying a matrix but by adding a vector.

$$\begin{bmatrix} x \\ y \\ z \end{bmatrix} = \begin{bmatrix} i \\ j \\ k \end{bmatrix} + \begin{bmatrix} a \\ b \\ c \end{bmatrix}$$

We can write our function f as a combination of matrix multiplication by some 3 by 3 matrix M followed by addition of a 3 by 1 translation vector.

$$\begin{bmatrix} x \\ y \\ z \end{bmatrix} = M \begin{bmatrix} i \\ j \\ k \end{bmatrix} + \begin{bmatrix} a \\ b \\ c \end{bmatrix}$$

In fact, the 4 by 4 image affine array does include exactly this information. If $m_{i,j}$ is the value in row i column j of matrix M, then the image affine matrix A is:

$$A = \begin{bmatrix} m_{1,1} & m_{1,2} & m_{1,3} & a \\ m_{2,1} & m_{2,2} & m_{2,3} & b \\ m_{3,1} & m_{3,2} & m_{3,3} & c \\ 0 & 0 & 0 & 1 \end{bmatrix}$$

Why the extra row of $[0, 0, 0, 1]$? We need this row because we have rephrased the combination of rotations / zooms / shear and translations as a transformation in homogeneous coordinates. This is a trick that allows us to put the translation part into the same matrix as the rotations / zooms / shear, so that both translations and rotations / zooms / shear can be applied by matrix multiplication. In order to make this work, we have to add an extra 1 to our input and output coordinate vectors:

$$\begin{bmatrix} x \\ y \\ z \\ 1 \end{bmatrix} = \begin{bmatrix} m_{1,1} & m_{1,2} & m_{1,3} & a \\ m_{2,1} & m_{2,2} & m_{2,3} & b \\ m_{3,1} & m_{3,2} & m_{3,3} & c \\ 0 & 0 & 0 & 1 \end{bmatrix} \begin{bmatrix} i \\ j \\ k \\ 1 \end{bmatrix}$$

Our motion correction step has only one aim, in easy words; we wish to make two images of the same thing coincide, in our terms; we wish to change the affine of one image so that, once applied, it coincided with the reference image. This will require a static image on which we will register and a moving image on which we will apply affine transformations.

Let's move on to a more tangible illustration of a motion correction that we really put into practice. For the moment, only matrix identities with a dimension of 4 can serve as affines for either of the two pictures (static or moving). In addition to this, we will make some adjustments to the affine of the moving image. The re-centering of the centers of mass is the very first transformation that we apply.

$$\begin{bmatrix} 1 & 0 & 0 & 0 \\ 0 & 1 & 0 & 0 \\ 0 & 0 & 1 & 0 \\ 0 & 0 & 0 & 1 \end{bmatrix} \Longrightarrow \begin{bmatrix} 1 & 0 & 0 & -0.158 \\ 0 & 1 & 0 & 0.039 \\ 0 & 0 & 1 & 0.008 \\ 0 & 0 & 0 & 1 \end{bmatrix}$$

The second is a metamorphosis that is very strict (translation and rotation).

$$\begin{bmatrix} 1 & 0 & 0 & -0.158 \\ 0 & 1 & 0 & 0.039 \\ 0 & 0 & 1 & 0.008 \\ 0 & 0 & 0 & 1 \end{bmatrix} \Longrightarrow \begin{bmatrix} 0.999 & 0 & 0.005 & -0.105 \\ 0 & 0.999 & 0.0013 & 0.051 \\ -0.005 & -0.0013 & 0.999 & 0.01 \\ 0 & 0 & 0 & 1 \end{bmatrix}$$

Finally, the final transformation is an affine transformation (shear and scale).

$$\begin{bmatrix} 0.999 & 0 & 0.005 & -0.105 \\ 0 & 0.999 & 0.0013 & 0.051 \\ -0.005 & -0.0013 & 0.999 & 0.01 \\ 0 & 0 & 0 & 1 \end{bmatrix} \Longrightarrow \begin{bmatrix} 0.998 & -0.006 & 0.005 & -0.108 \\ -0.002 & 0.999 & 0 & 0.051 \\ -0.004 & -0.003 & 0.998 & 0.01 \\ 0 & 0 & 0 & 1 \end{bmatrix}$$

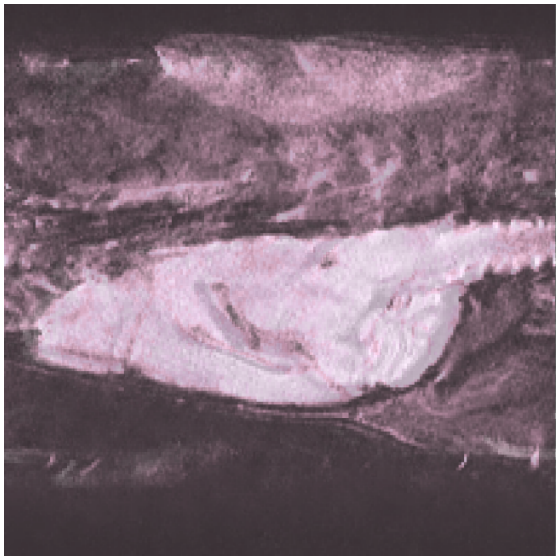

Figure 2.10: *Image to be corrected*

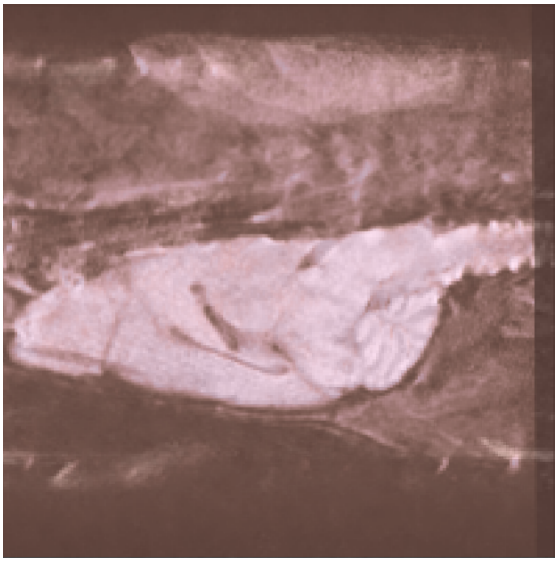

Figure 2.11: *Corrected image*

Motion Correction can be seen as a form of registration. Indeed the idea is to register two different images that represent the same thing; a rodent brain. Co-registration in this case is very effective using python libraries such as DIPY [21] or SimpleElastix[39] which are tools developed expressively for this purpose. Building on the denoising step, as demonstrated by Figures 2.10 and 2.11, our motion correction registration works quite well for our NifTi images as it succeeds in readjusting all the volumes of a shell onto the B0 frame of the shell. Motion Correction is a fundamental centerpiece in our pipeline as we use it as a base to extract the brain using a mask (see section 2.3.3) that will then be used in the microstructural algorithms such as NODDI or fingerprinting that will then allow us to analyse the brain based on maps. Therefore if the mask works well and is extracted properly, we can expect good results on that end.

However, it should be noted that there could still be inter-shell micro-movements. We could have co-registered each of the 424 acquisitions we had per mouse but the almost insignificant gain is not worth the time and computing power it would have taken.

We therefore chose to ignore them as they had very little impact on our images.

Code and parameters

```
1 def affine_reg(static, static_grid2world, moving, moving_grid2world):
```

This is the function used to co-register two images.

- `static` : The brain data of the image who don't move.
- `static_grid2world` : The brain affine of the image who don't move.
- `moving` : The brain data of the image who be register.

- `moving_grid2world` : The brain affine of the image who be register.

For one mouse, this function take on average 30 minutes and 27 seconds on a MackBook Pro (processor : dual-core Intel i7 with 3,5 GHz).

2.3.3 Brain extraction

Context

To be able to operate on the brain in the most effective manner, and to be able to interlock our code with the Elikopy pipeline, we had to eliminate all other visible substrates from the diffusion images (e.g. the skull, eyes, teeth, ...). This allows to focus entirely on the brain. To accomplish this, a mask was placed on the region surrounding the brain in order to remove the brain alone. However, obtaining this mask can be somewhat challenging because of bad acquisitions or different light intensities.

Since our diffusion MRI was performed in T2, just the brain shows up as white, while the rest of the body is black and shades of grey. Therefore, the first thing that came to mind was a machine learning algorithm that could sort all the pixels in our image according to their intensity. However, this approach is time consuming. The solution we finally opted for was to build the mask by region growing what we will refer to as a ROI.

Explanation

Because we intend to use this mask on all of the shells, we need to be certain that the calculation will not be carried out using an inaccurate acquisition.

To remedy this, the first trick we do is to create an image by summing all the shells into one in order to highlight the brain which will have a higher intensity than all the other substrates.

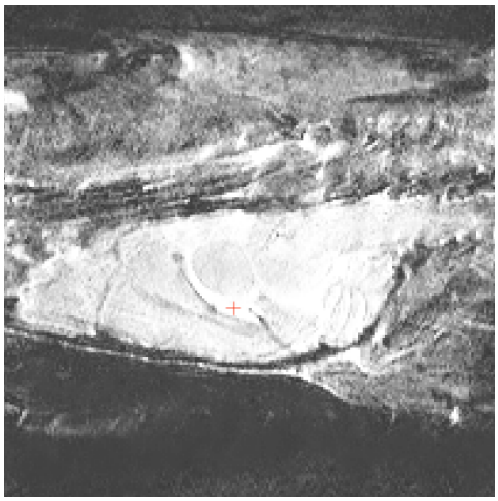

Figure 2.12: *Seed location*

The second thing we need to do is establish the place from which the mask will expand, known as its origin. We will also refer to this point as being the seed. A metaphoric way to express the beginning of the whole algorithm. In point of fact, if the origin is not situated properly, either the mask will not develop since the environment is not conducive to its growth, or it will not restrict its considerations to the brain alone. The idea is to find the pixel that sits in a luminous region. Mind you, the pixel doesn't have to be the most lit pixel because that pixel may lay in region outside the brain.

We came up with a simple yet effective algorithm in order to converge to the said point. For starters, the image is divided into 4 smaller images see 2.13. Note that if the length or

width of the image aren't even numbers, this will not influence the decision (because one is larger than the other) as the decision exclusively relies on the mean value, i.e the mean light intensity per pixel.

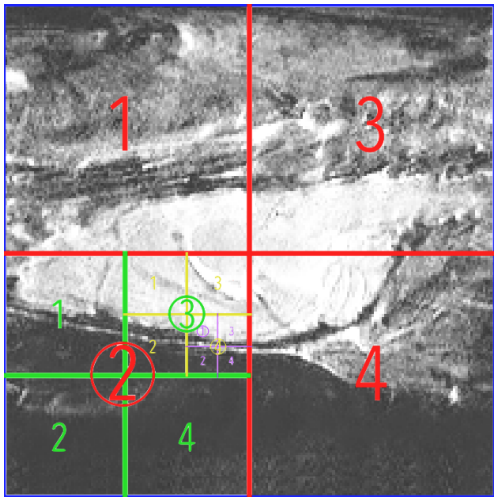

Figure 2.13: *Seed calculation*

Once the first four squares were analysed, (red squared in 2.13), we proceed in doing the exact same cuts within the winning square (2 red) thus giving rise to the green squares in 2.13. The winning square being the one presenting the highest intensity value. The algorithm proceeds on until four 1×1 squares remain i.e only four pixels remain. This algorithm mimics a binary search tree and has a complexity of $\mathcal{O}(\log_4(n))$ and is highly efficient. Finding the seed in a 200×200 pixel image only takes at most 8 operations.

The third phase is a recursive call that adds to a list all of the new pixels that are adjacent to the pixels that are already present in a ball with a fixed dimension (either 2D or 3D) and radius (r=4). The intensity of the selected pixels must be higher than the average intensity of the image plus a lambda times the standard deviation in order for them to be considered. This criterion serves as a guide for the selection process ($\lambda \in \mathbb{R}$ is a manual parameter fixed at 1 that allows the user to refine the search).

$$I(p_x) > \mu + \lambda \cdot \sigma$$

The parameter lambda can be seen as a refinement of the mask. A low lambda will allow more pixel within the mask while a high lambda will raise the standards for pixel selection and yield a lower number of selected pixels.

The algorithm follows the dynamic of a neighbourhood search each pixel will give rise to a list of neighbouring pixels that will enter a queue before being analysed. If selected the pixel yields a list of potential candidates (i.e all it's neighbours). We call neighbours the set of points that lie within a specific unit ball centered on the reference pixel we're studying. The type of ball that is used can be seen 2.16. Although the ball on Figure 2.16 is not used in the algorithm, the same code is used to generate it. The routine that generates it requires different parameters including the radius of the ball that is vital. An elegant compromise must be found in order to get a large ball in order to reduce search but small

Figure 2.14: *Filling using a function called in* `Mask_Wizard`

enough to limit the pixel candidates. Once the pixels are selected, we get the 2.14. A method of opening and closing is then used in order to smooth out any irregularities and capture a full filled mask. The opening process consists of sequential erosion and expansion of the mask to remove the excess area, while the closing process consists of sequential dilation and erosion to fill the gaps (2.15). In order to fully understand how the process of opening and closing works along with the concepts of dilation and erosion, Figures A.1 and A.2 are detailed representation of an opening or closing sequence.

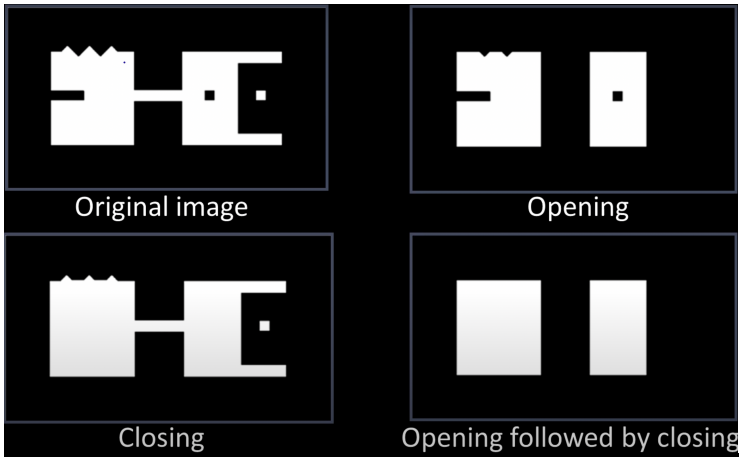

Figure 2.15: *A sequence of Opening/Closing*

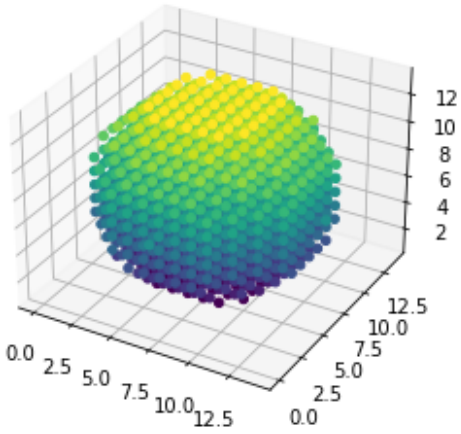

Figure 2.16: *Volume reference unit for opening an closing. Ball of radius=7*

Dilation adds any neighboring pixels that are absent from the reference layer. Moving the structuring element across each pixel of the image and checking to see if it "touches" (or, to use a more formal term, intersects) the structure of interest is what is involved in a morphological dilation. The end result is a structure that is far larger than the structure that was there before. It is possible that some of the holes will close up, and some of the particles will become joined, depending on the size of the structuring element.
Erosion is the process of removing pixels from an image based on whether or not those pixels are surrounded by other pixels on the reference layer. It is the exact opposite of dilation. It involves looking for all pixels in which the element of the structure that is centered on that pixel touches the outside of the structure. The end product is a structure that has been cut. We note the removal of particles that are less massive than the structuring element that was utilized, as well as the potential separation of larger particles. When run on 2.14, the algorithm gives the green mask in 2.17. Finally the mask is applied to the MRI and give the 2.18.

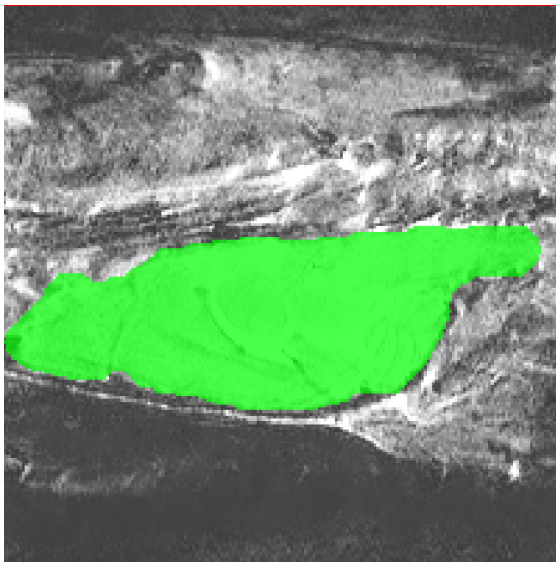

Figure 2.17: *Mask overlay on data*

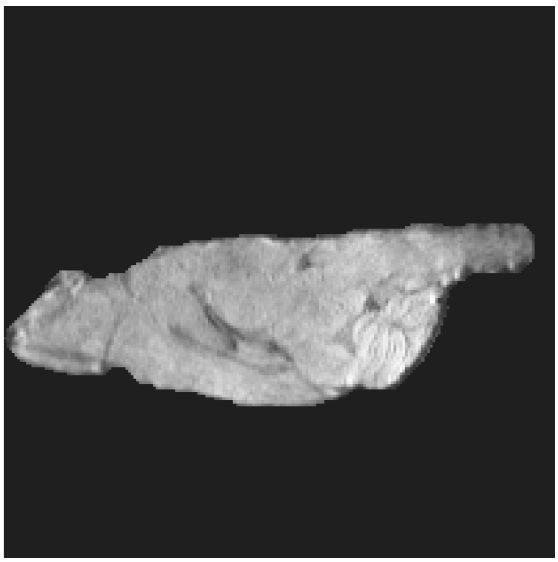

Figure 2.18: *Mask apply on data*

Code and parameters

```
def mask_Wizard(data, r_fill, r_shape, scal; geo_shape, height, work):
```

Here are the keys for using this function:

- `data` : the brain data on which you want to apply the mask.
- `r_fill` : The rayon of the circle,cylinder,or ball that we use for growing the surface.
- `r_shape` : The radius of the circle, cylinder, or ball that we use for the opening/closing.
- `scal` : The parameter λ in the formula $y = \mu + \lambda \times \sigma$ is the threshold value of light intensity that will define if we take the voxel or not. The default is 1.
- `geo_shape` : The shape of the convolution in the opening/closing. (`'ball'`, `'cylinder'`) The default is `'ball'`.
- `height` : The height of the cylinder if you choose 3D but not the ball. The default is 1.
- `work` : The dimension. (`'2D'`, `'3D'`) The default is `'2D'`.

For one mouse, this function take on average 39 seconds on a MackBook Pro (processor : dual-core Intel i7 with 3,5 GHz).

2.4 Atlas

Using now our knowledge in mouse anatomy (see Figure 1.26), we can create an atlas in order to establish the difference between addicted mice and control mice. The idea is to target a Region Of Interest (ROI) say for example the hippocampus or the Corpus callosum (CC). Once the ROI is acquired, a mask is drawn around the zone and all else is excluded. We then get a specific mask for the ROI. We can then apply this mask on processed data in order to compare mice or algorithms.

Figure 2.19: *Distinguishing the ROI on Magnetic Resonance Imaging*

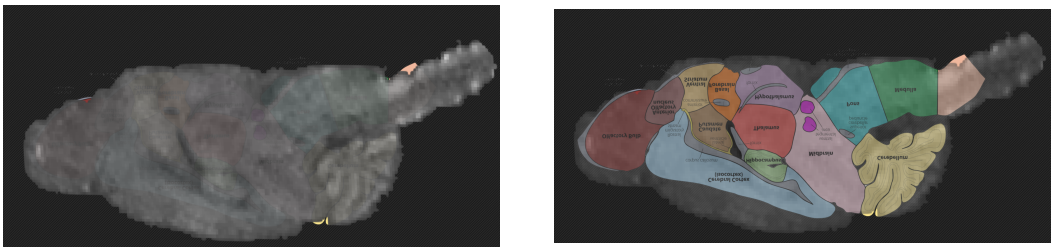

The main ROI of this study will be the CC as it is a key component in myelin loss under cuprizone. A future study may build upon this study to work on the hippocampus or the caudate putamen. But why build an atlas? Unfortunatly, co-registration between 3D MRI and 2D histology is, so far, impossible and no tool has yet been developed in order to achieve this. Therefore a registration of another kind must take place in order for us to link MRI and histology. The next section will deal with this link. Before hand, however, an Atlas must be built to locate the CC in order to create a brain-part-mask that will then be applied on microstructural maps. Again, no tool can directly detect the CC or any other brain component for that matter. The first step to the atlas will be a manual identification of the CC. Using MRIcron [52], one can outline the CC (see Figure 2.21).

Figure 2.20: *Volume 179 on acquisition 41 (Group 3, mouse 4 at time 2)*

Figure 2.21: *CC drawn on MRIcron [52] over Figure* 2.20

The first impression is quite good, the mask fits the CC and all seems well. The first idea that came to mind was to build a reference atlas on a good mouse acquisition and coregister this mouse on all others. Then apply the affine transformations to the reference mask and save it as the new mask for each mouse. This solution was tried but proved unsuccessful mainly due to the 3D coregistration tool. Our masks kept being split between two slices on the z axis thus creating two masks of different intensities. A small example in order to explain. Suppose the red plain is our reference image (see Figure 2.22). Suppose we wish to coregister the red image on the blue image in order to have their masks correspond (by making a mask for the blue image using the data on the red image and the coregsitration). Since the two images are not co planar (because of the b vectors of the shells), the coregistration will be 3D anyhow because the object is 3D. Therefore say there is a 30 deg angle between red and blue, then a third of the values of the red mask will be projected on the next blue slice while the remaining values will stick with the current blue slice depending on which slice the values are closest to. The mask thus becomes projected and unusable since the mask is binary (1 if taken 0 otherwise).

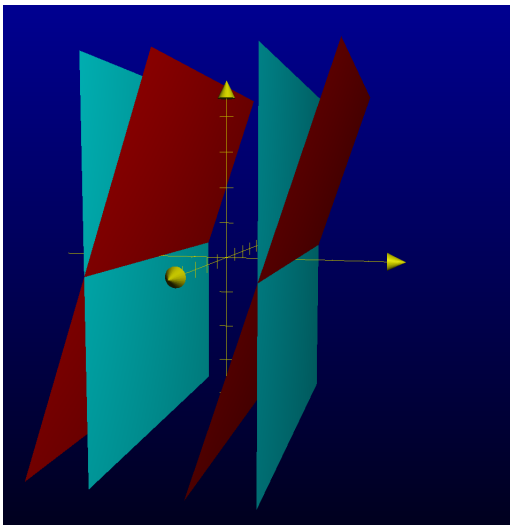

Figure 2.22: *Illustration of the coregistration of two images. The z axis is pointing out of the paper.*

It then became clear that each mask would need to be drawn independently because of this issue. This solution took time but seemed promising. However early stage analysis revealed that this mask is quite imperfect and takes pixels it should not, while forgetting pixels it should. A refinement step seemed indispensable to avoid outliers in our data set. In our 200×200 image, the CC only accounts for about 0.5%. In such cases, each pixel counts as there are only about 200 pixel values to analyse. It then came to our attention that certain microstructural maps contained information on CC; the `FA_rgb` map in particular has the advantage of depicting in 3 colors (Red, Green, Blue) the global direction of fibers within the brain (see Figure 2.23). The CC appears in the middle in red. This meant that our correction could be done using this image. The process of refinement will only concern the Red and Green arrays on which we apply our mask. The idea is to start from the empirical mask (drawn by hand) and remove any green over the mean value of non zeros in the green array. Then we add (only if it belonged to the empiric mask) all values above the mean value of non zeros for the red array. This yields the the following mask (see Figure 2.25).

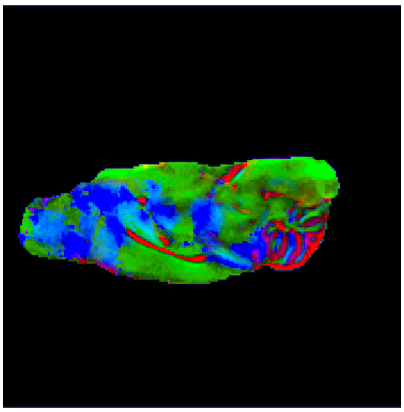

Figure 2.23: *DTI map, FA-RGB which depicts the general direction (x,y,z) of fibers with one of the three colors (or a mix)*

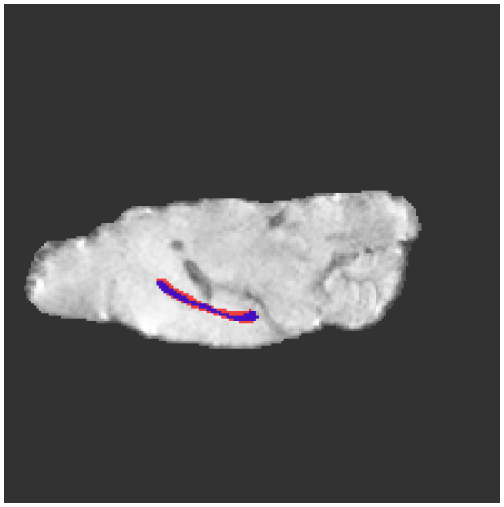

Figure 2.24: *Empirical mask (red) and refined mask (blue) on brain slice 179 of acquisition 41.*

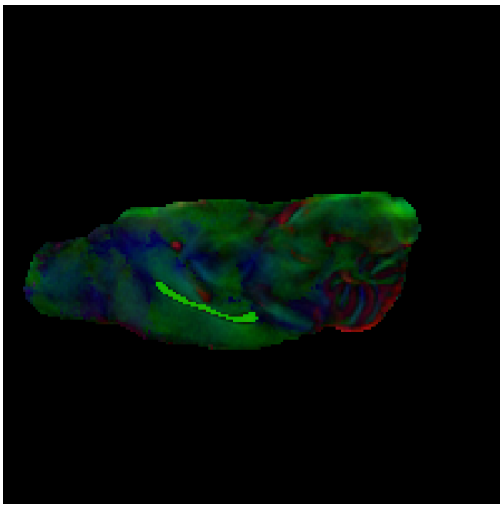

Figure 2.25: *Final CC mask on DTI's RGB map.*

Chapter 3

Analysis, comparison and discussion

Theory and practise will converge in this section in order to establish the validation with histology data. On the one hand, at our disposal sits an arsenal of Magnetic Resonance Imaging and on the other hand, extremely precise and accurate histology data. Comparing, registering and analysing these two sets of data will be the goal of this next section in hope that our microstructural tools will establish what we can see on histology data.

3.1 Histology Analysis

3.1.1 The cingulum problem

The cingulum is a C-shaped structure within the brain that wraps around the frontal lobe to the temporal lobe just above the corpus callosum (see Section 1.8). It is situated beneath the cingulate gyrus on the brain's medial surface, encompassing the entire brain. The cingulate cortex is divided into two parts: the posterior cingulate cortex and the anterior cingulate cortex. The cingulum is vital to brain structural connectivity and the integration of information it receives due to its location.

So why is it so important to us. Our study now comes together; in Section 1.7, we developed the working mechansim of Luxol Fast Blue (LFB), an important coloring tool to isolate specific biomarkers (in our case myelin). Our only option in order to analyse the histology data would be to study color intensities between mice group acquisitions (see Section 1.6.1 and 2.1). Theory predicts that within the Corpus callosum (CC) myelin will decrease after a certain time of cuprizone addiction. Therefore, we expect our LFB staining to be deeper in control mice than cuprizone mice. However, observations on histology data from cuprizoned mice have shown us that the cingulum stains are still quite blue no matter the mouse. And being a bundle of nerves (i.e. neurons and axons) this entails a strong amount of myelin. The purpose of this section will be to establish if the cingulum has the potential to influence results.

As can be seen in Figure 3.1, the cingulum is easy to spot as it is a track of fibers stretching in the same direction like small hairs. By visually comparing two histology

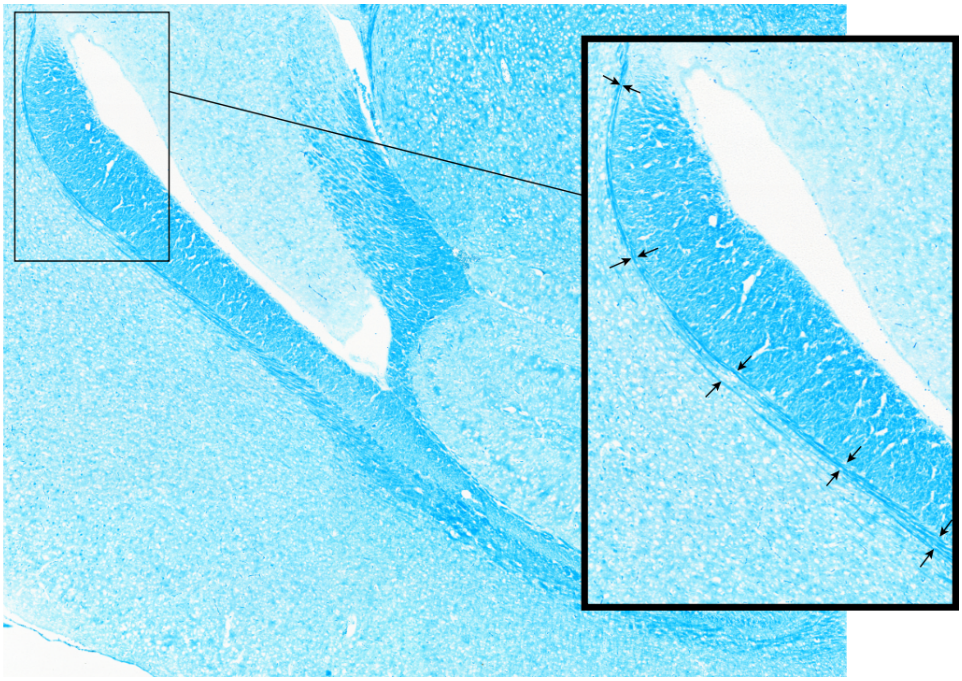

Figure 3.1: *Isolating the cingulum around the CC on a group 1 control mouse*

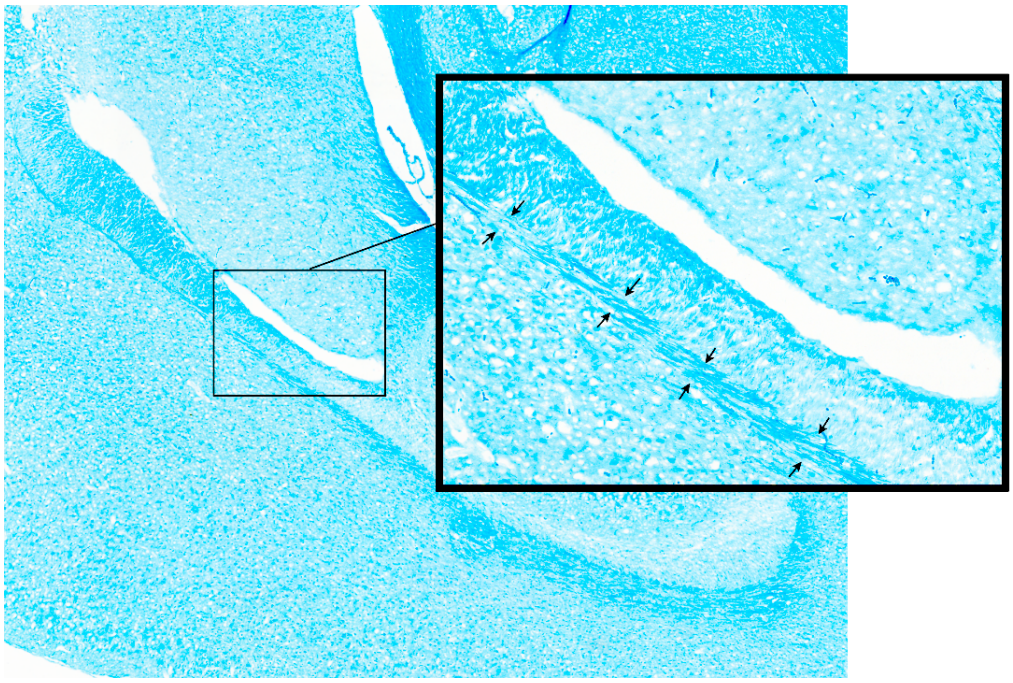

Figure 3.2: *Isolating the cingulum around the CC on a group 3 12 week Cuprizone mouse*

images (Figures 3.1 and 3.2) one could ask oneself if an intensity analysis would work. Indeed, both cingulums are clearly visible and are, at the least, of the intensity of the CC.

The analysis went as follows; taken a mouse of each groupe (see Section 2.1), we isolated the CC and cingulum on a black background in order to avoid any noise and unwanted pixels. The advantage of black in RGB coding is that the color black in encoded $[0, 0, 0]$ which makes any manipulation on the CC and easy boolean problem of "is the pixel part of CC?" (equivalent to "is the pixel not black?") $\Rightarrow$ `if pixel` $! = 0$.

Then each of the four CCs (from each mouse group) was once again isolated this time from the cingulum in order to have four other images. Then, the eight CC were all placed horizontally for our designed analysis. This analysis consisted in the averaging of vertical pixels meaning the sum of a column and then the division by the number of non zeros pixels. Then each average is placed in a table and plotted in a graph (see Figure 3.3). In order to correlate the myelin loss with the color intensity, a special rule was added to the plot, the absolute value of the average intensity minus 255 (in RGB, $[255, 255, 255]$ corresponds to white). This yields Figure 3.3.

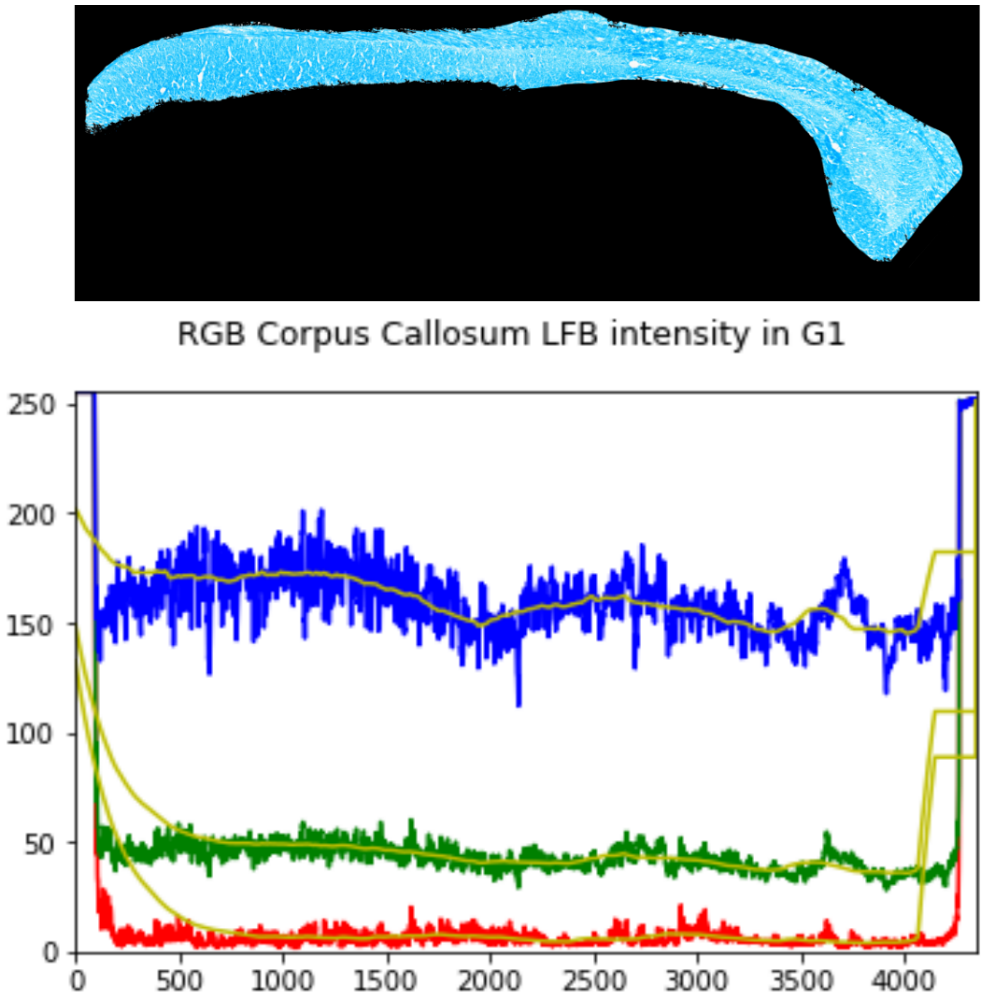

Figure 3.3: *Analysis protocol on group 1 control mouse cingulum and CC. Red, green and blue correspond with RGB respectfully. Yellow lines represents a basic approximation of the intensity function. The x axis represents the pixels from the image and the y-axis represents the absolute value of RGB intensity* -255

Because the mean intensities over rows varies greatly (i.e the sum on each column), a naive approximation of the function was implemented. A simple code that carries out the mean of the n first points. The code works as follows, let i be the pixel we wish to approximate. Let n be the neighbour parameter. We sum all intensities from i to $i+n$ (i.e. $\sum_{k=i}^{n} I_k$) and compute the average intensity $\mu = \frac{1}{n}\sum_{k=i}^{n} I_k$ on the interval $[i, i+n]$. μ is then assigned it the ith element of the array. We then move on to compare the different average function between each mouse group in order to assess if theory is respected. We expect to observe a decrease in intensity with addicted mice which would mean a myelin loss (Jelescu et al.,2015)[28] and (Torkildsen et al.,2008)[68]. Using the data with the cingulum, a quick RGB comparison between a control mouse and 6 week cuprizone mouse yields the following graph. Note that the absolute value of intensities was plotted:

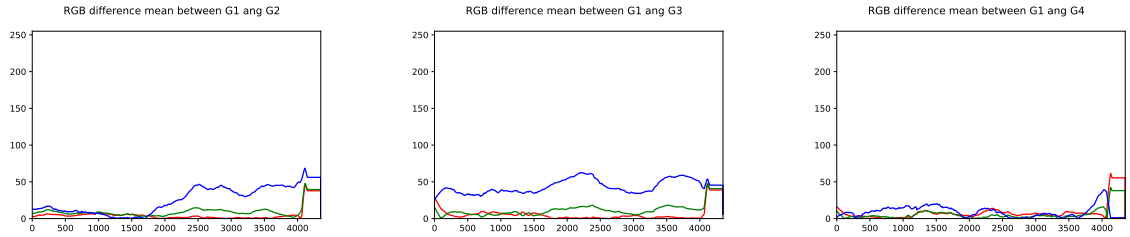

Figure 3.4: *Difference between Group 1 control and Group 2 Cuprizone 6 weeks, 3 Cuprizone 12 weeks and Group 4 remission mice intensities for RGB with cingulum.*

By comparing these graphs, it is clear that theory is respected. We can clearly see in Figure 3.4 that between the control group 1 and the 6 week Cuprizone group 2 (Figure **??**), there is a myelin loss in the lower part of the CC as predicted by (Matsushima and Morell, 2001) [41] and (Jelsecu et al.,2016)[29]. Based on the same source, a complete demyelination of the CC happens after 12 weeks (comparing group 1 with 12 week cuprizone group 3 Figure **??**). Finally, after 6 weeks of cuprizone and remission, group 4 witnesses an almost complete recovery in the CC (Figure **??**). In this respect, an analysis based on color intensity can be judged acceptable as the results follow current theory. We may now run the same study but without the cingulum. We should notice a notable change within intensities if the cingulum impacts current results. In light of the analysis with cingulum, we may however speculate that, if the cingulum is present but that the myelin loss follows theory, the cingulum does not influence our analysis. Below are the same graphics as Figure 3.4.

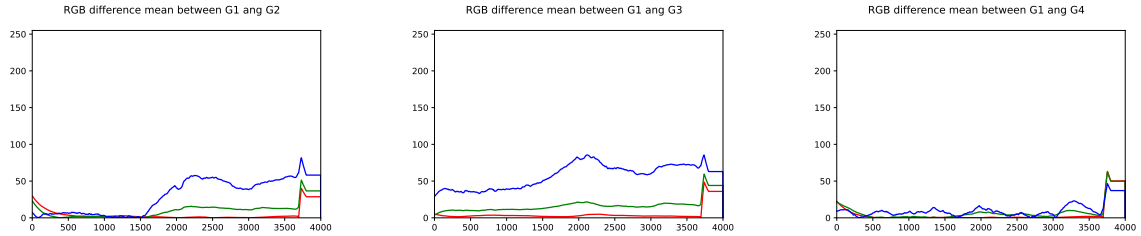

Figure 3.5: *Difference between Group 1 control and Group 2 Cuprizone 6 weeks, 3 Cuprizone 12 weeks and Group 4 remission mice intensities for RGB without cingulum.*

We can indeed notice a small change within graphics between "with cingulum" and "without cingulum". Although the intensity function seem the same, same spikes appear in some place (as in Figure **??** on the right). By comparing with Figure **??**, the right side ends with a height with cingulum whereas in Figure **??**, the right sides decreases. This may be due to cingulum however unlikely. There seems to be little variations whether the cingulum is taken into account or not. To convince ourselves, we will take the worst case scenario (the cingulum influencing a groupe 3 mouse analysis), and compare the two apporaches.

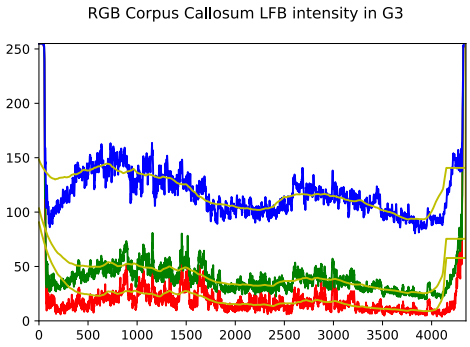

Figure 3.6: *RGB myelin intensity with cingulum*

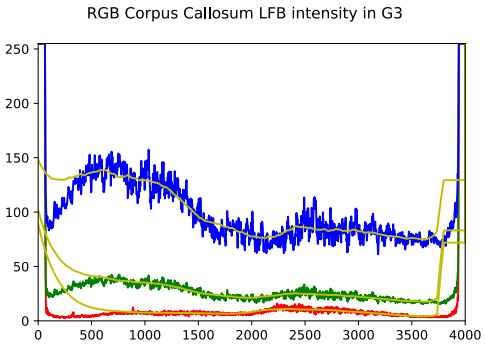

Figure 3.7: *RGB myelin intensity without cingulum*

It is now completely clear that although minor discrepencies can be spotted, the two blue functions follow the same trend. We can identify a small zone that is influenced by the cingulum between pixels 2500 and 4000. When taken with cingulum, this zone shows a slightly higher concentration of myelin whereas without the cingulum, the intensity remains relatively straight. We can also see that red and green intensity have little to no use in this analysis as the main LFB component is blue. When proceeding to a more general analysis involving all our histology data, we will choose to retract the cingulum in order to avoid small discrepancies such as seen in Figures 3.6 and 3.7. All results concerning the cingulum analysis can be found in Appendix D.1

3.1.2 Time and Diets analysis

We may now generalize with all the histology data we possess in order to show that our analysis is in accordance with theory and moreover, start on, a stolid basis when comparing with. Previously we have shown that the 4 mice from each group we selected are in accordance with theory. Our goal here is to show that these four mice are not the exception. In order to do this, we will need numerical analysis tools. Since our myelin intensity is assumed to be a signal with many spikes, a smart way of approximating the signal must be found in order to buid readable graphs. A whole section in the appendix is dedicated to this theory. We will refer to parts of it. If the reader feels uncomfortable with the notion to be presented, he may refer to Section B. Let us assume, our signal has n points. Interpolation theory has shown (see equations B.2 through B.4) that the interpolation polynomial that passes through these points exists and is unique (see also theorem B.1.3 for full proof). Therefore there is a unique polynomial of degree $n-1$ that passes through all the points $(x_i, f(x_i))$, where $f(x_i)$ is the ordinate of point x_i through the signal function of the image $f(x)$. However, high order polynomials with equally distant points are prominent to Runge phenomena on their borders. An important numerical analysis solution is the Chebyshev polynomial. However this polynomial forces the abcissa points to be specific and not equidistant. Therefore this solution is not implementable for this problem. There remains two options;

1 reduce the interpolation point set and risk loosing information while allowing a smaller degree polynomial to fit thus reducing Runge functions on the border of the domain

2 Enter the tedious realm of approximation, meaning lowering the degree of the interpolation polynomial (say m where $n >> m$ and trying to approximate the $n - m$ other points as best we can.

Solution [2] is best because it doesn't allow any loss of information. Therefore our quest is to find the minimax (see defintion B.2.2) polynomial in the sense of least squares. This induces the fact that we are working with the $2-$norm (see Section B.3). A smart solution would be working with Legendre polynomials as they are a orthogonal base which for the minimization problem ans the solving of the system comes in quite handy. First, the Legendre polynomials B.3.7 have the property of orthogonality. They also verify De La Vallé Poussin's theorem B.2.4 and the Oscillation theorem B.2.5 (both transposed in the two norm). But more than that, the Legendre polynomials satisfy the minimax orthogonality theorem for the $2-$norm B.3.6 which shows that for a minimax polynomial p_n, $f(x) - p_n(x)$ yields a polynomial that is orthogonal to every element in $\mathcal{P}_n$ (the set of all polynomials smaller or of degree n). We will therefore approximate the signal by a polynomial of degree m that will interpolate $m+1$ points and approximate the $n-m-1$ other ones.

We may now proceed in averaging, for each group, the pixel intensity in order to study it. The averaging of the color intensity for each groups is given by graph D.21 in Section D.2 dedicated to extra results on histology data. By applying the Legendre polynomial of degree 50 on the signal, the following graph can be extracted:

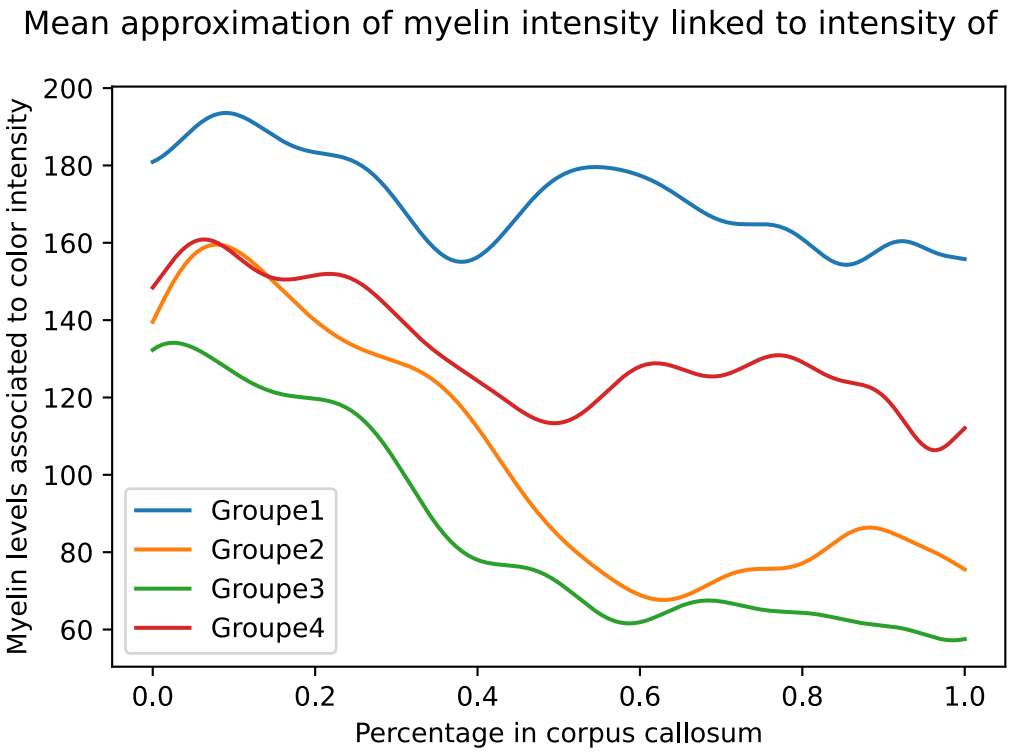

Figure 3.8: *Legendre approximation of the mean pixel intensity for each group*

The percentage of CC is not a universal measure and requires precision. In order to simply coregistration between graphs (histology and Diffusion-weighted magnetic resonance imaging), we need the same base. As it was easier to orient the corpus callosum in the histology data, the corpus callosum was placed as in Figure 3.9 to match the one in the DW-MRI. Percentage is taken from left to right as in integral would be.

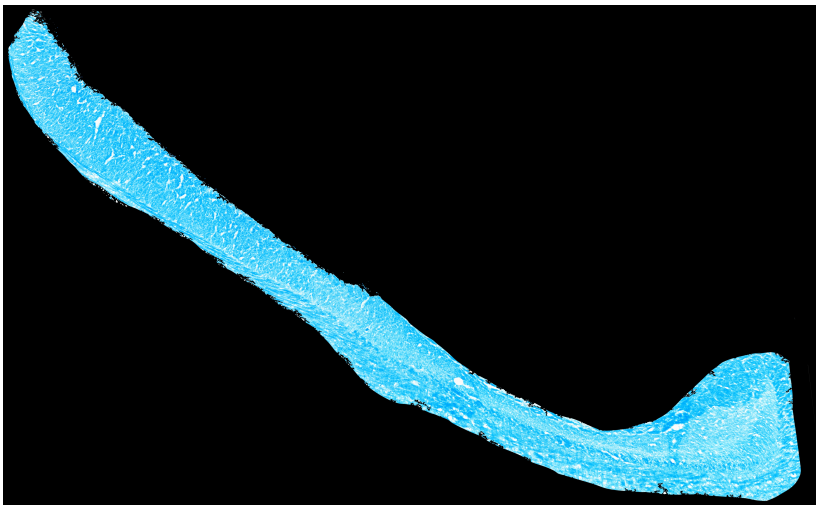

Figure 3.9: *Oriented histology corpus callosum in order to match DW-MRI orientation*

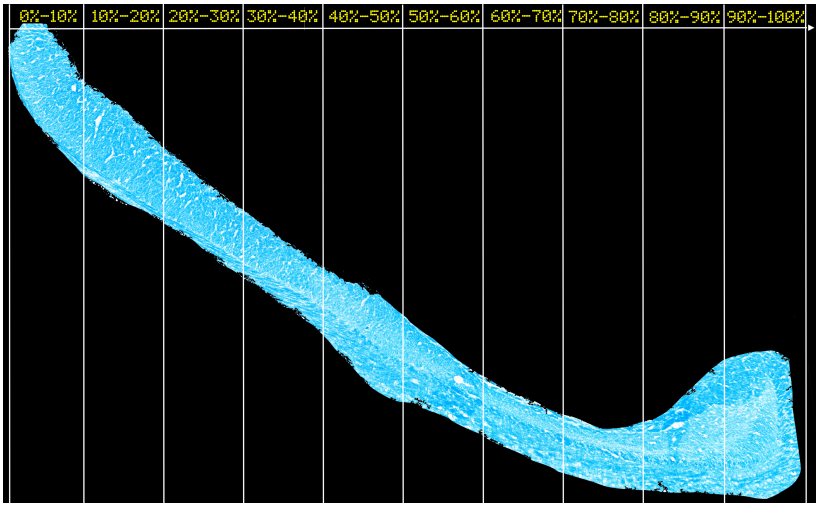

Figure 3.10: *Segmented histology data in order to visualize difference parts of the CC*

From Figure 3.8, we can go further by substituting myelin levels from one another to clearly see the impact of the myelin loss. This will enable a visual perspective of what happens in the CC. Starting with the control group (group 1) who shows the highest levels of myelin. By subtracting the group 2, 3 and 4 data to the group 1 data, one will be able to compare the groups and assess the myelin loss. This is shown in the following graph (Figure 3.11) where we can clearly see that group 2 shows prominent demyelination in the caudal part of the CC (from 0.5 to 1).

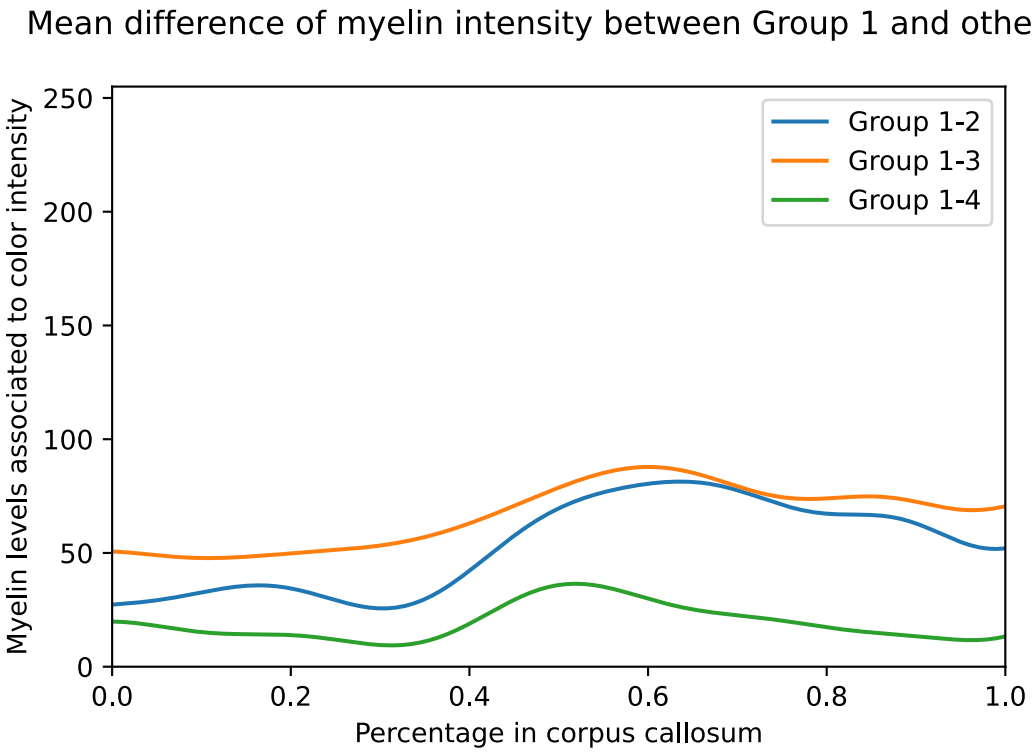

Figure 3.11: *Difference in myelin levels between group 1 and groups 2, 3 and 4 as a function of CC section*

As the myelin levels between 0 and 0.5 are below 25 in the intensity scale, this means that, although demyelination occurs throughout the CC, the demyelination is region sensitive and appears to be happening in the lower part (caudal part) of the CC. Another interesting result lied with the diffenrence between group 1 and group 4. After an addiction period, the group 4 mice have been partly demyelinated and should theoretically present demyelination levels similar to group 2.

In the histology section this will be assumed since we do not possess histology data from group 4 at that time. Once in rehabilitation and off the cuprizone diet, theory predicts that a remyelination should take place which can clearly be observed in Figure 3.11. However, after 9 weeks of rehabilitation, myelin levels haven't fully recovered from the addiction trauma. A longer test should take place in order to establish if some neuron connection are permanently deleted and full recovery impossible.

Interestingly enough, there is a single zone that seems harder to recover. Between 0.4 and 0.6 in the CC there seems to be a zone neighbouring the fornix and putamen that presents the max value of disparity in terms of myelin intensity difference. On the basis of these two analysis and by further observing the graph, one can come to the following conclusion. After the cuprizone period (it will be admitted based on the theories previously cited that groups

2, 3 and 4 have the same myelin levels) the caudal corpus callosum has been emptied by almost 80% of it's initial myelin level if we consider group 3 as being 100% of myelin loss in the caudal area of CC. This can be drawn from Figure 3.11 but also Figure D.23 and D.24 in Appendix D. As the demyelination continues for group 3, this time the rostral part is targeted as most of the myelin in the caudal part has already been eliminated. Figure D.24 shows the difference between groups 2 and 3 and how most of demyelination happens from 0 to 0.5.

We may ask ourselves why the demyelination first occurs in the caudal region rather than the rostral region of the CC? It is known for fact that, when mice are transferred to a normal diet, demyelination process is reversed due to Oligodendrocyte progenitor cells (OPC)s' spontaneous remyelination (Van der Sar et al., 2012)[70]. It is not known why administration of cuprizone only leads to a specific cell death in the OPC, but cuprizone is a copper chelator, which in turn leads to inhibition of the copper-dependent mitochondrial enzymes cytochrome oxidase and monoamine oxidase (Matsushima and Morell, 2001)[41], (Venturini, 1973)[71], (Tagge et al., 2016)[65].

Moreover the answer to the rostral-caudal difference is still not clear, elements can be found in (Lindner et al., 2008)[37] and (Steelman et al., 2012)[60] suggesting that variations in OPC concentrations may be key. The results of several different research teams have shown that the demyelination of the corpus callosum that results from cuprizone poisoning in mice varies from region to region. (Binder et al., 2008)[5], (Stidworthy et al., 2003)[62], (Wu et al., 2008)[74], (Yang et al., 2009)[76].

The degree of demyelination in these trials was expected to be more severe in the caudal parts of the callosal structure. This discovery was subsequently supported by MRI, diffusion tensor imaging analyses (Stidworthy et al., 2003)[62], (Wu et al., 2008)[74], (Xie et al., 2010)[75], (Steelman et al., 2012)[60], and observations in the current study. The research on the spatial organization of the healing processes following cuprizone-induced demyelination and the examination of the immunoregulator GAS6's impact on demyelination have both indirectly supported the rostral-caudal distinctions (Binder et al., 2008)[5].

When neural progenitor cells are injected into the lateral ventricles of cuprizone-demyelinated rats, the superficial section of the genu, the isthmus, and the splenium are repopulated and healed. However, the corpus callosum's body is not fixed (Irvine and Blakemore, 2008)[27]. Furthermore, a recent study that examined the function of CXCR4 in facilitating OPC migration discovered that its ligand, CXCL12, was more abundantly expressed in the caudal aspect of the CC compared to the most rostral aspects, suggesting that a more significant reparative process is taking place in the more caudal aspects of the corpus callosum. This was discovered during the course of an investigation from (Patel et al., 2010)[45].

3.2 DMRI analysis

To analyse the DW-MRI data, we use the same idea as for the histology analysis: isolate the CC, sum the intensity pixels by column (horizontal iteration of vertical summing) and detect a loss of intensity depending on the diets and the acquisition times. For starters, the isolation of the CC is done by identification (see Section 2.4) using a manually built atlas. Then the mask of the atlas (2.4) is refined by pixel selection using the `FArgb` map from the Diffusion tensor imaging library. In order to compare CCs between one another, a normalisation parameter must be found in order to establish a basis on which to compare them. This starts with a re-scaling of their pixel arrays (since the CCs aren't always of same size, some pixel arrays are longer or wider than others.

Standardizing them is an important step so their sizes match. This is done using the same tool described in Section 3.1 on histology data analysis. Using `polyfit`; a polynomial approximation from the `numpy` library in python, we can generate a polynomial interpolation of degree $n/2$ where n is the number of points (i.e. the number of entries in the intensity sum vector created above). This polynomial interpolation was also described in Section 3.1 on histology data analysis and can be further discussed or changed depending on the situation by using the theory in Section B. The `polyfit` function will return a, the vector of coefficients in the equation

$$p_n(x) = a_0 + a_1 x + a_2 x^2 + \ldots + a_n x^n \tag{3.1}$$

Then the result, a, is used to create all the normalized vectors using the `polyval` function from the `numpy` library in python. We generate a vector using 50 equidistant points x_i that will then be evaluated by the function. As a result our standardized vector of the CC, u^h, is therefore found as follows:

$$u_i^h = a_0 + a_1 x_i + a_2 x_i^2 + \ldots + a_n x_i^n \tag{3.2}$$

Once the approximation polynomial is constructed, we will be able to coregister the MRI curves onto the histology curves in order to assess their veracity. This procedure will be done for certain maps later on and will consist in scaling a reference curve (namely group 1 curve) and observe the differences between group 2, 3 and 4 curves to assess how the microstructre algorithm copes with myelin loss under cuprizone. Let G_1 and H_1 be group 1 for MRI and group 1 for histology respectfully and G_2, H_2 be group 2 curves for MRI and histology respectfully. Once th mean values of $G1$ and $H1$ leveled together, the error on group 2 noted E_2 will be the difference between fraction of MRI and histology. In other words:

$$E_2 = \frac{H_1}{H_2} - \frac{G_1}{G_2} \tag{3.3}$$

The following graphs are the direct result of this procedure and will begin the main course of the analysis of DW-MRI data:

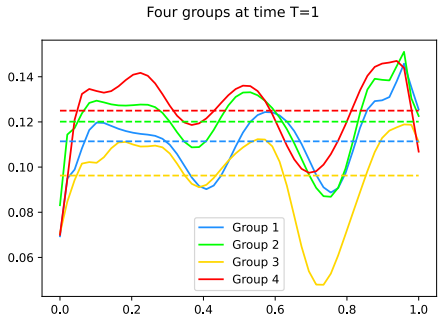

Figure 3.12: *Time $T = 1$ using DTI's* ***FA*** *map*

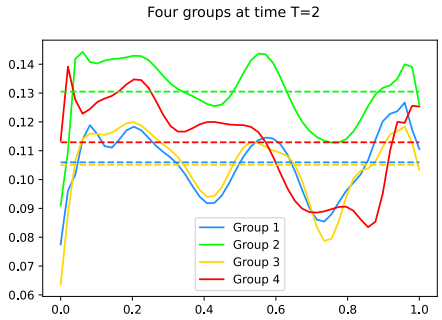

Figure 3.13: *Time $T = 2$ using DTI's* ***FA*** *map*

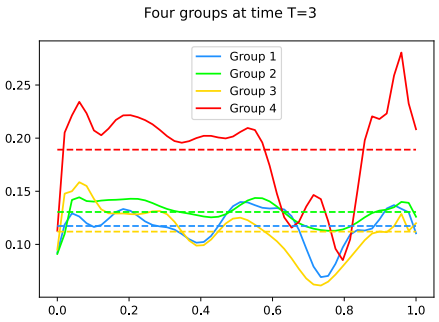

Figure 3.14: *Time $T = 3$ using DTI's* ***FA*** *map*

Figure 3.15: *Mean of anisotropie for all mouse base on FA of DTI*

It is clear from Figure 3.15 that none of the results are in accordance with theory. First, Figure 3.12 shows all four groups at the beginning of the experiment. Although each mouse is different, all myelin levels should be quite similar. However there is an important difference in FA values that ranges up to a 50% difference between group 4 and group 3. Notice how even the graphs clearly don't have the shapes but follow a trend. Figure 3.13 shows the four groups at time $T = 2$. At this time, three groups are under a strict cuprizone diet while group 1 remains the control group. And although we would expect to find out that group 1 has higher myelin levels, the results show that most groups are higher than 1 and don't make much sense. For example, group 3 maintains itself around group 1 while group 2 suddenly rockets past group 4 to achieve the highest myelin levels (even higher than the previous time period). This would mean cuprizone facilitates the creation of myelin within the CC which is absolute nonsense as previously cited studies have shown the exact opposite. We may hypothesize that the construction of the graphs are not relevant for the current data as each mouse is different and only relative to it's own group. We could therefore construct for each group a graph showing the group's evolution during the different time periods.

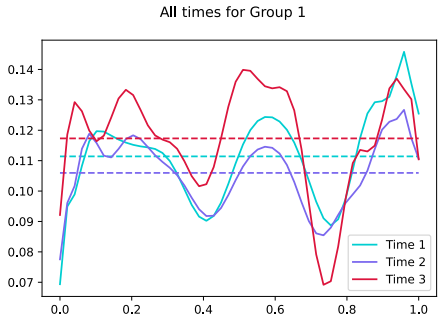

Figure 3.16: *Group 1 using DTI's* **FA** *map*

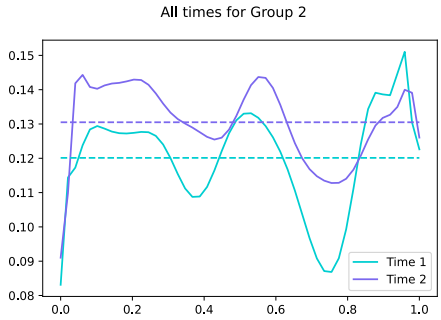

Figure 3.17: *Group 2 using DTI's* **FA** *map*

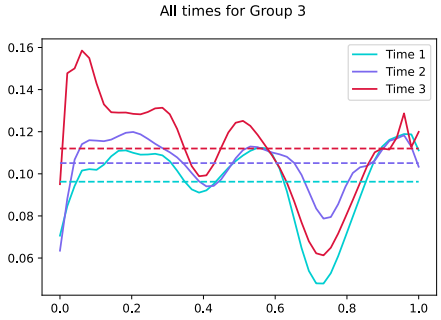

Figure 3.18: *Group 3 using DTI's* **FA** *map*

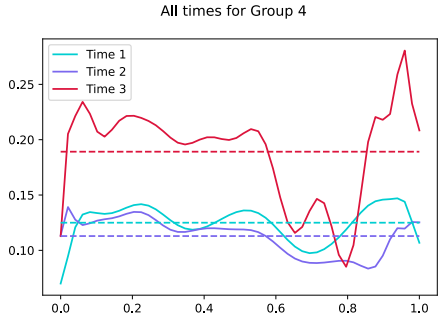

Figure 3.19: *Group 4 using DTI's* **FA** *map*

Figure 3.20: *Mean of anisotropie for all mouse base on FA of DTI*

Once again, we can clearly observe that these graphs are absolutely not what is predicted from theory and are far from our expectations. It is clear that for group 1 mice (Figure 3.16), the mean values (represented by the dashes) should be huddled together as no treatment was given to these mice hence no modification of myelin intensity should be observed whatsoever. On groups 2 and 3 (Figure 3.17 and 3.18), the Time $T = 2$ curves should be far below the Time $T = 1$ curves as the myelin intensities are affected by cuprizone; theory proved by the histology data in our possession (see Section 3.1). On the group 4 graph (Figure 3.19) the Time 3 curve shouldn't overshoot the Time $T = 1$ graph. If this was reality, it would mean that taking drugs made more neuron connections in the CC. Taking a more precise look, mouse by mouse, problems can easily be identified. For example, mouse 5 (Figure 3.22) presents results only admissible for a group 3 (cuprizone 12 weeks) while mouse 1 (Figure 3.21), from the same group, presents results that adhere to theory. Another example is mouse 11 (Figure 3.25) should see it's FA at time $T = 2$ reduced by administration of cuprizone as mouse 12 shows (Figure 3.24). However, by some magical artifact, mouse 11 has even more myelin after 6 weeks of cuprizone than when it started.

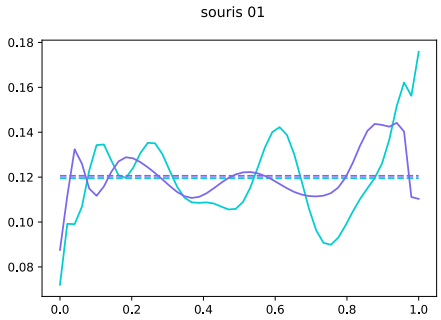

Figure 3.21: *Mouse 1 using DTI's* **FA** *map*

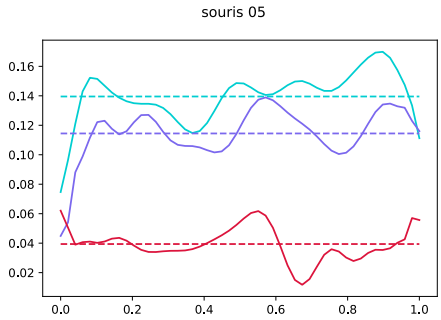

Figure 3.22: *Mouse 5 using DTI's* **FA** *map*

Figure 3.23: *Group 1 : control*

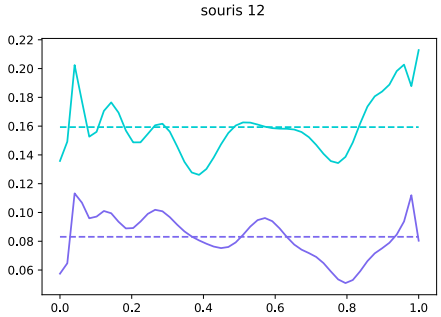

Figure 3.24: *Mouse 12 using DTI's* **FA** *map*

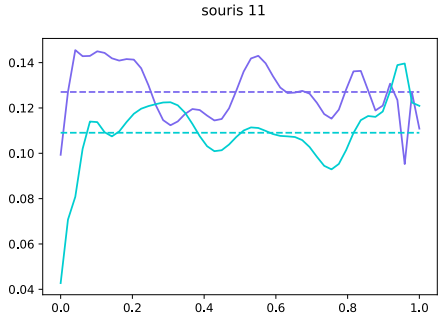

Figure 3.25: *Mouse 11 using DTI's* **FA** *map*

Figure 3.26: *Group 2 : 6 week of cuprizone*

To understand why the results are various and uncoordinated, the sole solution was to reopen the raw NifTi files to actually assess their admissibility. It is useful to add here that before this point, we had not carried out any quality check of the data, relying only on the lab's work. The first conclusion were quite appalling; many acquisitions presented known artifacts that rendered the image literally unusable (see Section on Artifacts). Here are a few artifacts found in mouse 5 and 11 data:

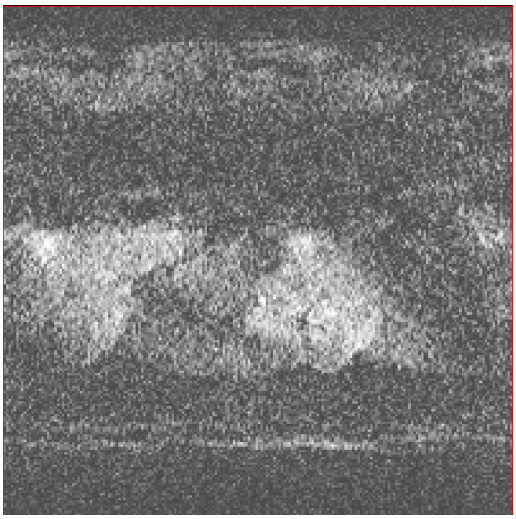

Figure 3.27: *Volume 197 (mouse 5 Time $T = 1$)*

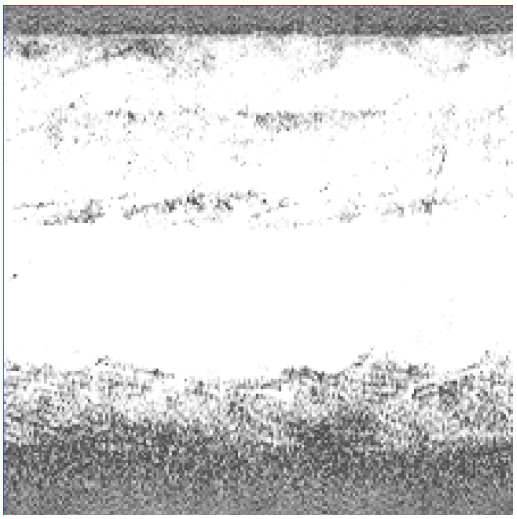

Figure 3.28: *Volume 282 (mouse 5 Time $T = 1$)*

Figure 3.29: *Artifacts on mouse 5*

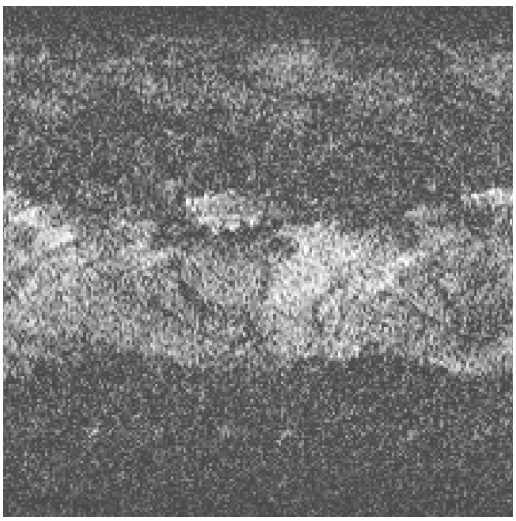

Figure 3.30: *Volume 188 (mouse 11 Time $T = 1$)*

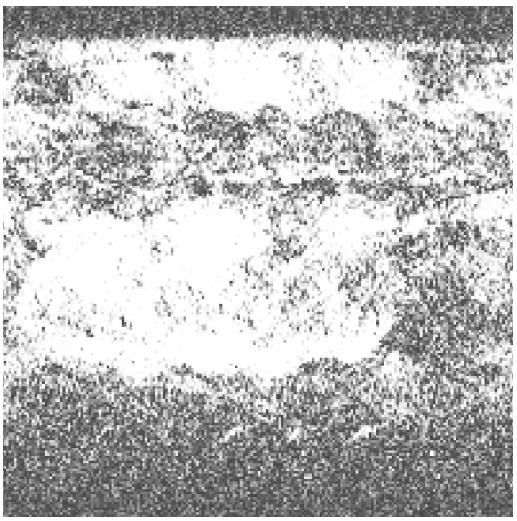

Figure 3.31: *Volume 278 (mouse 11 Time $T = 1$)*

Figure 3.32: *Artifacts on mouse 11*

A manual cleaning of all acquisition was mandatory; liquidate all acquisitions presenting too many artifacts rendering the image too poor for analysis of making it an outlier had become the new goal. This allowed building a study on a more solid basis. More on this can be found in Section 1.5. However, suppressing acquisitions comes with a cost: the number of acquisitions having decreased beyond expectations, our data set lacked certain

categories (some categories had only one acceptable acquisition, some had none like Time $T = 3$ where we only had 3 acquisition per group to start with). This gave rise to the first conclusions on this study.

3.2.1 First conclusions

Keep in mind that, although we will continue our analysis by pixel column mean, it cannot be considered as a statistical study in light of the missing data. Moreover we discovered that a time analysis (meaning a graph on which each group is plotted at time $T = \tau$) made no sense since every group consists of different mice with different intrinsic physical and physiological attributes that are too various for this study. To fully understand the underlying concept we are trying to discuss, Figures 3.33,3.34 and 3.35 show an example on `FA` maps:

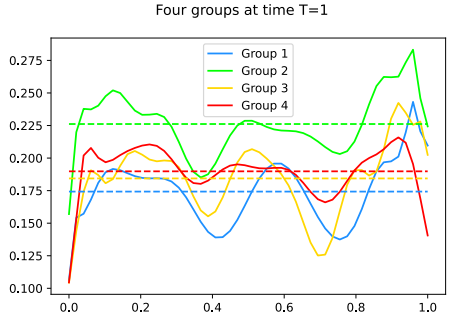

Figure 3.33: *DTI's FA map for T=1*

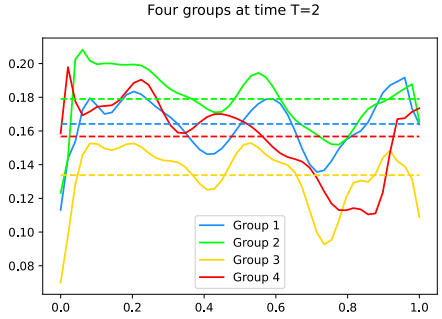

Figure 3.34: *DTI's FA map for T=2*

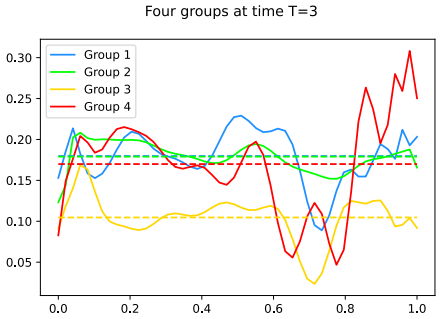

Figure 3.35: *DTI's FA map for T=3*

Figure 3.36: *Mean of anisotropy for all mice based on DTI's FA map*

On Figure 3.33, where the time $T = 1$ is shown, all the curves should be merged together. It is clear there are incoherences. What could possibly justify that group 2 should present such high levels of myelin before even anything was administered? There are multiple answers (Acquisition quality, physiology, inaccurate processing...). We can also clearly see major discrepancies on Figure 3.34 on time $T = 2$ where group 2 is still higher than group

1 even after 6 weeks of cuprizone. Group 4 has the same levels of myelin than group 1 even though group 4 has also been under influence for the past 6 weeks. Finally Figure 3.35 represents the exact same thing as Figure 3.8 in Section 3.1. However the result vary too much. Group 1 doesn't dominate in terms of myelin concentrations and levels with group 2 (Group 2 doesn't have a time $T = 3$, the green curve is group 2 at time $T = 2$) and group 4. Group 4 even rises higher than group 1. The only coherent result we can pull are that group 3 is below.

Excluding the study over time and only taking the study over groups was the natural conclusion to make in light of the previous argument (avoid at best variations due to physiological attributes inherent to each mouse). To quantify the error (as defined in equation 3.3), we will need a base considered to be the truth; namely histology. The Histology data is in accordance with theory as we have shown in Section 3.1. Therefore we will make the following assumption. For group 1 mice, the histology data acquired at time $T = 3$ also represents times $T = 1$ ane $T = 2$ and will serve as a reference for all mice at time $T = 1$. The histology data for group 2 (retrieved at time $T = 2$) will serve as a model for groups 3 and 4 at time $t = 2$. Thus we will be able to compare DW-MRI images to the histology data group-wise.

3.2.2 DTI

Concerning DTI specifically, among the few maps exported by the algorithm, the following maps were chosen for analysis: Fractional anisotropy (FA) map, the Axial Diffusivity (AD) map and the Radial Diffusivity (RD) map. Recall from Section 1.2.3 that the DTI model is what we could see as a binary model (it considers isotropic or anisotropic diffusion with the help of a diffusion tensor). Using the diffusion tensor, a number of metrics may be used to reflect the current condition of the brain's microstructure. The mean diffusivity (MD) is calculated by taking the average of the eigenvalues of the diffusion tensor.

$$MD = \frac{\lambda_1 + \lambda_2 + \lambda_3}{3} \tag{3.4}$$

This number indicates the degree to which the movement of water molecules inside a particular voxel is inhibited. It is possible to get anisotropy indices by computing the Axial Diffusivity

$$AD = \lambda_1 \tag{3.5}$$

and the Radial Diffusivity

$$RD = \frac{\lambda_2 + \lambda_3}{2} \tag{3.6}$$

and comparing the results of these computations. They both represent the mean diffusivity in their respective directions, which are axial and radial. However, the FA meter is by far the most often used DTI metric. The FA values range from 0 to 1, with 0 indicating that all of the eigenvalues are equal $\lambda_1 = \lambda_2 = \lambda_3$ and that the diffusion is isotropic (for example,

in the Cerebrospinal fluid (CSF), and 1 indicating that one direction λ_1 is largely dominant for the diffusivity and that the diffusion is strongly anisotropic.

$$\text{FA} = \sqrt{\frac{3 * [(\lambda_1 - MD)^2 + (\lambda_2 - MD)^2 + (\lambda_3 - MD)^2]}{2 * (\lambda_1^2 + \lambda_2^2 + \lambda_3^2)}} \tag{3.7}$$

Axial Diffusivity (AD)

As stated previously, the AD value is the ratio of axons in the principal direction. Physically speaking, we are expecting a drop in AD values since cuprizone should eliminate axons and thus reduce the axon clutter in the principal direction.

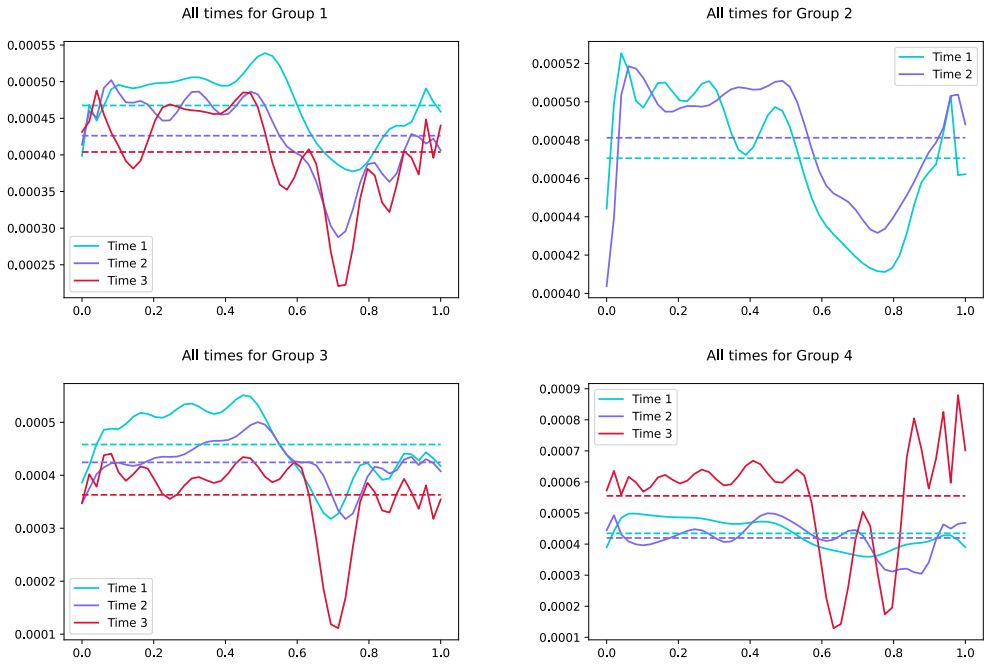

Figure 3.37: *Mean of axial diffusivity for selected mice based on DTI's AD map*

It is quite hard to spot differences in the AD map. Most of the groups don't seem to have the right profile; group 3 follows group 1's trend while group 2 and 4 are oddities and don't seem to follow any trend at all among themselves. Moreover, the values are ridiculously small which makes any analysis worthless.

Radial Diffusivity

Radial Diffusivity is linked to AD as the complementary. While one (AD) measure the fraction in the main direction, the other (RD) measure the fraction in the two other directions. We therefore expect this ratio to rise with the administration of cuprizone.

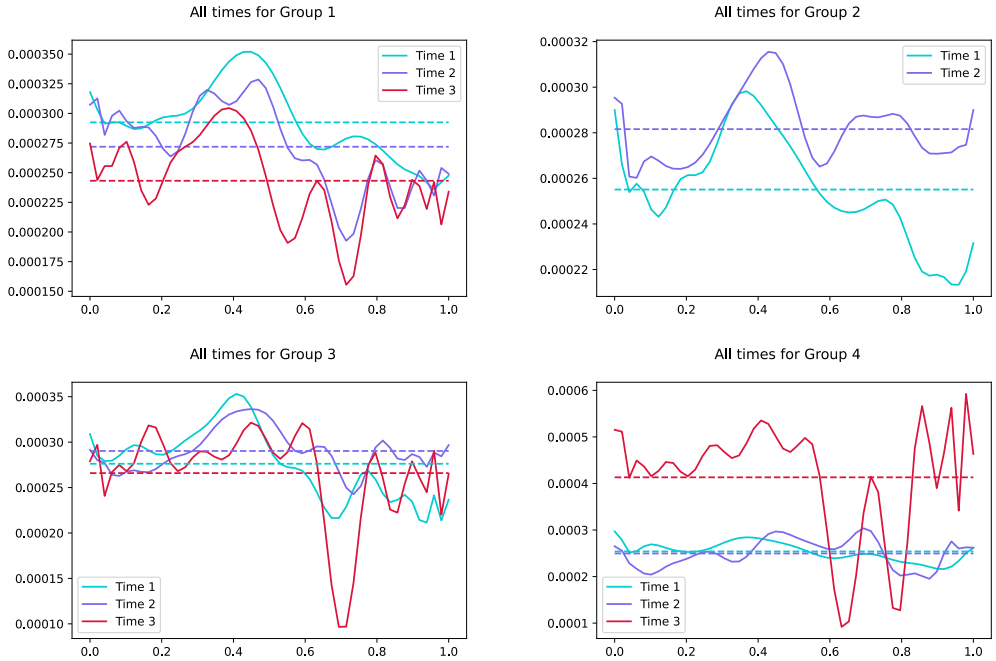

Figure 3.38: *Mean of radial diffusivity for selected mice based on DTI's RD map*

Once again, the graphs are ambiguous and unclear. The values are small and no important conclusions may be drawn from this graph.

Mean Diffusivity

The Mean Diffusivity map is not of use, we aren't expecting any results because the loss expected in the main direction (AD) would be compensated by some gain in the other directions (RD). Moreover, since the AD and RD haven't yielded any results there is no need for graphs as $MD = \frac{AD}{3} + \frac{2RD}{3}$

Fractional anisotropy

The CC being densely constituted of neurons, the Fractional anisotropy should theoretically be high. Since the neuronal grid spans in the same direction connecting neurons together, this conglomerated wad of fibers should be detected by the microstructural algorithm which will then give rise to high FA values in that area. Moreover, under the influence of cuprizone, according to theory and histology data, the axonal density should decrease which would in turn be detected by microstructural algorithm leading to a drop in FA value. The following graphs show, for each group, the mean FA value for each acquisition time.

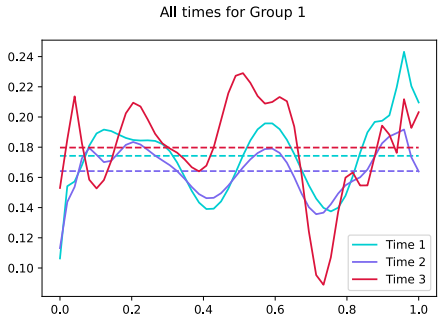

Figure 3.39

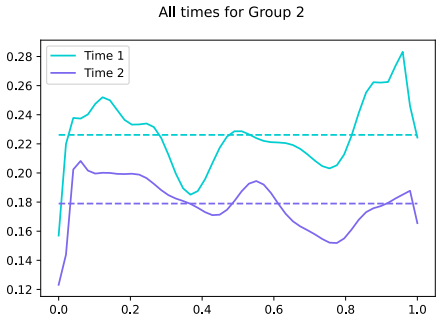

Figure 3.40

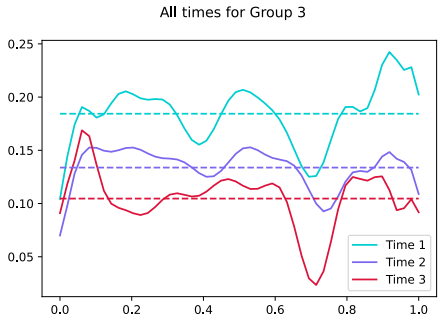

Figure 3.41

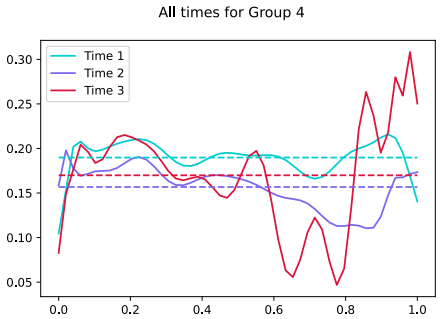

Figure 3.42

Figure 3.43: *Mean of anisotropy for selected mice based on DTI's FA map*

Figure 3.39 shows the mean values of FA values at each acquisition time. According to theory, these three times should be equivalent. Although the curves diverge quite a bit, the mean value (represented by the dashed lines) are quite similar for each acquisition time. They follow more or less theory. However, time $T = 3$ clearly does not follow the same trend and dives below the other curves around 0.8. This is the result of elimination of different acquisitions due to the presence of too many artifacts (as described in Section 3.2.1). Having only a single data to exploit, there is no more "mean" value for time $T = 3$ but only one acquisition acting as the mean value. This is the reason for the dive and the difference in trend.

Figures 3.40 and 3.41 are precisely what we were expecting to see. At each time there is a loss in FA value which in turn means a loss in myelin. Moreover, time $T = 1$ and time $T = 2$ should result in the same loss for both group 2 and 3. By geometrically comparing on the graphs, there is a 25% decrease in FA value between time $T = 1$ and time $T = 2$. In Figure 3.41 the same percentage can be geometrically calculated and we reach a 28% difference in FA value.

Figure 3.42 also follows theory at first glance and can also be compared the previous two during times $T = 1$ and $T = 2$. An FA value decrease of about 20%. We can conclude that the FA value follows theory in this respect. A last word on time $T = 3$, although we

can clearly see recovery (as the curve is higher than the time $T = 2$ curve), the gap between curves ($T = 2$ and $T = 3$) isn't significant enough to draw any conclusions as the length of the gap is similar to the gaps between curves in Figure 3.39 for group 1 as their values seem to orbit around 7%.

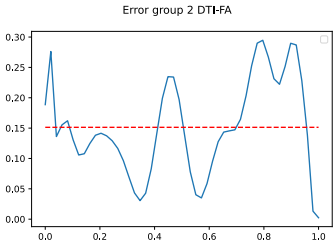

Figure 3.44:

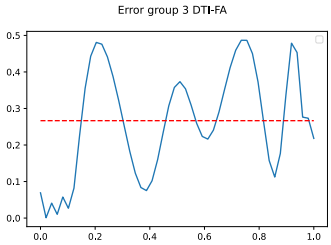

Figure 3.45:

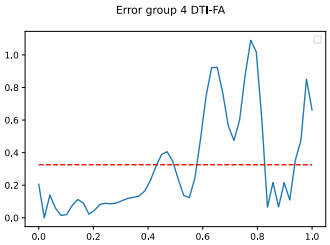

Figure 3.46:

Figure 3.47: *Error of DTI's FA map for selected mice*

An interesting question to ask one self is how to quantify the error 3.3. Let us rephrase what we have said earlier. First, one must start from theory (i.e histology) and then add practise to it. By normalizing $T = 1$ curve for group 2 on `FA` (i.e by making a correspondence between this curve and the histology group 1 curve which corresponds to time $T = 1 = 2 = 3$ for non cuprizoned mice), we have created the basis for analysis . Then by comparing the difference in FA between groups for FA and histology we get error 3.3 for each groups. To sum up, by taking a reference point (here group 1 is assumed to be the reference), then by subtracting the FA values to the histology values (that are now on the same scale as the FA values due to normalization), we can plot the error in prediction for `DTI`'s FA map. We have a mean error of 30% for groups 3 and 4. This means that, considering histology as being the absolute truth, the MRI data shows up to $\pm 30\%$ of the histology data value; i.e there can be up to 30% less or 30% more of myelin loss and gain.

3.2.3 NODDI

Recall that NODDI distinguishes itself from DTI as NODDI is a microstructural algorithm that uses an active dictionary to map the brain's connections. There are three categories; intra-cellular, extra-cellular and CSF. Among the many maps NODDI outputs, some were selected for our study; intra-cellular fraction (`F_intra`), extra-cellular fraction (`F_extra`) and isotropic fraction (`F_iso`). There is an additional map we will not use but will discuss; the Intracellular volume fraction (`ICVF`).

`F_intra`

The intra-cellular fraction is the ratio of constrained matter within the sticks as shown in Figure 1.19. It is the ratio that we are interested in as axon act as sticks in which water

molecules are trapped and can only diffuse in one direction. We expect it's value to decrease with the administration of cuprizone as it has been previously established that cuprizone reduces the density of axons.

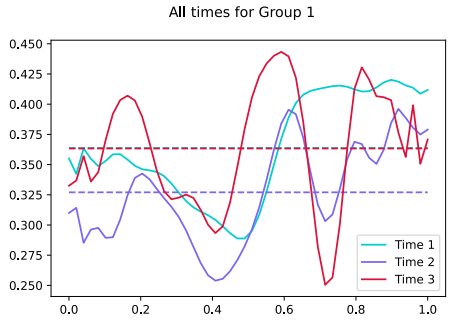

Figure 3.48:

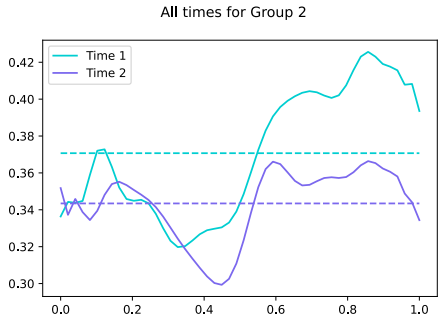

Figure 3.49:

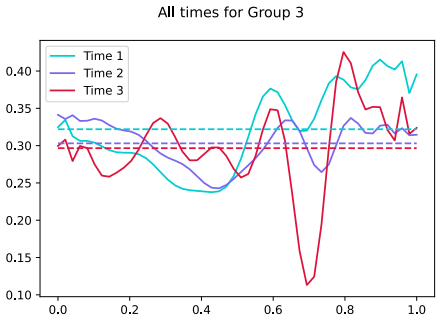

Figure 3.50:

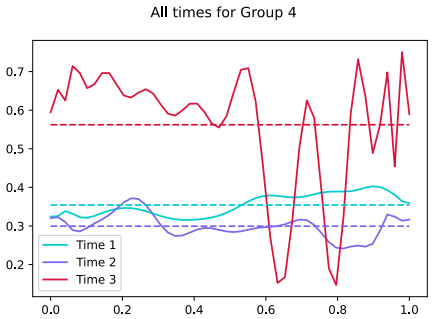

Figure 3.51:

Figure 3.52: *Mean of intra-cellular fraction for selected mice based on NODDI's* `F_intra` *map*

At first glance, the graphs seem to follow the correct trend meaning they behave has expected. However, the time $T = 2$ for group 1 (Figure 3.48) shows and important gap with the two other times. There are two options; the first would be to consider time $T = 2$ as being an actual value to take into account. It will naturally lead to the dismissing of this map since Figure 3.49 and Figure 3.50 present a gap difference between curves that isn't significant in regards to the gap in times from Figure 3.48. Because of this result, and although the `F_intra` map is promising, we would dismiss this result as NODDI failed to produce evidence of myelin loss in it's maps. The second option, that would seem more reasonable, is to consider time $T = 2$ as an outlier, dismissing just this value would make things more interesting as we could consider the trends in Figures 3.49, 3.50 and 3.51. Group 2 behaves like theory and presents even similarities in terms of region demyelination. As shown in Section 3.1, there is a caudal demyelination before a rostral demyelination. This phenomenon can be observed in Figure 3.49 where the curves start rather together (from 0 to 0.4) and then a great gap is created suggesting an important demyelination in

that area (from 0.5 to 1). Group 3 isn't as conclusive as the gap between times $T = 2$ and $T = 3$ are negligible. As for group 4, we will consider time $T = 3$ as an outlier as it's very high value finds no justification whatsoever in the other graphs.

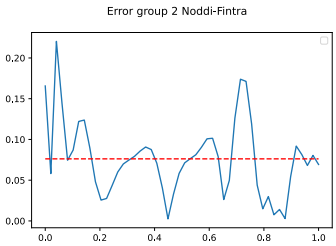

Figure 3.53:

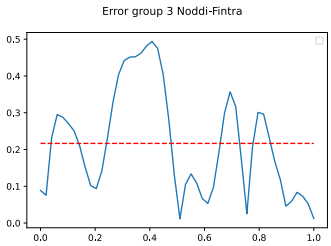

Figure 3.54:

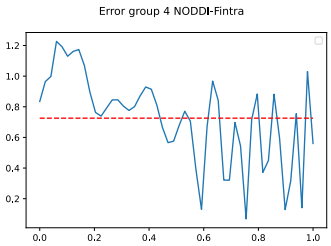

Figure 3.55:

Figure 3.56: *Error of NODDI's* ***F_intra*** *map*

It is evident that Group 2 has a very small error as the group 2 is representative of theory as described in Section 3.1. Group 3 has a higher error as the gap between times in Figure 3.50 isn't standard for these graphs. Because of the group 4 outlier (time $T = 3$) the result on the error is very high. Removing this outlier would probably be the best solution, however the fact that we only have one group 4 time $T = 3$ mouse wiould mean we wouldn't have any mice to compare in this category. That is why we will keep this mouse and the resulting outlier. The fact that we have two outliers in the `F_intra` map can be due to multiple artifacts in different acquisitions.

`F_extra`

As explained in Section 1.3.1, the extracellular compartment is the region around neurites that is populated by several types of glial cells as well as cell bodies in gray matter (soma). We would expect it to be low at first and then to increase with the administration of cuprizone. Once again, we can spot outliers like group 1 time $T = 3$ in Figure 3.57 (this curve has litterally no physical signification as all group 1 times should be leveled as stated by thoery) and group 4 time $T = 3$ (Figure 3.60). Group 2 (Figure 3.58) follows theory as the fraction increases while axons dissapear. Group 3 doesn't amount to much. There however seems to be a correlation between groups 1 and 3.

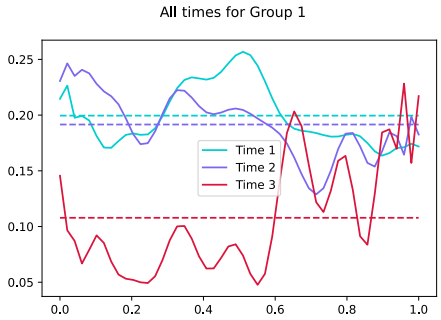

Figure 3.57:

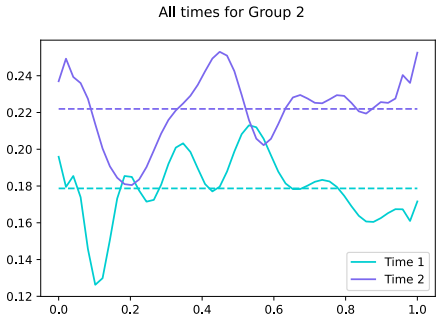

Figure 3.58:

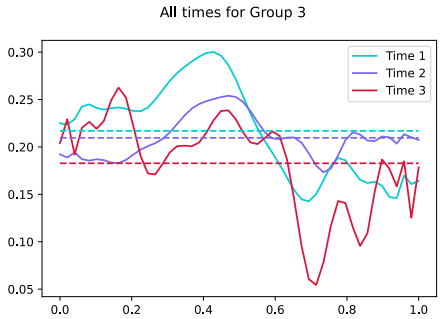

Figure 3.59:

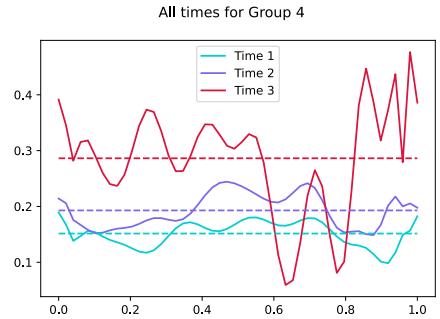

Figure 3.60:

Figure 3.61: *Mean of extra-cellular fraction for selected mice based on NODDI's* ***F_extra*** *map*

When axons disappear, they leave a void that will be replaced by either extra-cellular volume or Cerebrospinal fluid volume. NODDI will decide by which to replace it. Therefore this fact can account for the mitigated results we've encountered for this map. There are no error graphs here as we cannot quantify the difference between the rising `F_extra` value and our histology myelin intensities.

`F_iso`

The isotropic fraction (`F_iso` map) is the ratio of CSF in the voxel. We expect this ratio to be very low in the CC then slightly rise when cuprizone is administered. Following the previous map, we cannot tell if NODDI will replace the missing axons in voxels by CSF or extra-cellular volume. The values are too low to be analysed. Since we're in the CC,it doesn't make much sense for the value of CSF to rise. There is clearly not much to be said from this map and no conclusions can be drawn.

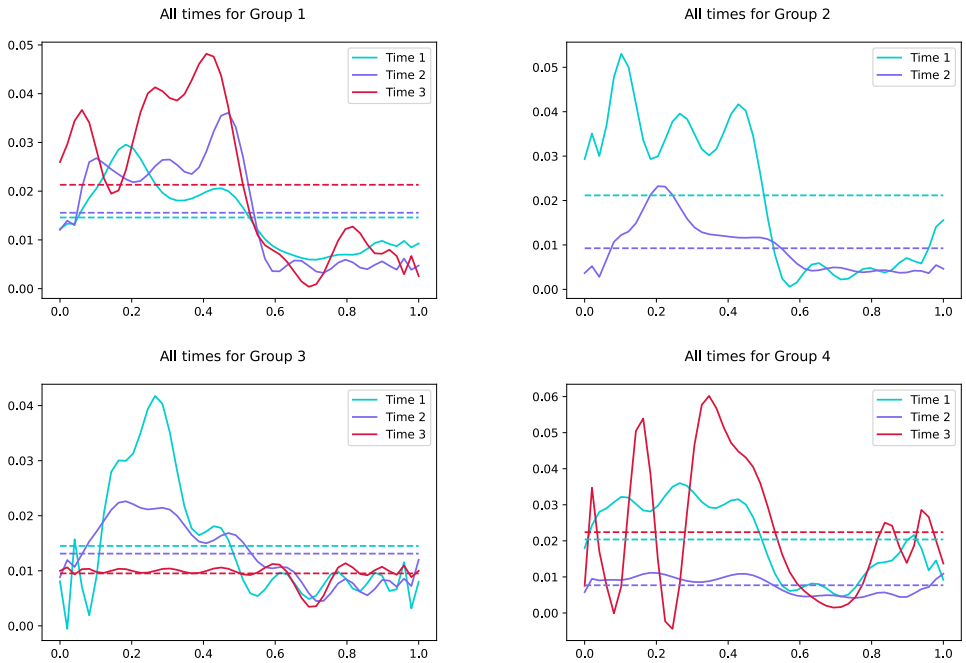

Figure 3.62: *Mean of isotropic fraction for selected mice based on NODDI's Fiso map*

`ICVF`

Intracellular volume fraction (ICVF) expressed as a fraction of the non-CSF compartment and the orientation dispersion index (ODI), which is calculated from the concentration parameter of the Watson distribution in such a way as to give a figure ranging from 0 (no dispersion of neurites) to 1 (fully dispersed neurites). The method enables their differing effects to be disentangled. This map is often used in studies on epilepsy however, in this case, this value is not of use as it doesn't represent much since the intracellular loss is compensated by something else. Nevertheless, we would expect a decrease because it is the ratio of `F_intra` over `F_intra`+`F_extra`. Since we did no see a gain in CSF volume (cf `F_iso` map), we could expect a decrease in `ICVF` value.

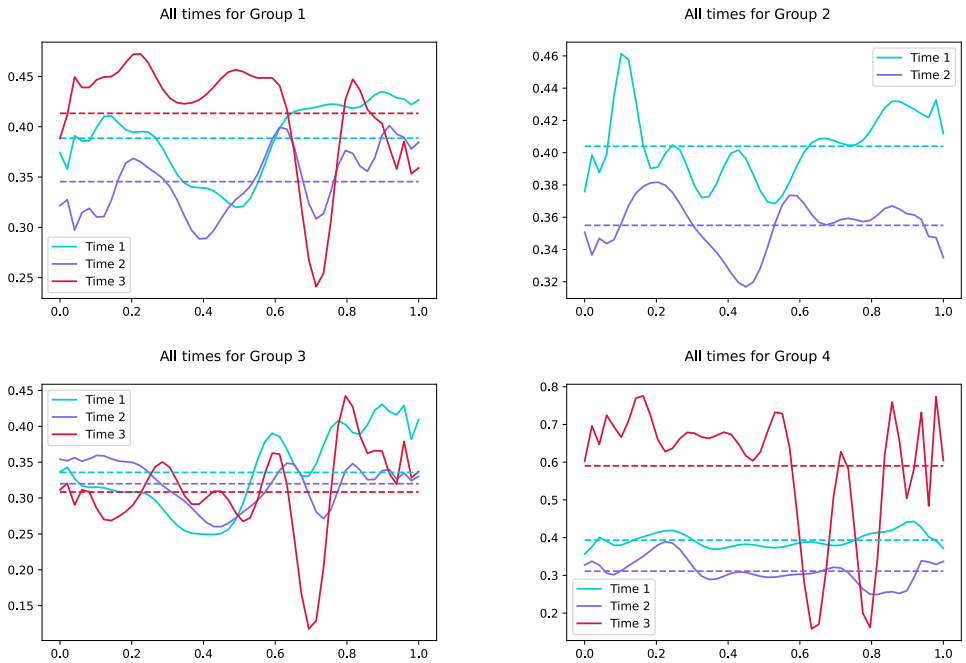

Figure 3.63: *Mean of intra-cellular volume fraction for selected mice based on NODDI's* `icvf` *map*

This map is closely related to `F_intra` and have both the same trends (even for the outliers). We will however prefer the `F_intra` map because in any case if we could assume the fraction CSF in the CC to be zeros, small variations could occur in `F_iso` that would be taken into account in `F_intra` making it more precise.

3.2.4 Fingerprinting

Fingerprinting the most promising microstructural algorithm, it will find two fiber populations and their respective fractions in order to better replicate diffusivity. (See Section 1.3.2). Since we happen to be studying the CC, the algorithm should theoretically find only one population of fibers oriented in a general direction. This is why we do not have a f_1 map. We will use the fraction of CSF contained in the `frac_csf` map along with the fraction of population 0 contained in map `frac_f`$_0$ and the total population fraction contained in map `fvf_tot`.

`frac_csf`

The CSF fraction (`frac_csf` : $\frac{csf}{f_0+f_1+csf}$) should be very low (in a perfect world it should not even exist) and would increase very little with cuprizone administration. This is due to the fact that we are working in the CC.

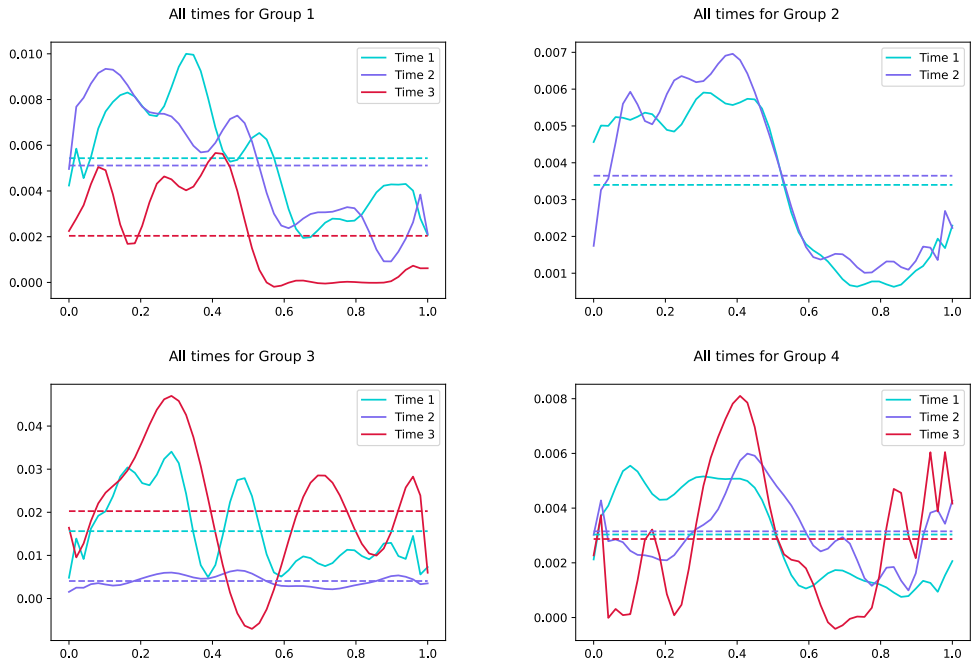

Figure 3.64: *Mean of Cerebrospinal fluid fraction for selected mice based on MF's* ***frac_csf*** *map*

As expected, the graphs don't make much sens; most values are very small and some are even zero (see group 1 time $T = 3$).

`frac_f`$_0$

Being the only population in the CC, population 0's fraction (`frac_f`$_0$: $\frac{f_0}{f_0+f_1+csf}$) should be high and drop under the influence of cuprizone. The algorithm will then replace the missing axons by CSF.

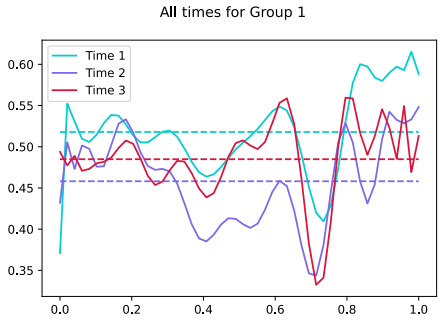

Figure 3.65:

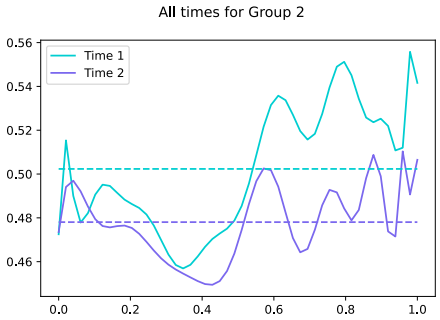

Figure 3.66:

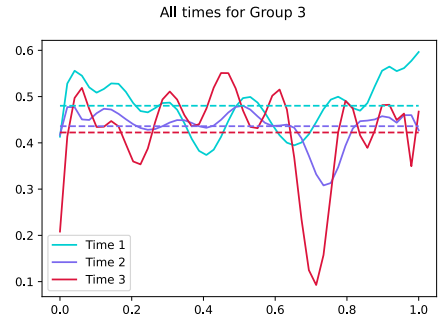

Figure 3.67:

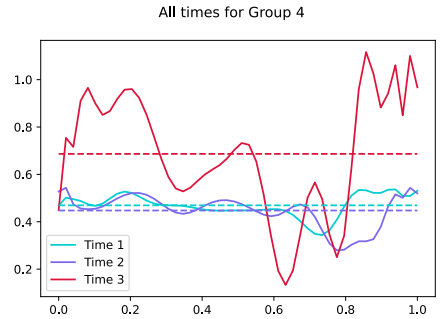

Figure 3.68:

Figure 3.69: *Mean of pop 0 fraction for selected mice based on MF's* $\texttt{frac_f}_0$ *map*

Group 2 is what is expected and what theory predicts (see Figure 3.66). Like `F_intra` in NODDI, the $\texttt{f}_0$ map presents the regional disparities (rostral and caudal) presented in Section 3.1. Group 3 behaves as expected; time $T = 3$ presents more disparities due to the fact that once again, time $T = 3$ only has one mouse. We can clearly see that time $T = 3$ of group 4 is an outlier as it's values exceed 1. Even if the scales are different between graphs, we observe about a 10% loss $\texttt{f}_0$ value in groups 2,3 and 4 for times $T = 1$.

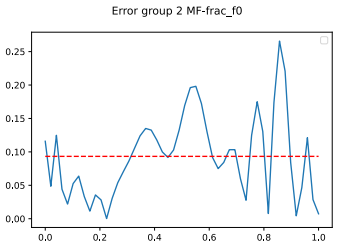

Figure 3.70:

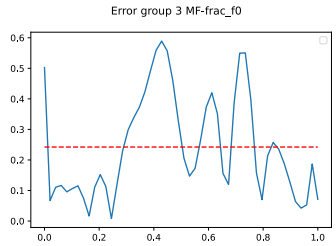

Figure 3.71:

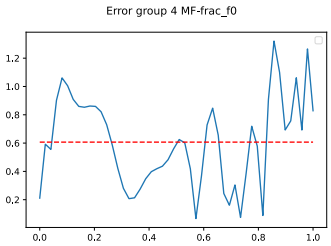

Figure 3.72:

Figure 3.73: *Error of MF's* $\texttt{frac_f}_0$ *map*

The error on group 2 clearly shows demyelination on the caudal section (from 0.5 to

1) as was expected. `F_intra` shows the same result. Group 3 error is about 25% which is acceptable. The spike around 0.7 at time $T = 3$ in Figure 3.67 should be smoother; i.e start beforehand around 0.5 and finish around 0.9. For group 4 once again, the error reaches high values (60%) because of the outlier mouse (group 4 time $T = 3$).

fvf_tot

The total fraction of population called `fvf_tot`= $\frac{f_0+f_1}{f_0+f_1+csf}$) should theoretically behave like `frac_f0` since there is no population f_1 in the CC.

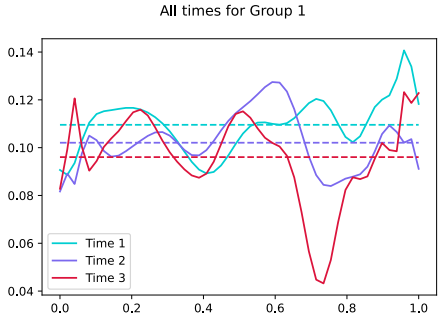

Figure 3.74:

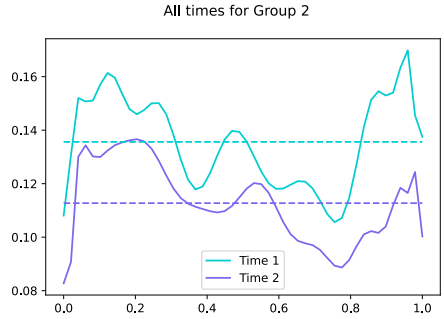

Figure 3.75:

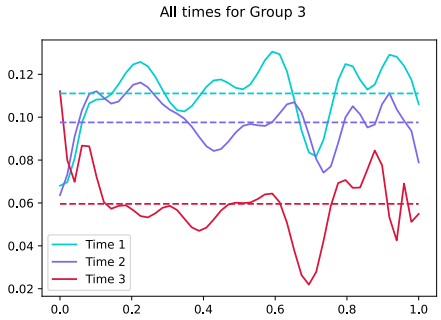

Figure 3.76:

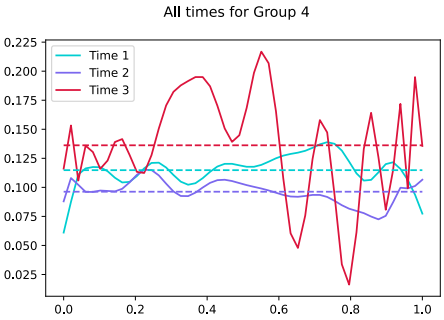

Figure 3.77:

Figure 3.78: *Mean of population fraction for selected mice based on MF's* ***`fvf_tot`*** *map*

Results aren't exactly the same as `frac_f0` but are similar to what we expected. Group 1 fits pretty nicely as all times are huddled together (±5%). The small variations can find their source in the lack of mice data (we invoke here the law of large numbers and our lack of large numbers). We can spot a decrease for groups 2 and 3 as expected although there is no sign of the caudal/rostral difference in Figure 3.75. Once again, the group 4 outlier (group 4 time $T = 3$) is much too high compared to other times. We will note however that compared to the other maps, this height difference isn't as important.

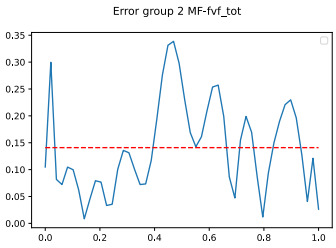

Figure 3.79:

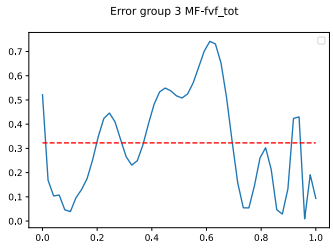

Figure 3.80:

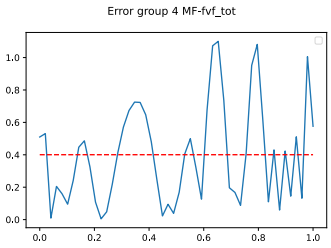

Figure 3.81:

Figure 3.82: *Error of MF's* ***fvf_tot*** *map*

The error on group 2 is less than 15% which is good. It is however higher than the `frac_f`$_0$ map because the loss in Figure 3.75 spans on the whole CC and is not only centered on the caudal region.

Which microstructure to better represent reality?

Even though the analysis builds upon a DTI calibration made using the `FA_rgb` map (cf Section 2.4) which predisposed DTI to be better, their results of `F_intra` map from NODDI and `fvf_tot` map from MF offer better results. From what we have seen in the previous section and their comparison with histology, we can select a few representative maps from the already pre-selected maps. Among the selected maps figure the `FA` map from DTI which gives us a pretty good result despite the bad quality of imaging. The three maps (for the three microstructural algorithms studied here) are `FA` fro DTI, `F_intra` for NODDI and `fvf_tot` for MF. To show which of them is the best at approximation, we took the group 3 data (15 weeks of cuprizone) as group 3 data shows group 1, 2 and 3 data all at once ($T = 1$ showing group 1 data, $T = 2$ showing group 2 data and $T = 3$ being specific to group 3). Group 4 could not be analysed because of the recurring outlier. To compare them will not use the error as defined in equation 3.3 but we will use the difference between the mean values of the curves. This scalar is defined as being the error in mean demyelination.

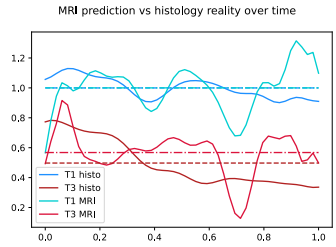

Figure 3.83: *DTI's* ***FA*** *map*

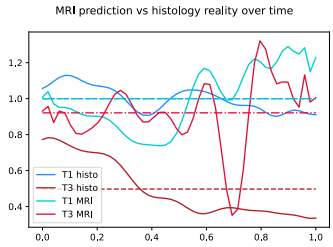

Figure 3.84: *NODDI's* ***F_intra*** *map*

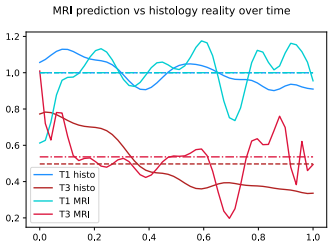

Figure 3.85: *MF's* ***fvf_tot*** *map*

Figure 3.86: *comparison into histology and MRI for group 3*

Having quantified the myelin loss after 15 weeks by a ratio of 2,014 in histology data (on average, group1 data is 2.014 higher than group 3 data), mice have a myelin density twice as low after 15 weeks of cuprizone feeding.

For DTI's `FA` maps, the value stands at 1.761 times less myelin after 15 weeks which corresponds to an error of 0.253 with the histoilogy data.

For NODDI's `F_intra`, we find a 1.086 myelin loss factor which amounts to a 0.98 error in regards to histology.

Finally for MF's `fvf-tot`, we find a myelin loss ratio worth 1.865 which gives an error of 0.149 in regards to histology.

We can conclude that, each proposed study has it's strengths and weaknesses. They have all shown at some point their precision and may not always be adapted to the problem. However, among the results and comparison, Microsture Fingerprinting (Rensonnet et al., 2019)[49] has shown more consistency with more precise maps ($\texttt{frac_f}_0$ and `fvf_tot`) and values. It is clear that the chosen maps and ranking are only valid from the point of view of our study and more experiments using our pipeline must be carried out in order to establish the dominance of an algorithm over the others. Moreover, each map brings some new information and using then jointly is highly recommended as things spotted in a map may be overlooked by another and vice versa.

Conclusion

We have reached the conclusion of our study. Through this study we have managed to elaborate an operational pipeline that takes DICOM files from a specific machines and leads them all the way to microstructural maps made by powerful algirthms (NODDI [78] or MF [49]). Moreover, overlooking the poor quality of our acquisitions, our pipeline has led to promising results using these microstructural algorithms, showing their capabilities on artifact-polluted images. The result of our analysis shows that among error factors a certain coherence when coregistered on histology data considered to be the truth. However, the analysis phase, being encouraging, was below our expectations in the sense that for many possible reasons (poor quality, bad interpretation, poorly designed dictonaries,...) the results don't fully match the histology observations taken to be the undeniable proof. And although these reasons must be investigated one day, we are confident that, with proper images of high quality, our pipeline, coupled to the powerful microstructural algorithms can conclusively predict with good precision the loss of myelin in the rats brains.

This conclusion can have large consequences in the medical field as diseases like Alzheimer or multiple sclerosis could then be predicted by only using MRI and processed images. But the applications of this pipeline could be broader and adapted to many situations. Already as study on brain tumors in mice using the same parameters we have used in our study as successfully used our pipeline to convert, denoise, correct and extract the brain. Once the proper dictionary created, MF will be able to predict the actual state of the tumor and multiple other parameters (as it has rather successfully done with the myelin degeneration) using only MRI. This would be an important breakthrough for artificial intelligence.

Of course, our pipeline can be largely perfected to include other artifact corrections such as TOPUP, or the correction of Gibbs ringing. It can be upgraded for non python users by adding a graphic interface that would allow easier manipulation and selection of tasks to be performed by the pipeline. But most importantly, it can be the brick on which is built a bigger structure that will one day help all of humanity prevail against illness.

Glossary

b **value** is a factor that reflects the strength and timing of the gradients used to generate diffusion-weighted images. The *b* value is physically expressed in Section 1.2.2. x, 14, 38

Alzheimer 's disease is a progressive neurologic disorder that causes the brain to shrink (atrophy) and brain cells to die. Alzheimer's disease is the most common cause of dementia — a continuous decline in thinking, behavioral and social skills that affects a person's ability to function independently. 3, 25, 33, 89

apparent diffusion coefficient is a measure of the magnitude of diffusion (of water molecules) within tissue, and is commonly clinically calculated using MRI with diffusion-weighted magnetic resonance imaging. x, 13, 15

cerebrospinal fluid is the fluid that flows in and around the hollow spaces of the brain and spinal cord, and between two of the meninges (the thin layers of tissue that cover and protect the brain and spinal cord). Cerebrospinal fluid is made by tissue called the choroid plexus in the ventricles (hollow spaces) in the brain. v, viii, x, 14, 15, 17–20, 75, 81, 84

circadian rhythm is a natural, endogenous process that controls the sleep–wake cycle and occurs every 24 hours or so. It can refer to any process that begins inside an organism and responds to its surroundings (entrained by the environment). 32

corpus callosum is a mass of white, transverse fibers connecting the cerebral hemispheres in human beings and in other higher mammals. i, ii, vii, x, 1, 3, 25, 30, 34, 37, 54, 57, 64, 65

diencephalon (or interbrain) is a forebrain division located between the telencephalon and the midbrain (embryonic prosencephalon) (embryonic mesencephalon). In ancient literature, the diencephalon was also known as the 'tweenbrain.' The thalamus, hypothalamus, epithalamus, and subthalamus are the structures on either side of the third ventricle that make up the thalamus. . 31, 32

diffusion tensor imaging is a promising method for characterizing microstructural changes or differences with neuropathology and treatment. The diffusion tensor may be used to

characterize the magnitude, the degree of anisotropy, and the orientation of directional diffusion. iii, x, 12, 16, 68

diffusion-weighted magnetic resonance imaging is the use of specific Magnetic Resonance Imaging (MRI) sequences as well as software that generates images from the resulting data that uses the diffusion of water molecules to generate contrast in. x, 12, 14, 21, 64, 90

fascicles is a bundle of nerve fibers. Each nerve contains many axons that are sometimes referred to as fibers. Within a nerve, each axon is surrounded by a layer of connective tissue called the endoneurium. The axons are bundled together into groups called fascicles. Each fascicle is wrapped in a layer of connective tissue called the perineurium. 20, 21

fractional anisotropy is a scalar value between zero and one that describes the degree of anisotropy of a diffusion process. A value of zero means that diffusion is isotropic, i.e. it is unrestricted (or equally restricted) in all directions. A value of one means that diffusion occurs only along one axis and is fully restricted along all other directions. FA is a measure often used in diffusion imaging where it is thought to reflect fiber density, axonal diameter, and myelination in white matter. The FA is an extension of the concept of eccentricity of conic sections in 3 dimensions, normalized to the unit range. x, 17, 74, 76

glial cells (from the Greek "$\gamma\lambda o\iota o\sigma$", which meaning "sticky") are the cells that surround and provide an environment for neurons in the nervous system. By supplying nutrients and oxygen, removing dead cells, and battling pathogens, they assist to maintain the body's steady temperature, encourage the creation of myelin in the brain, and protect and sustain nerve tissue. Glial cells, known as "white matter," constitute over half of the brain's total volume. 13, 18, 19, 22, 35, 80, 92, 93

limbic system also known as the paleomammalian cortex, is a collection of brain regions largely in the forebrain that are positioned on both sides of the thalamus, immediately behind the medial temporal lobe of the cerebrum. It helps with emotions, behavior, long-term memory, and olfaction, among other things. The limbic system is mostly responsible for emotional life, and it is essential for memory development. 32, 33

Monte Carlo simulations also known as the Monte Carlo experiments, are a general category of computational algorithms that produce numerical results by repeatedly drawing from a random pool. The fundamental idea is to make use of chance in order to find solutions to problems that, in theory, might be solved using deterministic methods. They are beneficial in situations where it is difficult or impossible to employ other methods, which is where they are most commonly applied in the realms of mathematics and physics. Optimization, numerical integration, and the generation

of draws from a probability distribution are the three primary application areas for Monte Carlo methods. 21

Multi-Slice-Multi-Echo (also referred to as Multi Echo T2) is an imaging sequence following to T2 time where the magnetisation wave decreases exponentially and acquisitions are made every T time steps. This gives rise to a series of images that are very bright at first due to the high energy of the wave and decrease in intensity (proportionally to the wave's energy over time). xi, 41

multiple sclerosis is a chronic, typically progressive disease involving damage to the sheaths of nerve cells in the brain and spinal cord, whose symptoms may include numbness, impairment of speech and of muscular coordination, blurred vision, and severe fatigue. xi, 3, 25–27, 37, 89

myelin is a lipid-rich material that surrounds nerve cell axons (the nervous system's "wires") to insulate them and increase the rate at which electrical impulses (called action potentials) are passed along the axon. The myelinated axon can be likened to an electrical wire (the axon) with insulating material (myelin) around it. However, unlike the plastic covering on an electrical wire, myelin does not form a single long sheath over the entire length of the axon. Rather, myelin sheaths the nerve in segments: in general, each axon is encased with multiple long myelinated sections with short gaps in between called nodes of Ranvier. i, ii, vii, ix, 2, 26, 28, 29, 37, 54, 57, 59–62, 65–70, 73, 74, 77–79, 81, 88, 89, 91, 92, 136–138

neocortex also known as the neopallium, isocortex, or six-layered cortex, is a group of layers in the mammalian cerebral cortex that are involved in higher-order brain activities as sensory perception, cognition, motor command production, spatial reasoning, and language. The real isocortex and the proisocortex are two subtypes of the neocortex. 31–33

neurites are any projection that emerge from the neuron's cell body. The projection may be an axon or a dendrite, depending on its nature. In developmental biology, immature nerve cells are typically referred to as such, especially when produced in culture, because it is difficult to distinguish between the two types of projections. 18–20, 80

oligodendrocyte progenitor cells Oligodendrocyte progenitor cells (OPCs) are a subtype of glial cells responsible for myelin regeneration. Oligodendrocytes (OLGs) originate from OPCs and are the myelinating cells in the central nervous system (CNS). OLGs play an important role in the context of lesions in which myelin loss occurs. Even though many protocols for isolating OPCs have been published, their cellular yield remains a limit for clinical application. see (Zhang et al., 2019) [79]. xi, 27, 67

principal component analysis is used to create predictive models and for exploratory data analysis. It is frequently used to acquire lower-dimensional data while retaining the most of the data's variation by projecting each data point onto only the first few principal components. The path that maximizes the variance of the projected data can also be used to define the first main component. The route orthogonal to the first $i-1$ principal components that maximizes the variance of the projected data is the i-th principal component. See more information here . xi, 23, 43

pulse gradient echo spin is a spin echo sequence with 90° and 180° pulses, with phases x and y, separated by the delay τ. A pair of gradient pulses with duration δ and incremented amplitude G is used to encode the signal for translational motion during the diffusion time Δ. xi, 13

soma (singular soma) are bodies of organisms as contrasted with their germ cells. 13, 18, 19, 35, 36, 80

substantia nigra is a basal ganglia structure located in the midbrain that plays an important role in reward and movement. Substantia nigra is Latin for "black substance", reflecting the fact that parts of the substantia nigra appear darker than neighboring areas due to high levels of neuromelanin in dopaminergic neurons. Parkinson's disease is characterized by the loss of dopaminergic neurons in the substantia nigra pars compacta. 33, 34

subventricular zone is a region situated on the outside wall of each lateral ventricle of the vertebrate brain. It is present in both the embryonic and adult brain. In embryonic life, the subventricular zone refers to a secondary proliferative zone containing neural progenitor cells, which divide to produce neurons in the process of neurogenesis. The primary neural stem cells of the brain and spinal cord, called radial glial cells, instead reside in the ventricular zone (VZ) (so-called because the VZ lines the inside of the developing ventricles). xi, 1

voxel (in computer-based modelling or graphic simulation) each of an array of elements of volume that constitute a notional three-dimensional space, especially each of an array of discrete elements into which a representation of a three-dimensional object is divided. 4, 16–18, 20–22, 25, 38, 44, 53, 74

Bibliography

[1] A. L. Alexander, J. E. Lee, and A. S. Lazar, M.and Field, Diffusion tensor imaging of the brain., Neurotherapeutics : the journal of the American Society for Experimental NeuroTherapeutics, 4(3) (2007), p. 316–329.

[2] H. Alturkistani, F. Tashkandi, and Z. Mohammedsaleh, Histological stains: A literature review and case study, Global Journal of Health Science, 8 (2015).

[3] B. B. Avants, N. Tustison, G. Song, et al., Advanced normalization tools (ants), Insight j, 2 (2009), pp. 1–35.

[4] A. W. Barritt, M. C. Gabel, M. Cercignani, and P. N. Leigh, Emerging magnetic resonance imaging techniques and analysis methods in amyotrophic lateral sclerosis, Frontiers in Neurology, 9 (2018).

[5] M. D. Binder, H. S. Cate, A. L. Prieto, D. Kemper, H. Butzkueven, M. M. Gresle, T. Cipriani, V. G. Jokubaitis, P. Carmeliet, and T. J. Kilpatrick, Gas6 deficiency increases oligodendrocyte loss and microglial activation in response to cuprizone-induced demyelination, Journal of Neuroscience, 28 (2008), pp. 5195–5206.

[6] V. P. Bingman, C. Salas, and F. Rodriguez, Evolution of the Hippocampus, Springer Berlin Heidelberg, Berlin, Heidelberg, 2009, pp. 1356–1360.

[7] J. G. Black and L. J. Black, Microbiology: principles and explorations, John Wiley & Sons, 2018.

[8] A. Brun and E. Englund, Cbrain changes in dementia of alzheimer's type relevant to new imaging diagnostic methods., Progress in Neuro-Psychopharmacology and Biological Psychiatry, 10 (1986), pp. 297–308.

[9] J. Cheng, Sampling in q-space, 2017. Last accessed 16 May 2022.

[10] A. M. Colman, dentate gyrus, 2015.

[11] K. L. Davis, D. G. Stewart, J. I. Friedman, M. Buchsbaum, P. D. Harvey, P. R. Hof, J. Buxbaum, and V. Haroutunian, White Matter Changes in Schizophrenia: Evidence for Myelin-Related Dysfunction, Archives of General Psychiatry, 60 (2003), pp. 443–456.

[12] F. Dell'Acqua, L. Lacerda, M. Catani, and A. Simmons, Anisotropic power maps: a diffusion contrast to reveal low anisotropy tissues from hardi data, in Proc Intl Soc Mag Reson Med, vol. 22, 2014, pp. 29960–29967.

[13] Q. Dessain, M. Simon, and B. Macq, Development of an image processing pipeline for large-scale in vivo population studies of the brain microstructure, Master's thesis, UCLouvain, 2021.

[14] B. Dubois, H. Hampel, H. H. Feldman, P. Scheltens, P. Aisen, S. Andrieu, H. Bakardjian, H. Benali, L. Bertram, K. Blennow, K. Broich, E. Cavedo, S. Crutch, J.-F. Dartigues, C. Duyckaerts, S. Epelbaum, G. B. Frisoni, S. Gauthier, R. Genthon, A. A. Gouw, M.-O. Habert, D. M. Holtzman, M. Kivipelto, S. Lista, J.-L. Molinuevo, S. E. O'Bryant, G. D. Rabinovici, C. Rowe, S. Salloway, L. S. Schneider, R. Sperling, M. Teichmann, M. C. Carrillo, J. Cummings, C. R. Jack Jr, and Proceedings of the Meeting of the International Working Group (IWG) and the American Alzheimer's Association on "The Preclinical State of AD"; July 23, 2015; Washington DC, USA , Preclinical alzheimer's disease: Definition, natural history, and diagnostic criteria, Alzheimer's & Dementia, 12 (2016), pp. 292–323.

[15] S. Eloul and R. G. Compton, General model of hindered diffusion, The Journal of Physical Chemistry Letters, 7 (2016), pp. 4317–4321.

[16] V. Fernández, C. Llinares-Benadero, and V. Borrell, Cerebral cortex expansion and folding: what have we learned?, The EMBO Journal, 35 (2016), pp. 1021–1044.

[17] S. Ferraris, I. D. Shakir, J. Van Der Merwe, W. Gsell, J. Deprest, and T. Vercauteren, Bruker2nifti: Magnetic resonance images converter from bruker paravision to nifti format, Journal Of Open Source Software, 2 (2017), p. 354.

[18] R. Fick, R. Deriche, and D. Wassermann, The dmipy toolbox: Diffusion mri multi-compartment modeling and microstructure recovery made easy, Oct 2019.

[19] B. Fischl, Freesurfer, NeuroImage, 62 (2012), pp. 774–781. 20 YEARS OF fMRI.

[20] R. J. Galvin, D. Regan, and J. R. Heron, A possible means of monitoring the progress of demyelination in multiple sclerosis: effect of body temperature on visual perception of double light flashes., Journal of Neurology, Neurosurgery & Psychiatry, 39 (1976), pp. 861–865.

[21] E. Garyfallidis, M. Brett, B. Amirbekian, A. Rokem, S. Van Der Walt, M. Descoteaux, and I. Nimmo-Smith, Dipy, a library for the analysis of diffusion mri data, Frontiers in Neuroinformatics, 8 (2014).

[22] N. Gholizadeh, P. Greer, and J. Simpson, Characterization of prostate cancer using diffusion tensor imaging: A new perspective., European journal of radiology, 110 (2019), pp. 112–120.

[23] J. Hillis, J. Davies, M. Mundim, O. Al Dalahmah, and F. Szele, Cuprizone demyelination induces a unique inflammatory response in the subventricular zone, Journal of Neuroinflammation, 13 (2016).

[24] W. Hodos, Evolution of Cerebellum, Springer Berlin Heidelberg, Berlin, Heidelberg, 2009, pp. 1240–1243.

[25] T. Huisman, Diffusion-weighted and diffusion tensor imaging of the brain, made easy., Cancer Imaging., 2 (2010), pp. 163–171.

[26] IMAIOS, Imaos mri course, 2008. Last accessed 16 July 2022.

[27] K. Irvine and W. Blakemore, Remyelination protects axons from demyelination-associated axon degeneration, Brain, 131 (2008), pp. 1464–1477.

[28] I. O. Jelescu, M. Zurek, K. Winters, J. Veraart, A. Rajaratnam, T. M. Shepherd, D. S. Novikov, S. G. Kim, and E. Fieremans, Longitudinal study of cuprizone-induced white matter degeneration and recovery using diffusion white matter tract integrity metrics (wmti)., in Proc. Intl. Soc. Mag. Reson. Med, vol. 23, 2015, p. 3000.

[29] I. O. Jelescu, M. Zurek, K. V. Winters, J. Veraart, A. Rajaratnam, N. S. Kim, J. S. Babb, T. M. Shepherd, D. S. Novikov, S. G. Kim, et al., In vivo quantification of demyelination and recovery using compartment-specific diffusion mri metrics validated by electron microscopy, Neuroimage, 132 (2016), pp. 104–114.

[30] M. Jenkinson, C. F. Beckmann, T. E. Behrens, M. W. Woolrich, and S. M. Smith, Fsl, NeuroImage, 62 (2012), pp. 782–790. 20 YEARS OF fMRI.

[31] B. Jeurissen, A. Leemans, J.-D. Tournier, D. K. Jones, and J. Sijbers, Investigating the prevalence of complex fiber configurations in white matter tissue with diffusion magnetic resonance imaging, Human Brain Mapping, 34 (2013), pp. 2747–2766.

[32] H. Johansen-Berg and T. E. Behrens, Diffusion MRI: from quantitative measurement to in vivo neuroanatomy, Academic Press, 2013.

[33] E. Jones, The Thalamus, Plenum Press, 1985.

[34] K. Kinnunen, R. Greenwood, and P. J. et al., Cwhite matter damage and cognitive impairment after traumatic brain injury., Brain, 134 (2011), pp. 449–463.

[35] D. Le Bihan and S. Warach, Diffusion and perfusion magnetic resonance imaging, Journal of Computer Assisted Tomography, 19 (1995), p. 844.

[36] L. A. Lemaire, C. Cao, P. H. Yoon, J. Long, and M. Levine, The hypothalamus predates the origin of vertebrates, Science Advances, 7 (2021), p. eabf7452.

[37] M. Lindner, S. Heine, K. Haastert, N. Garde, J. Fokuhl, F. Linsmeier, C. Grothe, W. Baumgärtner, and M. Stangel, Sequential myelin protein expression during remyelination reveals fast and efficient repair after central nervous system demyelination, Neuropathology and Applied Neurobiology, 34 (2008), pp. 105–114.

[38] K. V. Mardia, P. E. Jupp, and K. Mardia, Directional statistics, vol. 2, Wiley Online Library, 01 2000.

[39] K. Marstal, F. Berendsen, M. Staring, and S. Klein, Simpleelastix: A user-friendly, multi-lingual library for medical image registration, International Workshop on Biomedical Image Registration (WBIR), (2016).

[40] J. H. Martin, Neuroanatomy: Text and Atlas, 5e, McGraw Hill, New York, NY, 2021.

[41] G. K. Matsushima and P. Morell, The neurotoxicant, cuprizone, as a model to study demyelination and remyelination in the central nervous system, Brain Pathology, 11 (2001), pp. 107–116.

[42] K. Mori, Y. K. Takahashi, K. M. Igarashi, and M. Yamaguchi, Maps of odorant molecular features in the mammalian olfactory bulb, Physiological Reviews, 86 (2006), pp. 409–433. PMID: 16601265.

[43] A. Ozturk, S. Smith, E. Gordon-Lipkin, D. Harrison, N. Shiee, D. L. Pham, B. Caffo, P. A. Calabresi, and D. S. Reich, Mri of the corpus callosum in multiple sclerosis: association with disability, Multiple Sclerosis Journal, 16 (2010), pp. 166–177.

[44] E. Pasquini, K. Corriveau, M. Koenig, and P. Harris, Preschoolers monitor the relative accuracy of informants, Developmental psychology, 43 (2007), pp. 1216–26.

[45] J. R. Patel, E. E. McCandless, D. Dorsey, and R. S. Klein, Cxcr4 promotes differentiation of oligodendrocyte progenitors and remyelination, Proceedings of the National Academy of Sciences, 107 (2010), pp. 11062–11067.

[46] S. Patergnani, V. Fossati, M. Bonora, C. Giorgi, S. Marchi, S. Missiroli, T. Rusielewicz, M. Wieckowski, and P. Pinton, Mitochondria in multiple sclerosis: Molecular mechanisms of pathogenesis., Journal of the Neurological Sciences, 356 (2015), pp. 55–60.

[47] J. Praet, C. Guglielmetti, Z. Berneman, A. Van der Linden, and P. Ponsaerts, Cellular and molecular neuropathology of the cuprizone mouse model: Clinical relevance for multiple sclerosis, Neuroscience & Biobehavioral Reviews, 47 (2014), pp. 485–505.

[48] P. Rakic, Evolution of the neocortex: a perspective from developmental biology, Nature Reviews Neuroscience, 10 (2009), pp. 724–735.

[49] G. Rensonnet, B. Macq, and J.-P. Thiran, In vivo diffusion magnetic resonance imaging of the white matter microstructure from dictionaries generated by Monte Carlo simulations : development and validation, PhD thesis, UCLouvain, 2019.

[50] G. Rensonnet, B. Scherrer, G. Girard, A. Jankovski, S. Warfield, B. Macq, J.-P. Thiran, and M. Taquet, Towards microstructure fingerprinting: Estimation of tissue properties from a dictionary of monte carlo diffusion mri simulations, NeuroImage, 184 (2018).

[51] A. M. Roberts, The complete human body, Dorling Kindersley Ltd, 2010.

[52] C. Rorden, Mricron.

[53] K. Saladin, Human Anatomy, McGraw-Hill, 2011.

[54] C. B. Saper, T. E. Scammell, and J. Lu, Hypothalamic regulation of sleep and circadian rhythms, Nature, 437 (2005), pp. 1257–1263.

[55] B. Scherrer, A. Schwartzman, M. Taquet, M. Sahin, S. Prabhu, and S. Warfield, Characterizing brain tissue by assessment of the distribution of anisotropic microstructural environments in diffusion-compartment imaging (diamond): Characterizing brain tissue with diamond, Magnetic Resonance in Medicine, 76 (2016), pp. spcone–spcone.

[56] J. D. Schmahmann and D. Caplan, Cognition, emotion and the cerebellum, Brain, 129 (2006), pp. 290–292.

[57] S. Shostak, Histology's nomenclature: Past, present and future, Biol Syst Open Access, 2 (2013), p. 2.

[58] T. Skripuletz, V. Gudi, D. Hackstette, and M. Stangel, De-and remyelination in the cns white and grey matter induced by cuprizone: the old, the new, and the unexpected, Histology and histopathology, Vol. 26, n°12 (2011), (2011).

[59] T. Skripuletz, M. Lindner, A. Kotsiari, N. Garde, J. Fokuhl, F. Linsmeier, C. Trebst, and M. Stangel, Cortical demyelination is prominent in the murine cuprizone model and is strain-dependent, The American Journal of Pathology, 172 (2008), pp. 1053–1061.

[60] A. J. Steelman, J. P. Thompson, and J. Li, Demyelination and remyelination in anatomically distinct regions of the corpus callosum following cuprizone intoxication, Neuroscience Research, 72 (2012), pp. 32–42.

[61] E. O. Stejskal and J. E. Tanner, Spin diffusion measurements: spin echoes in the presence of a time-dependent field gradient, The journal of chemical physics, 42 (1965), pp. 288–292.

[62] M. F. Stidworthy, S. Genoud, U. Suter, N. Mantei, and R. J. Franklin, Quantifying the early stages of remyelination following cuprizone-induced demyelination, Brain pathology, 13 (2003), pp. 329–339.

[63] N. L. Strominger, R. J. Demarest, and L. B. Laemle, Cerebral Cortex, Humana Press, Totowa, NJ, 2012, pp. 429–451.

[64] E. Süli and D. F. Mayers, An introduction to numerical analysis, Cambridge university press, 2003.

[65] I. Tagge, A. O'Connor, P. Chaudhary, J. Pollaro, Y. Berlow, M. Chalupsky, D. Bourdette, R. Woltjer, M. Johnson, and W. Rooney, Spatio-temporal patterns of demyelination and remyelination in the cuprizone mouse model, PLOS ONE, 11 (2016), pp. 1–24.

[66] M. Titford, Progress in the development of microscopical techniques for diagnostic pathology, Journal of Histotechnology, 32 (2009), pp. 9–19.

[67] R. Tomioka and M. Matsui, Biomarkers for multiple sclerosis., Intern Med., 53 (2014), pp. 361–365.

[68] O. Torkildsen, L. Brunborg, K.-M. Myhr, and L. Bø, The cuprizone model for demyelination., Acta Neurol Scand, 117 (2008), p. 72–76.

[69] J.-D. Tournier, R. Smith, D. Raffelt, R. Tabbara, T. Dhollander, M. Pietsch, D. Christiaens, B. Jeurissen, C.-H. Yeh, and A. Connelly, Mrtrix3: A fast, flexible and open software framework for medical image processing and visualisation, Neuroimage, 202 (2019), p. 116137.

[70] R. Van der Sar, E. Ødegård, E. Brouwers, I. Goor, and H. Garretsen, Acceptance of illicit drug use in the netherlands and norway: A cross-national survey, Drugs: Education, Prevention, and Policy, 19 (2012).

[71] G. Venturini, Enzymic activities and sodium, potassium and copper concentrations in mouse brain and liver after cuprizone treatment in vivo, Journal of Neurochemistry, 21 (1973), pp. 1147–1151.

[72] D. Vetter and B. Kastler, Comprendre l'IRM, manuel d'auto-apprentissage, ELSEVIER-MASSON, 2018.

[73] U. Wolf, M. J. Rapoport, and T. A. Schweizer, Evaluating the affective component of the cerebellar cognitive affective syndrome, The Journal of Neuropsychiatry & Clinical Neurosciences, 21 (2009), pp. 245–253. PMID: 19776302.

[74] Q.-Z. Wu, Q. Yang, H. S. Cate, D. Kemper, M. Binder, H.-X. Wang, K. Fang, M. J. Quick, M. Marriott, T. J. Kilpatrick, et al., Mri identification of the rostral-caudal pattern of pathology within the corpus callosum in the cuprizone mouse model, Journal of Magnetic Resonance Imaging: An Official Journal of the International Society for Magnetic Resonance in Medicine, 27 (2008), pp. 446–453.

[75] M. Xie, J. E. Tobin, M. D. Budde, C.-I. Chen, K. Trinkaus, A. H. Cross, D. P. McDaniel, S.-K. Song, and R. C. Armstrong, Rostrocaudal analysis of corpus callosum demyelination and axon damage across disease stages refines diffusion tensor imaging correlations with pathological features, Journal of Neuropathology & Experimental Neurology, 69 (2010), pp. 704–716.

[76] H.-J. Yang, H. Wang, Y. Zhang, L. Xiao, R. W. Clough, R. Browning, X.-M. Li, and H. Xu, Region-specific susceptibilities to cuprizone-induced lesions in the mouse forebrain: Implications for the pathophysiology of schizophrenia, Brain research, 1270 (2009), pp. 121–130.

[77] P. A. Yushkevich, Y. Gao, and G. Gerig, Itk-snap: An interactive tool for semi-automatic segmentation of multi-modality biomedical images, in 2016 38th Annual International Conference of the IEEE Engineering in Medicine and Biology Society (EMBC), IEEE, 2016, pp. 3342–3345.

[78] H. Zhang, T. Schneider, C. A. Wheeler-Kingshott, and D. C. Alexander, Noddi: Practical in vivo neurite orientation dispersion and density imaging of the human brain, NeuroImage, 61 (2012), pp. 1000–1016.

[79] Y. Zhang, X.-Y. Lu, G. Casella, J. Tian, Z.-Q. Ye, T. Yang, J.-J. Han, L.-Y. Jia, A. Rostami, and X. Li, Generation of oligodendrocyte progenitor cells from mouse bone marrow cells, Frontiers in Cellular Neuroscience, 13 (2019).

Appendix A

brain extraction

To better visualize how erosions and dilations constitute opening and closing sequences, the following figures are constructed as a series of erosion and dilation (in different orders) that make the opening and closing operation.

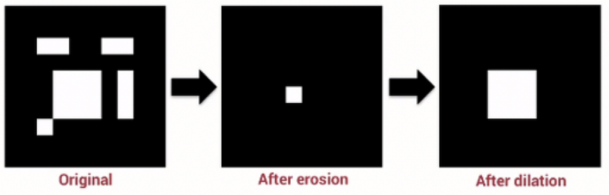

Figure A.1: *Opening*

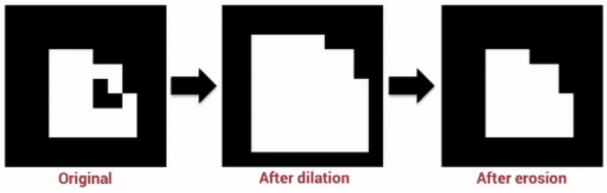

Figure A.2: *Closing*

Appendix B

Polynomial interpolation and approximation

This chapter is developed to motivate our choice when analysing the data and approximating the data. The following is taken from (Endre Süli, 2003)[64]. In order for us to approximate unknown function (i.e a set of points) the following theory is important to understand the environment in which the approximation can be done.

B.1 Polynomial interpolation

Usually, the use of Lagrangian polynomials is wildly implemented. Let us remind the reader that the interpolation function $p_n(x)$ passes exactly by the points of interpolation $x_i, f(x_i)$ satisfying the equation:

$$f(x_i) = p_n(x_i) = y_i \tag{B.1}$$

B.1.1 Different interpolations

The interpolation of such a problem is equivalent to the following:
Find $(a_0, \ldots, a_n) \in \mathbb{R}$ such that

$$\sum_{j=0}^{n} a_j \phi_j(x) = y_i \tag{B.2}$$

It means solving the following linear system:

$$\begin{pmatrix} \phi_0(x_0) & \phi_1(x_0) & \ldots & \phi_n(x_0) \\ \phi_0(x_1) & \phi_1(x_1) & \ldots & \phi_n(x_1) \\ \vdots & \vdots & \ddots & \vdots \\ \phi_0(x_n) & \phi_1(x_n) & \ldots & \phi_n(x_n) \end{pmatrix} \cdot \begin{pmatrix} a_0 \\ a_1 \\ \vdots \\ a_n \end{pmatrix} = \begin{pmatrix} y_0 \\ y_1 \\ \vdots \\ y_n \end{pmatrix} \tag{B.3}$$

Vandermonde Matrix

Lets start by adopting a base function $\phi_j(x)$ a set of monomes $(x^0, \ldots, x^j)$. The interpolation we are looking for is a polynome of degree n of the form $p_n(x) = a_0 + \ldots + a_n x^n$. Equation B.3) leads us to the Vandermonde Matrix

$$\begin{pmatrix} 1 & x_0 & \ldots & x_0^n \\ 1 & x_1 & \ldots & x_1^n \\ \vdots & \vdots & \ldots & \vdots \\ 1 & x_n & \ldots & x_n^n \end{pmatrix} \begin{pmatrix} a_0 \\ a_1 \\ \vdots \\ a_n \end{pmatrix} = \begin{pmatrix} y_0 \\ y_1 \\ \vdots \\ y_n \end{pmatrix} \tag{B.4}$$

With a linear system as we have found, (n equations, n unknowns), there exists only one interpolation polynomial of degree at most n that passes through $n + 1$ points of distinct abcissa.

Lagrange interpolation formula

By taking the case where the Vandermonde Matrix is equal to the identity matrix, **I**, we get the Lagrange interpolation polynomial defined by:

$$L_i(x) = \frac{(x - x_0) \ldots (x - X_{i-1})(x - X_{i+1}) \ldots (x - X_n)}{(x_i - x_0) \ldots (x_i - X_{i-1})(x_i - X_{i+1}) \ldots (x_i - X_n)} = \prod_{i=0, i \neq k}^{n} \frac{(x - x_i)}{(x_k - x_i)} \tag{B.5}$$

Since $L_i(X_j)$ is the identity if $i = j$ and zero otherwise, solving this problem becomes trivial:

$$p_n(x) = \sum_{i=0}^{n} y_i L_i$$

Chebyshev polynomials

Definition B.1.1. *The Chebyshev polynomial T_n of degree n is defined, for $x \in [-1, 1]$ by:*

$$T_n(x) = \cos(n \cos^{-1}(x)) \tag{B.6}$$

Despite it's usual form, T_n is a polynomial in disguise. For example, $T_0 = 1, T_1 = x$ and so on. In order to show that this is true in general, we recall the trigonometric identity $\cos((n+1)\theta) + \cos((n-1)\theta) = 2\cos(\theta)\cos(n\theta)$ and set $\theta = \cos^{-1}(x)$ to obtain the recurrence relationship:

$$T_{n+1}(x) = 2xT_n(x) - T_{n-1} \tag{B.7}$$

Since we've shown that T_0 and T_1 are polynomials on $[-1, 1]$, we deduce by induction that they all are.

- $T_0 = 1$
- $T_1 = x$

- $T_2 = 2x^2 - 1$
- $T_3 = 4x^3 - 3x$
- $T_4 = 8x^4 - 8x^2 + 1$
- $\vdots$

For $n \geq 1$, the zeros of T_n are at $x_j = \cos\left(\frac{(2j-1)\pi}{2n}\right)$. On any set $[a, b]$ the abcissa become $x_j = \frac{a+b}{2} + \frac{b-a}{2}\cos\left(\frac{\pi j}{n}\right)$

Lemma B.1.1. *The Chebyshev polynomials have the following properties:*

1 $T_{n+1} = 2xT_n - T_{n-1}$ *on* $x \in [-1, 1]$

2 for $n \geq 1, T_n$ *is a polynomial in* x *of degree* n *on* $[-1, 1]$*, with leading coefficient* $2^{n-1}x^n$

3 T_n *is an even function on* $[-1, 1]$ *if* n *is even and odd function if* n *is odd.*

4 For $n \geq 1$ *the zeros of* T_n *are at* $x_j = cos\left(\frac{(2j-1)\pi}{2n}\right)$

5 $|T_n(x)| \leq 1$ *for all* x *on the interval* $[-1, 1]$

6 for $n \geq 1, T - n(x) = \pm 1$*alternately at the* $n + 1$ *points* $x_k = \cos(\frac{k\pi}{n})$

B.1.2 About Lagrange interpolation

Lemma B.1.2. *Suppose* $n \geq 1$, $\exists L_k \in \mathcal{P}_n$ *such that*

$$L_k(x_i) = \begin{cases} 1 & i = k \\ 0 & i \neq k \end{cases}$$

satisfies the interpolation condition

Remark. *Although the lemma requires* $n \geq 1$*, the trivial case at the beginning can also be included by defining for* $n = 0, L_0 \equiv 1$*, and observing that the function* p_0 *defined by* $p_0 = L_0(x)y_0 \equiv y_0$ *is the unique polynomial in* $\mathcal{P}_0$ *that satisfies* $p_0(x) = y_0$*.*

We note that, implicitly $L_k(x)$ *depend on the polynomial degree* n*.* $L_k(x) = L_k^n(x) \neq L_k^m(x)$

Theorem B.1.3. ***Lagrange interpolation*** *Assume that* $n \geq 0$*. Let* x_i *be distinct real numbers and suppose that* y_i *are also* $(i = 0, \ldots, n)$*. Then* $\exists$ *a unique polynomial* $p_n(x) \in \mathcal{P}_n$ *such that*

$$p_n(x_i) = y_i \qquad \forall i = 0, \ldots, n \tag{B.8}$$

The proof is in 2 parts (existence and uniqueness). Existence is trivial since Lagrange polynomials are by definition built to exist for such a case. Uniqueness is proven by contradiction and supposing another exist then showing they are the same.

Proof. **Existence** From the previous remark $n = 0$ is trivial. For $n \geq 1$, it follows from Lemma 1.2.1 that the polynomial $p_n \in \mathcal{P}_n$ defined by $p_n(x) = \sum_{k=0}^{n} L_k(x)y_k$ satisfies the conditions $p_n(x_i) = y_i$ thus showing the existence of the required polynomial.

Uniqueness Suppose p_n is not unique. $\exists q_n \in \mathcal{P}_n$ with $p_n \neq q_n$ such that $q_n(x_i) = y_i$. Then $p_n - q_n \in \mathcal{P}_n$ has $n + 1$ distinct roots x_i. Since a polynomial of degree n cannot have more than n roots unless it's identically 0, it follows that $p_n(x) = q_n(x)$ thus showing uniqueness □

Theorem B.1.4. *Suppose that $n \geq 0$ and that f is a real valued function defined continuous and closed on $[a, b]$ such that the $n + 1$ derivates exist and are continuous on $[a, b]$. Then given that $x \in [a, b], \exists \xi = \xi(x) \in [a, b]$ such that:*

$$e(x) = f(x) - p_n(x) = \frac{f^{(n+1)}(\xi)}{(n+1)!}\pi_{n+1}(x) \tag{B.9}$$

Where $\pi_{n+1}(x) = (x - x_0)(x - x_1)\dots(x - x_n)$. Moreover:

$$|f(x) - p_n(x) \leq \frac{M_{n+1}}{(n+1)!}|\pi_{n+1}(x)| \tag{B.10}$$

Where $M_{n+1} = \max_{\zeta \in [a,b]} |f^{(n+1)}(\zeta)|$

The idea of the proof is to build a special function and to apply Rolle's theorem to all derivatives until $n + 1$ to establish the result. ‘

Proof. When $x = x_i, |f(x_i) - p_n(x_i)| = \frac{M_{n+1}}{(n+1)!}\pi_{n+1}(x) = 0$.

Suppose now $x \in [a, b]$ and $x \neq x_i$. For such values, let us consider the function $t \mapsto \phi(t)$ defined on $[a, b]$ by:

$$\phi(t) = f(t) - p_n(t) - \frac{f(x) - p_n(x)}{\pi_{n+1}(x)}\pi_{n+1}(t)$$

Clearly, $\phi(x_i) = 0$ when $x = x_i$ and $\phi(x) = 0$. Thus $\phi(t)$ vanishes at $n + 2$ points in $[a, b]$. By applying Rolle's theorem $\phi'(t)$ vanishes at $n + 1$ points in $[a, b]$; one between each consectutive points at which $\phi(t)$ vanishes. If $n = 0, \exists \xi = \xi(x) \in [a, b]$ such that $\phi'(\xi) = 0$. Since $p_0(x) \equiv f(x_0)$ (see first remark) and $\pi_1(t) = t - x_0$ it follows that

$$0 = \phi'(\xi) = f'(\xi) - \frac{f(\xi) - p_0(\xi)}{\pi_1(x)}$$

Suppose now $n \geq 1$, by using Rolle's theorem on $\phi''(t), \dots, \phi^{(n+1)}(t)$ it follows that:

$$0 = \phi^{(n+1)}(\xi) = f^{(n+1)}(\xi) - \frac{f(\xi) - p_0(\xi)}{\pi_1(x)}(n + 1)!$$

Hence $f(x) - p_n(x) = \frac{f^{(n+1)}(\xi)}{(n+1)!}\pi_{n+1}(x)$ □

Remark. *The Runge phenomenon can be explain using the previous theorem. Indeed one could ask onself what happens to*

$$\lim_{n\mapsto\infty} \frac{M_{n+1}}{(n+1)!}\pi_{n+1}(x)$$

when $n \mapsto \infty$? The answer is it does not always converge to 0. This is the reason why we see runge phenomona appear arround the borders. A simple way to avoid this is using Chebyshev's abciss system.

B.1.3 About Hermite's interpolation

Definition B.1.2. *Let $n \geq 0$ and suppose that x_i are real and distinct numbers. Then given two sets y_i and z_i, we can build Hermite's polynomial as follows:*

$$p_{2n+1}(x) = \sum_{k=0}^{n} H_k(x)y_k + K_k(x)z_k \tag{B.11}$$

where

- $H_k(x) = (L_k(x))^2(1 - 2L_k'(x_k)(x - x_k))$
- $K_k(x) = (L_k(x))^2(x - x_k)$

and with

$$H_k(x_i) = \begin{cases} 1 & i = k \\ 0 & i \neq k \end{cases} \qquad H_k'(x_i) = 0$$

$$K_k(x_i) = 0 \qquad K_k'(x_i) \begin{cases} 1 & i = k \\ 0 & i \neq k \end{cases}$$

Hermite's interpolation satisfies:

$$p_{2n+1}(x_i) = f(x_i) \qquad p_{2n+1}'(x_i) = f'(x_i)$$

Theorem B.1.5. *Let $n \geq 0$ and suppose that x_i are real and distinct numbers. Then given two sets y_i and z_i there exists a unique polynome $p_{2n+1}(x) \in \mathcal{P}_{2n+1}$ such that*

$$p_{2n+1}(x_i) = y_i \qquad p_{2n+1}'(x_i) = z_i$$

The idea of the proof is to construct the auxilliary polynomials H_k and K_k and show it exists (it fits the definition of an interpolation) and the proof of uniqueness is the same as proof of uniqueness of Lagrange.

Proof. **Existance:** Let us begin by supposing that $n \geq 1$. As in the case of Lagrange interpolation, we construct a set of auxiliary polynomials defined by

- $H_k(x) = (L_k(x))^2(1 - 2L'_k(x_k)(x - x_k))$

- $K_k(x) = (L_k(x))^2(x - x_k)$

where $L_k(x) = \prod_{i=0, i\neq k}^{n} \frac{(x-x_i)}{(x_k-x_i)}$. Clearly H_k and K_k are of degree $2n+1$. It is trivial to see that $H_k(x_i) = K_k(x_i) = 0$ and $H'_k(x_i) = K'_k(x_i) = 0$ whenever $i, k \in \{0, 1, \ldots, n\}$ and $i \neq k$

$$H_k(x_i) = \begin{cases} 1 & i = k \\ 0 & i \neq k \end{cases} \qquad H'_k(x_i) = 0$$

$$K_k(x_i) = 0 \qquad K'_k(x_i) \begin{cases} 1 & i = k \\ 0 & i \neq k \end{cases}$$

We deduce that

$$p_{2n+1}(x) = \sum_{k=0}^{n} H_k(x)y_k + K_k(x)z_k$$

satisfies the required condition and $p_{2n+1} \in \mathcal{P}_{2n+1}$

Uniqueness Suppose p_{2n+1} is not unique. $\exists q_{2n+1} \in \mathcal{P}_{2n+1}$ with $p_{2n+1} \neq q_{2n+1}$ such that $q_{2n+1}(x_i) = y_i$. Then $p_{2n+1} - q_{2n+1} \in \mathcal{P}_{2n+1}$ has $2n+2$ distinct roots x_i (twice, one for function and the secoind for derivates). Since a polynomial of degree $2n+1$ cannot have more than $2n+1$ roots unless it's identically 0, it follows that $p_{2n+1}(x) = q_{2n+1}(x)$ thus showing uniqueness □

B.1.4 Differentiation

From the Lagrange interpolsation polynomial $p_n(x) = \sum_{k=0}^{n} L_k(x)f(x_k)$, the polynomial $p'_n(x)$ is given by

$$p'_n(x) = \sum_{k=0}^{n} L'_k(x)f(x_k)$$

The degree of this polynomial is clearly $n - 1$.

B.2 $\infty-$norm

Definition B.2.1. *Suppose ν is a linear space over the field $\mathbb{R}$ of real numbers. A non negative function $||.||$ defined on ν whose value at $f \in \nu$ is denoted by $||f||$ is called a norm on ν if it satisfies the following axioms:*

- $||f|| = 0$ *if an only if* $f = 0$ *in* ν
- $||\lambda \cdot f|| = |\lambda| \cdot ||f|| \forall \lambda \in \mathbb{R}$ *and* $\forall f \in \nu$

- $||f+g|| \leq ||f|| + ||g|| \forall f, g \in \nu$ *(triangular inequality)*

Lemma B.2.1. *1 Suppose that the real function w is defined continuous positive and integrable on the interval (a, b). Then for any function $f \in \mathcal{C}[a, b]$,*

$$||f||_2 \leq W||f||_\infty \tag{B.12}$$

where $W = \left(\int_a^b w(x)dx \right)^{\frac{1}{2}}$

2 Given two positive numbers ϵ (however small) and M (however large), $\exists f \mathcal{C}[a, b]$ such that

$$||f||_2 \leq \epsilon \qquad\qquad ||f||_\infty \geq M \tag{B.13}$$

Theorem B.2.2. ***Weierstrass Approximation Theorem*** *Suppose that f is a real valued function defined and continuous on a bounded closed interval $\Omega = [a, b]$ of the real line. Then given any $\epsilon > 0, \exists$ a polynomial p such that*

$$||f - p||_\infty \leq \epsilon \tag{B.14}$$

This is an important theorem in classical analysis, and several proofs are known. It is evidently sufficient to consider $[0, 1]$; a simple change of variable will then extend the proof to any bounded closed interval $[a, b]$. For real-valued functions f defined and continuous on $[0, 1]$ Bernstein's proof uses the polynomial

$$p_n(x) = \sum_{k=0}^{n} p_{nk}(x) f(\frac{k}{n})$$

where the Bernstein polynomials are defined by: $p_{nk} = C_k^n x^k (1-x)^{n-k}$ It can be shown that for any $\epsilon > 0, \exists n = n(\epsilon)$ such that $||f - p_n||_\infty < \epsilon$.

According to the Weierstrass Approximation Theorem any function $f \in \mathcal{C}[a, b]$ can be approximated arbitrarily well from the set of all polynomials. Clearly if instead of the set of all polynomials we restrict ourselves to $\mathcal{P}_n$ the theorem is no longer true. The following theorem establishes the existence of a best approximation polynomial $p_n(x)$ of degree n to the function f in the $\infty-$norm.

Theorem B.2.3. *Given that $f \in \mathcal{C}[a, b], \exists p_n \in \mathcal{P}_n$ such that*

$$E(c_0, \ldots, c_n) = ||f - p_n||_\infty = \min_{q \in \mathcal{P}_n} ||f - q||_\infty \tag{B.15}$$

where $c_0, \ldots, c_n$ are the coefficients of $q_n(x) = c_0 + c_1 x + \ldots + c_n x^n$

The idea of the proof is first to show that E is continuous. Then by showing that a certain element is optimal.

Proof. **Continuity** To show that E is continuous at each point $(c_0, \ldots, c_n) \in \mathbb{R}^{n+1}$, consider any other point $(d_0, \ldots, d_n) \in \mathbb{R}^{n+1}$ and define the polynomial $eta_n(x) = d_0 + d_1 x + \ldots + d_n x^n$. We see from the triangular inequality that:

$$\begin{aligned} E(c_0 + d_0, \ldots, c_n + d_n) &= ||f - (q_n + \eta_n)||_\infty \\ &\leq ||f - q_n||_\infty + ||\eta_n||_\infty \\ &\leq E(c_0, \ldots, c_n) + ||\eta_n||_\infty \end{aligned}$$

Now given a positive number ϵ, choose $\delta = \epsilon/(1 + \ldots, K^n)$ where $K = \max |a|, |b|$. Consider any $(d_0, \ldots, d_n) \in \mathbb{R}^{n+1}$ such that $|d_i| \leq \delta$. Then:

$$\begin{aligned} E(c_0 + d_0, \ldots, c_n + d_n) - E(c_0, \ldots, c_n) &\leq ||\eta_n||_\infty \\ &\leq \max_{x \in [a,b]} (|d_0| + |d_1 x| + \ldots + |d_n x^n|) \\ &\leq \delta(1 + \ldots + K^n) \\ &\leq \epsilon \end{aligned}$$

Similarly:

$$\begin{aligned} E(c_0, \ldots, c_n) &= ||f - (q_n - \eta_n) + \eta_n||_\infty \\ &\leq ||f - (q_n + \eta_n)||_\infty + ||\eta_n||_\infty \\ &\leq E(c_0 + d_0 + \ldots + c_n + d_n) + \epsilon \end{aligned}$$

Therefore $|E(c_0 + d_0, \ldots, c_n + d_n) - E(c_0, \ldots, c_n)| \leq \epsilon$ by the two equations. Since $(c_0, \ldots, c_n)$ is an arbitrary point in $\mathbb{R}^{n+1}$, it follows that E is continuous on $\mathbb{R}^{n+1}$

Existence Let us denote by S the set of all points $(c_0, \ldots, c_n) \in \mathbb{R}^{n+1}$ such that $E(c_0, \ldots, c_n) \leq ||f||_\infty + 1$. The set S is evidently bounded and closed on $\mathbb{R}^{n+1}$; furthermore, $S \neq \emptyset$ since $E(0, \ldots, 0) = ||f||_\infty \leq ||f||_\infty + 1$ so that $(0, \ldots, 0) \in S$. Hence the continuous function E attains it's lower bound over the set S; let us denote this lower bound by d and let $(c_0^*, \ldots, c_n^*)$ denote that point in S where it is attained. Since $(0, \ldots, 0) \in S$ it follows that:

$$d = \min_{(c_0, \ldots, c_n) \in S} E(c_0, \ldots, c_n) \leq E(0, \ldots, 0) = ||f||_\infty$$

According to the definition of S

$$E(c_0, \ldots, c_n) > ||f||_\infty + 1 \forall (c_0, \ldots, c_n) \in \mathbb{R}^{n+1}/S$$

Hence if $(c_0, \ldots, c_n) \notin S$ then $E(c_0, \ldots, c_n) > d + 1$. Thus the lower bound d of the function E over the set S is the sale as the lower bound E over all of $\mathbb{R}^{n+1}$. Therefore the lower bound is attained at a point $(c_0^*, \ldots, c_n^*) \in S$ letting $p_n^*(x) = c_0^* + \ldots + c_n^* x^n$ we find $d = ||f - p_n^*||_\infty$. p_n^* is the polynomial of best approximation. $\square$

Definition B.2.2. ***Minimax Polynomial:*** *The polynomial of best approximation is often referred to as the minimax polynomial.*

Theorem B.2.4. ***De La Vallée Poussin*** *Let $f \in \mathcal{C}[a,b]$ and $r \in \mathcal{P}_n$. Suppose $\exists n+2$ points $x_0 < \ldots < x_{n+1}$ in the interval $[a,b]$ such that $f(x_i) - r(x_i)$ and $f(x_{i+1}) - r(x_{i+1})$ have opposite signs for $i = 0, \ldots, n+1$. Then:*

$$\min_{q \in \mathcal{P}_n} ||f - q||_\infty \geq \min_{i=0,\ldots,n+1} |f(x_i) - r(x_i)| \tag{B.16}$$

The idea of the proof is by the absurd. Suppose the statement is false.

Proof. Let us denote the right hand side of the last equation by μ. Clearly $\mu > 0$; when $\mu = 0$ the statement is trivial. Suppose equation is false; then for a minimax polynomial approximation of the function f we have:

$$||f - p_n||_\infty = \min_{q \in \mathcal{P}_n} ||f - q||_\infty < \mu \tag{B.17}$$

Therefore:

$$|p_n(x_i) - f(x_i)| < |r(x_i) - f(x_i)| \tag{B.18}$$

Now

$$r(x_i) - p_n(x_i) = [r(x_i) - f(x_i)] - [p_n(x_i) - f(x_i)] \tag{B.19}$$

Since the first right term always exceeds the term in absolute value, it follows that $r(x_i) - p_n(x_i)$ and $p_n(x_i) - f(x_i)$ have the same signs for $i = 0, \ldots, n+1$. Hence $r - p_n$ which is a polynomial of degree at most n changes signs $n+1$ times. Which is a contradiction. □

Theorem B.2.5. ***Oscillation theorem*** *Suppose that $f \in \mathcal{C}[a,b]$. A polynomial $r \in \mathcal{P}_n$ is a minimax polynomial of degree n for the function f on $[a,b]$ if and only iff $\exists$ a sequence of $n+2$ points x_i such that $a \leq x_0 < \ldots < x_{n+1} \leq b$*

$$|f(x_i) - r(x_i)| = ||f - r||_\infty$$

and

$$f(x_i) - r(x_i) = -f(x_{i+1}) - r(x_{i+1}) \tag{B.20}$$

In other words, $f - r$ attains it's maximum absolute value with alternating signs at the points x_i which are referred to as critical points.

This theorem is an equivalence et needs to proven the both ways: Equi-oscillation ⇒ optimality and optimality ⇒ Equi-oscillation. The latter will be proven by contraposition. Meaning we will prove that non equi-oscillation ⇒ non optimality.

Proof. **Equi-oscillation ⇒ optimality** Let p do equioscillation at $x_0, \ldots, x_{n+1}$. Let's apply De La Vallée Poussin's theorem at thus points

$$\min_{q \in \mathcal{P}_n} ||f - q||_\infty \geq \min_i |f(x_i) - p(x_i)| = ||f - p||_\infty$$

i.e p is optimal so p is a solution.

Equi-oscillation $\Leftarrow$ optimality Suppose p doesn't equi-oscillate. Then $\exists \xi_1 > \xi_2 < \ldots < \xi_k \in [a,b]$ such that:

$$\begin{aligned} (f-p)(x) &\leq E - \delta \qquad \text{for} x \in [\xi_1, \xi_2] \cup [\xi_3, \xi 4] \cup \ldots \\ (f-p)(x) &\geq E + \delta \qquad \text{for} x \in [a, \xi_1] \cup [\xi_2, \xi 3] \cup \ldots \end{aligned}$$

Define $\Delta p(x) = (\xi_1 - x)(\xi_2 - x)\ldots(\xi_k - x) \in \mathcal{P}_n$ then $\exists \epsilon > 0$ sufficiently small such that

$$||f - (p + \epsilon \Delta p(x))||_\infty < ||f - p||_\infty \tag{B.21}$$

In other words $p(x) + \epsilon \Delta p(x)$ is feasible and has a strictly smaller value of the objective function. p is not optimal. □

Theorem B.2.6. *Suppose that $[a,b]$ is a bounded closed interval of the real line. Each $f \in [a,b]$ has a unique minimax polynomial $p_n \in \mathcal{P}_n$ on $[a,b]$*

The proof of this theorem is by the absurd. Suppose there exists another one. Show that a combination of the two $(p_n - q_n)$ is also a minimax polynomial and show that this polynomial cannot exist unless it equals 0 using the oscillation theorem.

Proof. Suppose that $q_n \in \mathcal{P}_n$ is also a minimax polynomial for f; p_n and q_n are distinct. Then:

$$||f - p_n||_\infty = ||f - q_n||_\infty = E_n(f)$$

where $E_n(f) = \min_{q \in \mathcal{P}_n} ||f - q||_\infty$. This implies by the triangular inequality that:

$$\begin{aligned} ||f - \frac{1}{2}(p_n + q_n)||_\infty &= ||\frac{1}{2}(f - p_n) + \frac{1}{2}(f - q_n)||_\infty \\ &\leq \frac{1}{2}||f - p_n||_\infty + \frac{1}{2}||f - q_n||_\infty = E_n(f) \end{aligned}$$

Therefore $\frac{1}{2}(p_n - q_n)$ is also a minimax polynomial $\in \mathcal{P}_n$ approximating f on $[a,b]$. By the oscillation theorem, $\exists$ a sequence of $n+2$ critical points x_i at which $|f(x_i) - \frac{1}{2}(p_n(x_i) + q_n(x_i))| = E_n(f)$. This is equivalent to $|f(x_i) - p_n(x_i)| + |f(x_i) - q_n(x_i))| = 2E_n(f)$. Now

$$|f(x_i) - p_n(x_i)| \leq \max_{x \in [a,b]} |f(x) - p_n(x)| = ||f - p_n||_\infty = E_n(f)$$

Same goes for $|f(x_i) - q_n(x_i)|$. It therefore follows that

$$f(x_i) - p_n(x_i) = f(x_i) - q_n(x_i)$$

Thus the difference $p_n - q_n$ vanishes at $n+2$ distinct points. As $p_n - q_n$ is a polynomial of at most degree n, the difference can only be 0. This contradicts the first hypothesis meaning the minimax polynomial is unique. □

The exchange algorithm is the algorithm that computes the minimax polynomial of degree n or less of a function $f \in \mathcal{C}[a,b]$.

Algorithm 1: *Finding the minimax plynomial of a function f*

Result: $p_n(x)^*$ the minimax interpolation polynomial for the function f
initialization:
Choose reference $R \in [a,b]$ of $n+2$ points $\{r_i\}$ with $i = 0, \ldots, n+1$;
Find degree $n+1$ polynomial $q(x)$ which interpolates f at R;
Find degree $n+1$ polynomial $s(x)$ which interpolates $\{(-1)^i\}_{i=0}^{m+1}$ on R;
Then $p(x) = q(x) - e_R s(k)$ where $e_k = \frac{\hat{q}}{\hat{s}}$ and where $\hat{q}, \hat{s}$ are the coefficients of highest powers for q and s;
Compute $||f - p_n(x)||_\infty > \epsilon$;
Determine a point x_e where $|E(x_e)| = |f(x_e) - p_n(x_e)| = ||E||_\infty = E_k$;
while $\underline{||f(x_e) - p_n(x_e)||^\smile \infty > \epsilon}$ **do**
    Exchange x_e for a point in R using one of 3 cases:;
    if $\underline{r_i < x_e < r_{i+1}}$ **then**
        if $\underline{\text{sign}(E(r_i))=\text{sign}(E(x_e)}$ **then**
            swap x_e for r_i ;
        else
            swap x_e for r_{i+1} ;
        end
    else if $\underline{x_e < r_1}$ **then**
        if $\underline{\text{sign}(E(r_1))=\text{sign}(E(x_e)}$ **then**
            swap x_e for r_1 ;
        else
            delete r_{n+2} and insert x_e instead;
        end
    else
        if $\underline{\text{sign}(E(r_{n+2}))=\text{sign}(E(x_e)}$ **then**
            swap x_e for r_{n+2} ;
        else
            delete r_0 and insert x_e instead;
        end
    end
    Find degree $n+1$ polynomial $q(x)$ which interpolates f at R;
    Find degree $n+1$ polynomial $s(x)$ which interpolates $\{(-1)^i\}_{i=0}^{m+1}$ on R;
    Then $p(x) = q(x) - e_R s(k)$ where $e_k = \frac{\hat{q}}{\hat{s}}$ and where $\hat{q}, \hat{s}$ are the coefficients of highest powers for q and s;
    Compute $||f - p_n(x)||^\smile \infty > \epsilon$with new polynomial;
end
Congratulations you've found p_n^*

Theorem B.2.7. *Suppose that $n \geq 0$. The polynomial $p_n \in \mathcal{P}_n$ defined by $p_n(x) =$*

$x^{n+1} - 2^{-n}T_{n+1}(x)$ *with* $x \in [-1,1]$ *is the minimax polynomial of degree* n *to the function* $x \longmapsto x^{n+1}$ *on* $[-1,1]$.

Proof. By the second property of the Chebyshev polynomials (see section 1), $p_n \in \mathcal{P}_n$. Since $x^{n+1} - p_n(x) = 2^{-n}T_{n+1}(x)$, by properties 5 and 6 of the Chebyshev polynomials, the difference does not exceed 2^{-n} on the interval $[-1,1]$ and attains this value with alternating sign at the $n+2$ points $x_k = \cos(k\pi/n)$. Therefore in virtue of the oscillation theorem, p_n is the unique minimax polynomial to the function f on $[-1,1]$. □

Theorem B.2.8. *Suppose that* $n \geq 0$. *Among all the monic polynomials of degree* $n+1$, *the polynomials* $2^{-n}T_{n+1}$ *and* $-2^{-n}T_{n+1}$ *have the smallest* $\infty-$*norm on the interval* $[\breve{}1, 1]$.

Proof. Let $\mathcal{P}_{n+1}$ denote the set of all monic polynomials of degree $n+1$. Any $r \in \mathcal{P}_{n+1}$ can be regarded as the difference between the function $x \longmapsto x^{n+1}$ and a polynomial of lower degree, i.e $r(x) = x^{n+1} - q(x)$ with $q(x) \in \mathcal{P}_n$. Hence by the previous theorem (not the one we are proving.)

$$\begin{aligned}\min_{r\in\mathcal{P}_{n+1}} ||r||_\infty &= \min_{q\in\mathcal{P}_n} ||x^{n+1} - q||_\infty \\ &= ||x^{n+1} - (x^{n+1} - 2^{-n}T_{n+1})||_\infty \\ &= ||2^{-n}T_{n+1}||_\infty\end{aligned}$$

The minimum is therefore achieved when $r \in \mathcal{P}_{n+1}$ is one of the monic polynomials $2^{-n}T_{n+1}$ or $-2^{-n}T_{n+1}$ □

We close the body of this subsection with another application of Chebyshev's polynomials: it concerns the "optimal" choice of interpolation points in the Lagrange interpolation. In Section 1 on polynomial interpolation, the error between an $n+1$ times continuously differentiable function defined on a closed interval $[a,b]$ of the real line, and it's Lagrange interpolation points $\xi_0, \ldots \xi_n$ was shown to have the form

$$f(x) - p_n(x) = \frac{f^{(n+1)}(\eta}{(n+1)!}\pi_{n+1}(x) \tag{B.22}$$

Where $\eta = \eta(x) \in]a,b]$ and $\pi_{n+1}(x) = (x-\xi_0)\ldots(x-\xi_n)$. Clearly $\pi_{n+1}(x)$ is a monic polynomial of degree $n+1$. In a practical application the values ξ_i and $f(\xi_i)$ might already be given. However, in a situation where $[a,b] = [-1,1]$, they should be taken as the zeros of the Chebyshev polynomial T_{n+1} for then π_{n+1} will have the smallest $\infty-$norm on the interval $[\breve{}1, 1]$ among all monic polynomials.

Theorem B.2.9. *Suppose that* f *is a real valued function defined and continuous on the closed real interval* $[a,b]$, *and such that the derivative of* f *of order* $n+1$ *is continuous on* $[a,b]$. *Let* $p_n \in \mathcal{P}_n$ *denote the Lagrange interpolation polynomial of* f *with interpolation points:*

$$\xi_i = \frac{(b-a)}{2}(b-a)\cos\left(\frac{(j+\frac{1}{2})\pi}{n+1}\right) + \frac{(b+a)}{2} \tag{B.23}$$

Then $||f - p_n||_\infty \leq \frac{(b-a)^{n+1}}{2^{2n+1}(n+1)!}M_{n+1}$. *Where* $M_{n+1} = \max_{\zeta\in[a,b]} |f^{(n+1)}(\zeta)|$

Proof. Let $\tau_j = \cos\left(\frac{(j+\frac{1}{2})\pi}{n+1}\right)$ denote the zeros of the polynomial $T_{n+1}(t)$ on $[-1,1]$. Hence

$$2^{-n}T_{n+1}(t) = \prod_{j=0}^{n}(t-\tau_j) \qquad\qquad t \in [-1,1] \tag{B.24}$$

Let us define the points ξ_j as the statement of the theorem. Clearly $\xi_j \in (a,b)$ is the image of $\tau_j \in (-1,1)$ under linear transformation $t \mapsto x = \frac{(b-a)}{2}t + \frac{(b+a)}{2}$. By transformation we obtain the required bound. □

B.3 2-norm

B.3.1 Inner product spaces

Let ν be a linear space over the field of real numbers. A real valued function $\langle\cdot|\cdot\rangle$ defined on the Cartesian product $\nu \times \nu$ is called an inner product on ν if it satisfies the following axioms:

- $\langle f+g|h\rangle = \langle f|h\rangle + \langle g|h\rangle \qquad \forall f,g,h \in \nu$
- $\langle \lambda f|g\rangle = \lambda\langle f|g\rangle \qquad \forall \lambda \in \mathbb{R} \text{ and } \forall f,g \in \nu$
- $\langle f|g\rangle = \langle g|f\rangle \qquad \forall f,g \in \nu$
- $\langle f|f\rangle \geq 0 \qquad \forall f \in \nu$

Definition B.3.1. *Suppose that ν is an inner product space, and that f, g are two elements of ν such that $\langle f|g\rangle = 0$; we shall then say that f is orthogonal to g.*

Definition B.3.2. *Suppose that ν is an inner product space over the field of real numbers, with inner product $\langle\cdot|\cdot\rangle$. For $f \in \nu$, we define the induced norm $||f|| = \left(\langle f|f\rangle\right)^{\frac{1}{2}}$*

Theorem B.3.1. ***Cauchy-Schwartz inequality***

$$|\langle f|g\rangle| \leq ||f|| \cdot ||g|| \qquad\qquad \forall f,g \in \nu \tag{B.25}$$

Proof. Recalling the definition of $||\cdot||$ from the first definition of this subsection and noting the first three acioms of inner product, we find that for $f,g \in \nu$:

$$0 \leq ||\lambda f + g||^2 = \lambda^2||f||^2 + 2\lambda\langle f|g\rangle + ||g||^2 \tag{B.26}$$

Denoting, for $f,g \in \nu$ fixed, the quadratic polynomial in λ on the right hand side by $A(\lambda)$ to be non negative $\forall\lambda \in \mathbb{R}$ is that using the discriminant: $(2\langle f|g\rangle)^2 - 4||f||^2||g||^2 \leq 0$; this gives us the inequality of Cauchy-Schwartz. □

B.3.2 Best approximation of the 2-norm

Definition B.3.3. *Let $\nu = [a, b]$ be an inner product space over the field of real numbers. Suppose $f, g \in \nu$. Suppose also a weight function $w(x)$ defined, continuous, positive and integrable on ν. We define the scalar product of f by g as:*

$$\langle f|g\rangle = \int_a^b w(x)f(x)g(x) \tag{B.27}$$

Definition B.3.4. *Following the previous definition, the induced norm over the inner space $\nu = [a, b]$ is defined by:*

$$||f||_2 = \Big(\int_a^b w(x)|f(x)|^2 \Big)^{\frac{1}{2}} \tag{B.28}$$

We denote by $L^2_w(a, b)$ the set of real valued function f defined on (a, b) such that $w(x)|f(x)|^2$ is integrable on (a, b).

Theorem B.3.2. *The problem of best approximation in the $2-$norm can be formulated as follows:*
Given that $f \in L^2_w(a, b)$ find $p_n \in \mathcal{P}_n$ such that:

$$||f - p_n||_2 = \inf_{q\in\mathcal{P}_n} ||f - q||_2$$

Such a polynomial is called the polynomial of best approximation of degree n to the function f in the $2-$norm over (a, b).

Definition B.3.5. *Given a weighted function w defined, positive, continuous and integrable on (a, b), we say the sequence of polynomials ϕ_j is a system of orthogonal polynomials on (a, b) with respect to w if each ϕ_j is of exact degree j and if*

$$\int_a^b w(x)\phi_k(x)\phi_j(x)dx \qquad \begin{cases} \neq 0 & j = k \\ = 0 & j \neq k \end{cases}$$

Now we show that the system of orthogonal polynomials exists on any interval (a, b). Let $\phi_0 \equiv 1$, and suppose that ϕ_j has already been constructed for $j = 0, \ldots, n \geq 0$. Then

$$\int_a^b w(x)\phi_k(x)\phi_j(x)dx = 0 \qquad k = \{0, \ldots, n\}/j$$

Let us now define the polynomial $q(x) = x^{n+1} - a_0\phi_0(x) + \ldots + a_n\phi_n(x)$

$$a_j = \frac{\int_a^b w(x)x^{n+1}\phi_j(x)dx}{\int_a^b w(x)(\phi_j(x)^2)dx} \tag{B.29}$$

It then follows that:

$$\int_a^b w(x)q(x)\phi_j(x)dx = \int_a^b x^{n+1}\phi_j(x)dx - a_j\int_a^b w(x)(\phi_j)^2dx = 0 \quad \forall j \text{such that} 0 \leq j \leq n \tag{B.30}$$

Where we have used the orthogonality of the sequence ϕ_j. This procedure is usually referred to as the Graham-Schmitt orthogonalization

Definition B.3.6. ***Graham-Schmitt*** *Let ψ_j be the sequence of vectors we wish to orthogonalize. We define ϕ_j, the set of ψ_j orthogonalized by the formula:*

$$\phi_n = \psi_n - \sum_{j=0}^{n-1} \frac{\langle \phi_j | \phi_n \rangle}{||\phi_j||^2} \phi_j$$

The same procedure can be done if we wish to orthonormalize them. The formula thus becomes:

$$\phi_n = \frac{\psi_n - \sum_{j=0}^{n-1} \langle \phi_j | \phi_n \rangle \phi_j}{||\psi_n - \sum_{j=0}^{n-1} \langle \phi_j | \phi_n \rangle \phi_j||}$$

Theorem B.3.3. *There is a unique system $(\phi_0, \ldots)$ of monic (the term of highest degree is with coefficient 1) orthogonal polynomials on (a, b) with respect to w. They are determined by the so called three term recurrence relation.*

$$\phi_{j+1}(x) = (x - \alpha_j)\phi_j(x) - \beta_j \phi_{j-1}(x) \tag{B.31}$$

with $\phi_0(x) = 1$ and $\phi_1(x) = (x - \alpha_0)\phi_0(x)$

$$\alpha_j = \frac{\langle \phi_j | x\phi_j}{||\phi_j||^2}$$
$$\beta_j = \frac{||\phi_j||^2}{||\phi_{j-1}||^2}$$

Proof. Proof is direct by graham Schmitt □

Definition B.3.7. ***Legendre Polynomials*** *We wish to construct a system of orthogonal polynomials on $(-1, 1)$ with respect to $w(x) \equiv 1$. On replacing $x \mapsto 2x - 1$leads to Legendre polynomials. The recurrence is:*

$$\phi_{n+1}(x) = \frac{2n+1}{n+1} x\phi_n(x) - \frac{n}{n+1}\phi_{n-1}(x) \tag{B.32}$$

With $\phi_0(x) = 1$ and $\phi_1(x) = x$. They have the property orthogonality, symmetry and Maximum norm (i.e $|\phi_n(x)| \leq 1$

Theorem B.3.4. ***Weierstrass Approximation Theorem*** *Suppose that f is a real valued function defined and continuous on a bounded closed interval $\Omega = [a, b]$ of the real line. Furthermore, suppose w is a real valued weight function, defined continuous, positive and integrable on Ω. Then given any $\epsilon > 0, \exists$ a ploynomial p such that*

$$||f - p||_2 = \left(\int_\Omega w(x)|f(x) - p(x)|^2 \right)^{\frac{1}{2}} \leq \epsilon \tag{B.33}$$

Theorem B.3.5. *Given that $f \in L^2_w(a, b), \exists$ a unique polynomial $p_n \in \mathcal{P}_n$ such that $||f - p_n||_2 = \min_{q \in \mathcal{P}_n} ||f - q||_2$*

The idea of the proof is to build a set of orthonormal polynomial that form the base of $\mathcal{P}_n$ and then construct a polynomial q_n using the base. Then find the coefficients β_i^* to ensure q minimizes the problem.

Proof. Suppose that ϕ_j is a system of orthogonal polynomials with respect to the weight function w on (a, b). Let us normalize ϕ_j by defining a new system of orthogonal polynomials

$$\psi_j(x) = \frac{\phi_j(x)}{||\phi_j||_2}$$

Now $\langle \phi_j | \phi_k \rangle = 1$ if $j = k$ and 0 otherwise. Such a system is said to be orthonormal. The polynomials ϕ_j are linearly independant and form a basis for the linear space $\mathcal{P}_n$. Therefore each element $q \in \mathcal{P}_n$ can be expressed as a suitable linear combination

$$q(x) = \beta_0\psi_0(x) + \ldots + \beta_n\psi_n(x)$$

We wish to choose the β_j in order to ensure that q minimises $||f - q||_2$ over all $q \in \mathcal{P}_n$. Let us define $E : (\beta_0, \ldots, \beta_n) \in \mathbb{R}^{n+1} \mapsto E(\beta_0, \ldots, \beta_n)$ defined by $E(\beta_0, \ldots, \beta_n) = ||f - q||_2^2$ Then:

$$\begin{aligned} E(\beta_0, \ldots, \beta_n) &= \langle f - q | f - q \rangle = \langle f | f \rangle - 2\langle f | q \rangle + \langle g | g \rangle \\ &= ||f||_2^2 - 2\sum_{j=0}^{n} \beta_j \langle f | \phi_h \rangle + \sum_{j=0}^{n} \sum_{k} = 0^n \beta_j \beta_k \langle \psi_k | \psi_j \rangle \\ &= ||f||_2^2 - 2\sum_{j=0}^{n} \beta_j \langle f | \phi_h \rangle + \sum_{j=0}^{n} \beta_j^2 \end{aligned}$$

The function $E(\beta_0, \ldots, \beta_n)$ achieves it's minimum value at $(\beta_0^*, \ldots, \beta_n^*)$

$$\beta_j^* = \langle f | \psi_j \rangle$$

hence $p_n \in \mathcal{P}_n, p_n(x) = \beta_0^*\psi_0(x) + \ldots + \beta_n^*\psi_n(x)$ is the unique polynomial □

Remark. *As $E(\beta_0^*, \ldots, \beta_n^*) = ||f - q||_2^2 \geq 0$ it follows the proof of the previous theorem that if $f \in L_w^2(a, n)$ and $\{\psi_0, \ldots\}$ is an orthogonal system of polynomials in $L_w^2(a, b)$, then*

$$\sum_{j=0}^{n} |\langle f | \psi_j \rangle|^2 \leq ||f||_2^2 \qquad \text{for each} n \geq 0 \tag{B.34}$$

This result is known as the Bessel inequality.

Theorem B.3.6. *A polynomial $p_n \in \mathcal{P}_n$ is the polynomial of best approximation of degree n to a function $f \in L_w^2(a, b)$ in the $2-$norm if and only if the difference $f - p_n$ is orthogonal to every element of $\mathcal{P}_n$*

$$\langle f - p_n | q \rangle = 0 \qquad \forall q \in \mathcal{P}_n$$

The idea of the proof orthogonal⇒ best approximation is to replace q in the previous equation by $p_n - q$ since it also belongs to $\mathcal{P}_n$. Then using Cauchy-Schwartz establish there is no better polynomial. The idea of the proof orthogonal⇐ best approximation is to start from the optimal polynomial $p_n(x) = \beta_0^* \psi_0(x) + \ldots$ and show that the scalar product between $f - p_n$ and the basis $\{\psi_j\}$ equals 0 using the properties of $p_n(x)$

Proof. **orthogonal⇒ best approximation** Suppose that $\langle f - p_n | q \rangle = 0$ holds. Then, given that $q - p_n \in \mathcal{P}_n \forall q \in \mathcal{P}_n$

$$\langle f - p_n | q - p_n \rangle = 0$$

$$\begin{aligned} ||f - p_n||^2 &= \langle f - p_n | f - p_n \rangle \\ &= \langle f - p_n | f - p_n \rangle + \langle f - p_n | q - p_n \rangle \\ &= \langle f - p_n | f - q \rangle + \langle f - p_n | q - p_n \rangle \\ &= \langle f - p_n | f - q \rangle \end{aligned}$$

Hence by Cauchy-Schwartz

$$||f - p_n||_2^2 \leq ||f - p_n||_2 ||f - q||_2 \qquad \forall q \in \mathcal{P}_n \tag{B.35}$$

On choosing $q = p_n$ on the right hand side the equality will hold therefore $||f - p_n||_2 = \min_{q \in \mathcal{P}_n} ||f - q||_2$

orthogonal⇐ best approximation Conversely, suppose that p_n is the polynomial of best approximation to $f \in L_w^2(a, b)$. With the previous theorem (not the one we are trying to prove), we have proof that $p_n(x) = \beta_0^* \psi_0(x) + \ldots + \beta - n^* \psi_n(x)$ where $\beta_k^* = \langle f | \psi_k \rangle$. On recalling thet $\langle \psi_k | \psi_j \rangle = \delta_{jk}$ ($\delta_{jk} = 1$ if $j = k$ and 0 otherwise) we deduce from $\beta_k^* = \langle f | \psi_k \rangle$ that:

$$\begin{aligned} \langle f - p_n | \psi_j \rangle &= \langle f | \psi_j \rangle - \sum_{k=0}^{n} \beta_k \langle \psi_k | \psi_j \rangle \\ &= \langle f | \psi_j \rangle - \sum_{k=0}^{n} \beta_k \delta_{jk} \\ &= \langle f | \psi_j \rangle - \beta_j^* = 0 \end{aligned}$$

Since $\mathcal{P}_n$= span$\{\psi_0, \ldots, \psi_n\}$ it follows this previous developement that $\langle f - p_n | q \rangle = 0 \forall q \in \mathcal{P}_n$ □

Theorem B.3.7. *Suppose that ϕ_j is a system of orthogonal polynomials on (a, b) with respect to the positive, continuous and integrable weight function $w(x)$ on (a, b). It is understood that ϕ_j is a polynomial of exact degree j. Then for $j \geq 1$, the zeris of the polynomial ϕ_j are real and distinct and lie in (a, b)*

Proof. Suppose $\xi_i (i = 1, \ldots, k)$ are the points in (a, b) where $\phi_j(x)$ changes signs. However w is positive on (a, b) so ϕ_j must change sign at least once on (a, b) therefore $k \geq 1$. Let us define:

$$\pi_k(x) = (x - \xi_1) \ldots (x - \xi_k)$$

Now the function $\phi_j(x)\pi_k(x)$ does not change sign in (a, b) since at each point where $\phi_j(x)$ changes sign so does $\pi_k(x)$. Hence

$$\int_a^b w(x)\phi_j\pi_k(x)dx \neq 0 \tag{B.36}$$

However ϕ_j is orthogonal to every polynomial of lower degree with respect to the weight function w, so the degree of π_k must be at least j, thus $k \geq j$. On the other hand, k cannot be greater than j since a polynimial of degree j cannot change signs more than j times. Therefore $k = j$ ie $\xi_i \in (a, b)$ are the zeros of ϕ_j □

Appendix C

Acquisition parameters

ICTEAM : ELEN pole LDRI : REMA – ADDB –BPBL CRL

Under the supervision of R.A. JOUDIOU Nicolas, , FNRS R.F. DES RIEUX Anne, FNRS R.F. RENSONNET Gaëtan, A.Pr. MUCCIOLI Giulio, FNRS S.R.A. A.Pr. JORDAN Bénédicte Post-D. R.F. TAQUET Maxime and Pr. MACQ Benoît

Last update date : January 22, 2020

Digital Laboratory Notebook – Myemouse Project

Ir. NIYIGABA ISHIMWE Alain

Preamble

This digital laboratory notebook aims to guarantee the traceability of the research results while recording the laboratory manipulations and settings in order to facilitate the in-house sharing and transfer. Moreover, any laboratory notebook is supposed to be confidential and therefore should not be disclosed to any person outside the research team.

Table of Contents

Table of Contents i
Project title 1
Mouse datasheet 1
Timeline 1
Setup 1
Pre-acquisition : . . . 1
Acquisition . . . 2
Remarks :
Post-acquisition . . . 5
Acquisitions 6
13/01/20 . . . 6
14/01/20 . . . 6
20/01/20 . . . 6
21/01/20 . . . 7
22/02/2020 – 23/02/2020 . . . 7
24/02/2020 . . . 7
29/02/2020 – 01/03/2020 . . . 7
02/03/2020 . . . 8
04/05/2020 . . . 8
05/05/2020 . . . 8
06/05/2020 . . . 8

Project title

In vivo quantification of myelin concentration in the brain from multi-modal MRI : longitudinal validation on a cuprizone mouse model of demyelination - second cohort -.

Mouse datasheet

- Denomination : C57BL/6JRj
- Type : inbred mouse (male)
- Source : Charles River
- Colour : black
- Number : 24 (6 healthy-controls – 18 cuprizone-fed)

Timeline

Semaine d'acquisition	Lundi	Mardi	Mercredi	Jeudi	Vendredi	Samedi	Dimanche	
-1			1	2	3	4	5	Janvier
0	6	7	8	9	10	11	12	
1	13	14	15	16	17	18	19	
2	20	21	22	23	24	25	26	
3	27	28	29	30	31	1	2	Février
4	3	4	5	6	7	8	9	
5	10	11	12	13	14	15	16	
6	17	18	19	20	21	22	23	
7	24	25	26	27	28	29	1	Mars
8	2	3	4	5	6	7	8	
9	9	10	11	12	13	14	15	
10	16	17	18	19	20	21	22	
11	23	24	25	26	27	28	29	
12	30	31	1	2	3	4	5	Avril
13	6	7	8	9	10	11	12	
14	13	14	15	16	17	18	19	
15	20	21	22	23	24	25	26	
16	27	28	29	30				

Code couleur
Jour d'arrivée des souris
Control Group
Cuprizone 6 weeks
Cuprizone 12 weeks
Cuprizone 6 weeks - Recovery 6 weeks

	1	2	3	4	5	6	7	8	9	10	11	12	13	14
Ctl	Control Diet													
Cpz6	Cuprizone Diet													
Cpz12							Cuprizone Diet							
Cpz6-Rcv6							Cuprizone Diet						Control Diet	

Setup

Pre-acquisition :

- Temperature regulation : preparation of the thermal blanket (heated up by a water bath) to keep the mouse at a temperature of 37°C.
- Anaesthesia regulation : injection of isoflurane (IsoFlo®) vapour (100% -+ 250 ml) via pressurized air (1 L/min)
  - to put the mouse to sleep (at 2.5%vol) ;
  - to keep the mouse asleep (about 1%vol).
- Respiration and temperature monitoring :
  i) Hardware : pressure detector (respiration) and anal probe (temperature).
  ii) Software : Small Animal Instruments Incorporated (SAM PC Monitor)
    * respiration between 60 and 120 breaths/min (ideally about 90 breaths/min) ;
    * temperature about 37°C (±0.5°C).

- MRI setting of 25 mm coil using PV6.0.1 software (Bruker®)

  i) Study registration :

  * Information filling :
    · Animal ID : Cuprizone_experiment_2019
    · Animal Name : Cuprizone_experiment_2019
    · Specimen : Rodent
    · Study Name : Groupe_X_souris_Y_D
      X ≡ group number
      Y ≡ mouse number
      D ≡ date in format "year-month-day" (e.g. 200113)
    · Operator : nmrsu
    · Location : Niyigaba_Ishimwe_Alain/Head/Diffusion_2/01_Localizer
    · Postion : HEAD_PRONE
  * Information selection :
    · RF : RAPID VHQ 177 (RAPID VHQ 177/01)
    · Gradient : BFG9S N.C.2 GRAD SYSTEM FOR BC70/16US-47/16 US (RRI 010467/4020)
    · Shim : BFG 9S FOR BC70/16-47/16 (RRI 010467/4020)
    · Adjustment : MRI Default

  ii) Wobble Adj. : tuning of the coil so that it matches the electronic components (impedance matching).

Acquisition

- Localizer [19s] : allow to have a quick overview of the mouse position in the 3 plans (axial, sagittal and coronal).
  - Flip Angle : 30°
    ⚠additional "Localizer" might be necessary in order to accurately position the coronal acquisition region with respect to the mice brain ; nevertheless, each time prior launching the acquisition the "study shim" and the "basic frequency" must be recomputed.

- T2_coronal [40s] : T2-weighted acquisition in the coronal plan to help positioning the sagittal slices.
  - Echo Time : 30 ms
  - Repetition Time : 2500 ms
  - Averages : 1
  - Repetitions : 1
  - Echo Spacing : 10 ms
  - Rare Factor : 8
  - Fat Suppression : ON
  - Trigger : ON
  - Slices : 10
  - Slice Orientation : Coronal
  - Read Orientation : Ro-Cd
  - Slice Thickness : 1 mm
  - Image Size : 128 × 128
  - Field of View : 20 × 20 mm
  - Read Offset : 0 mm
  - Phase Offset : 0 mm

  - Slices Gap Mode : Contiguous

- T2_sagittal [1m20s] : first T2-weighted acquisition in the sagittal plan to help positioning the anatomical reference acquisition with respect to the T2_coronal acquisition.

  - Echo Time : 30 ms
  - Repetition Time : 2500 ms
  - Averages : 2
  - Repetitions : 1
  - Echo Spacing : 10 ms
  - Rare Factor : 8
  - Fat Suppression : ON
  - Trigger : ON
  - FOV Saturation : ON
  - Slices : 20
  - Slice Orientation : Sagittal
  - Read Orientation : V-D
  - Slice Thickness : 0.5 mm
  - Image Size : 128×128
  - Field of View : 20×20 mm
  - Read Offset : 0 mm
  - Phase Offset : 0 mm
  - Slices Gap Mode : Contiguous

- T2_anat_ref [2m05s] : second T2-weighted acquisition in the sagittal plan that is used as the anatomical reference acquisition in order to determine/visualize the region of interest. Most of its parameters are identical to the T2_sagittal acquisition excepted

  - Slices : 10
  - Slice Thickness : 1 mm
  - Image Size : 200×200

- T2map_MSME [16m40s] : T2 multi-echo acquisition. Its geometrical parameters are identical to the T2_anat_ref acquisition and expected the subsequent parameters, the remaining are default Bruker parameters.

  - Echo Spacing : 6.689 ms
  - Repetition Time : 2500 ms
  - Averages : 2
  - Echo Averages : 1
  - Echo Images : 30

  ⚠Prior to launch any diffusion acquisition, the B0 Map must be computed.

- DtiEpi_reverse_baseline [40s] : diffusion acquisition with $b = 0\,s/mm^2$ and a negative phase encoding direction. As for the T2map_MSME the geometry and default Bruker parameters do not vary, excepted

  - Echo Time : 23.72 ms
  - Repetition Time : 2500 ms
  - Averages : 1
  - Repetitions : 1
  - Segments : 4
  - Preparation : SpinEcho
  - Gradient Duration : 3.5 ms
  - Gradient Separation : 12 ms
  - Experiment : DW_Contrast
  - Diffusion Directions : 1 (i.e. 1 – 0 – 0)
  - Exp. per Direction : 1
  - A0 Images : 3

- Dummy Duration : 20000 ms
- Fat Suppression : ON
- FOV Saturation : ON
- Trigger : ON
- Navigator : ON
- Requested Shim : Map-Shim
- Shim up to : Allshims
- Automatic Volume Margin : $1 \times 1 \times 1$ mm
- Shape of Shim Volume : Cuboid

- DtiEpi_baseline [40s] : diffusion acquisition with $b = 0\,s/mm^2$ and a positive phase encoding direction. Its parameters are identical to those of the DtiEpi_reverse_baseline acquisition.

- DtiEpi_bξ [5m50s] : diffusion acquisitions with $b = \xi\,s/mm^2$ and a positive phase encoding direction, where $\xi \in \{700, 1500, 2000, 2500\}$. For the two lowest b-values (i.e. 700 and 1500 s/mm^2), the images are acquired in 32 different directions ; whereas for the higher b-values (i.e. 2000 and 2500 s/mm^2), they are acquired in 64 directions. Furthermore, each direction is repeat twice and grouped consecutively, in order to generate acquisition redundancy. Subsequently, each enlarged set (i.e. $32 \rightarrow 64$ and $64 \rightarrow 128$) is grouped per 32 directions and per individual b-value, and acquired with 3 A0 images (to ease regristration post-processing) ; such that 12 DtiEpi_bξ are finally acquired.

Remarks :

1. The acquisition slices are always positioned such that they encompass the entire mouse brain. Furthermore, the coronal slices stack is set such that its utmost right edge is just next to the top of the brain.

2. When Triger "ON" $\Rightarrow$ gating parameters (Gating Setup Form) of the monitoring software must be filled :

   - ECG – Gates : OFF
   - E-Resp (tm) – Pulse Invert : ON
   - Respiration – Pulse Invert : ON – Begin Delay : 100 – Gates : ON

3. After positioning correctly the T2_sagittal acquisition, its *Slice Orientation* and *Geometry* is copied to the remaining acquisitions.

4. The *Phase* and *Read Offset* are forced to 0, to avoid artefacts.

5. Two FOV Sat (Field Of View Saturation) bands are positioned respectively on the mouse rostro-caudal axe such that they are adjacent to the acquisition slices : i.e.

   Sat Slice : 1
   - Slice Orientation : Axial
   - Slice Thickness : 8.5 mm
   - Slice Offset : -15 mm

   Sat Slice : 2
   - Slice Orientation : Axial
   - Slice Thickness : 8.5 mm
   - Slice Offset : 15 mm

6. The *Echo Spacing* of the T2map_MSME and the *Echo Time* of the diffusion acquisitions are minimum values that are automatically computed by Bruker Software.

7. In order to obtain a negative phase encoding direction, the Bruker DtiEpi method was modified : the *ACQ_scaling_phase* parameter was changed from 1 to -1 in the *BaseLevelRelation.c* file.

8. The DtiEpi_reverse_baseline acquisition together with the DtiEpi_baseline are used to correct from *susceptibility and eddy currents induced distortions* and only necessitate A0 images, hence why there is only one *Diffusion Directions*.

9. Theoretically, the total acquisition time is equal to 1h32m24s ($= 19s + 40s + 1m20s + 2m05s + 16m40s + 40s + 40s + (2 \times 2 + 4 \times 2) \times 5m50s$), but in practice, as the acquisition is performed only when the mouse respiration is stable (due to *Trigger* on), this time can reach up to 2h30m.

Post-acquisition

- Mouse tagging : on the first day of acquisition, ear(s) of the mouse are punched following a specific stamping pattern (FIGURE 1) in order to recognise them.

TABLE 1. **Mice labelling and numbering.**

Group	Label	Mice number					
1	Ctl	01	02	03	04	05	06
2	Cpz6	11	12	13	14	15	16
3	Cpz12	21	22	23	24	25	26
4	Cpz6-Rcv6	31	32	33	34	35	36

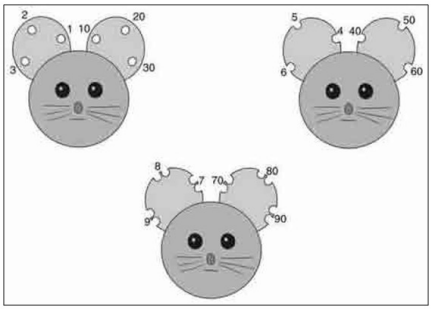

FIGURE 1. **Mouse tagging convention.**

- Weighing : after each acquisition, the mice are weighed in order to keep track of their weight over the experiment.

⚠This overall setup is used for all the subsequent acquisitions and therefore is not repeated each time, but remarks are made in case of any change.

Acquisitions

13/01/20

General information

- First day of acquisition of Group 1 mice (Ctl).
- Weighing :
  - mouse 01 : 23.8 g (about 10h58)
  - mouse 02 : 24.5 g (about 13h43)
  - mouse 03 : 23.5 g (about 16h15)
  - mouse 04 : 24.9 g (about 19h00)
  - mouse 05 : 24.2 g (about 21h48)
  - mouse 06 : 23.6 g (about 00h38)

Remarks

- The phase offset was no put at zero on each diffusion acquisition. Therefore, an additional DtiEpi_reverse_baseline acquisition was performed with an opposite phase offset.
- For each mouse, some blood was noticed on the temperature probe after remove of the latter from the anus (maybe due to a deep penetration, movement during the acquisition or not enough lubrication).

14/01/20

General information

- Acquisitions prior cuprizone feeding of Group 2 mice (Cpz6).
- Weighing :
  - mouse 11 : 23.3 g (about 04h01)
  - mouse 12 : 25.4 g (about 06h40)
  - mouse 13 : 27.2 g (about 09h12)
  - mouse 14 : 24.1 g (about 11h50)
  - mouse 15 : 25.6 g (about 14h14)
  - mouse 16 : 26.2 g (about 16h46)

Remarks

- Study Name mismatches : for all the acquisitions on that day, the date (year-month-day) should be "200114" instead of "200113" (e.g. Groupe_2_souris_11_200114).

20/01/20

General information

- Acquisitions prior cuprizone feeding of Group 3 mice (Cpz12).
- Weighing :
  - mouse 21 : 23.4 g (about 11h24)
  - mouse 22 : 24.6 g (about 13h59)
  - mouse 23 : 25.9 g (about 16h35)
  - mouse 24 : 23.8 g (about 19h06)
  - mouse 25 : 24.5 g (about 21h50)
  - mouse 26 : 24.8 g (about 00h19)

Remarks

- Mouse 21 – Tagging mistake : the left ear was mistaken with the right ear, such that its tagging became "12" instead of "21". In order, to differentiate it with the mouse 12, it was tagged again on the correct ears, such that in the end it has 4 holes (tag "12" and "21").
- Mouse 22 – Rectal bleeding on temperature probe (cfr comment of 13/01/20).

21/01/20

General information

- Acquisitions prior cuprizone feeding of Group 4 mice (Cpz6-Rcv6).
- Weighing :
  - mouse 31 : 26.9 g (about 03h33)
  - mouse 32 : 23.1 g (about 05h55)
  - mouse 33 : 26.6 g (about 08h16)
  - mouse 34 : 24.0 g (about 10h42)
  - mouse 35 : 25.8 g (about 13h05)
  - mouse 36 : 26.7 g (about 15h30)

Remarks

- Mouse 32 – Rectal bleeding on temperature probe (cfr comment of 13/01/20) & Small bleeding on the left ear after tagging.
- Mouse 36 – Rectal bleeding on temperature probe (cfr comment of 13/01/20).

22/02/2020 – 23/02/2020

General information

- Acquisitions of Group 1 mice (Ctl) after 6 weeks of normal diet. The first two and the last four mice were respectively imaged on the 22 and the 23.
- Weighing :
  - mouse 01 : 28.5 g (about 14h23)
  - mouse 02 : 28.4 g (about 16h54)
  - mouse 03 : 26.9 g (about 13h18)
  - mouse 04 : 28.0 g (about 15h43)
  - mouse 05 : 28.3 g (about 18h14)
  - mouse 06 : 28.0 g (about 20h35)

24/02/2020

General information

- Acquisitions of Group 2 mice (Cpz6) after 6 weeks of cuprizone diet.
- Weighing :
  - mouse 11 : 23.5 g (about 10h26)
  - mouse 12 : 25.9 g (about 12h44)
  - mouse 13 : 26.5 g (about 15h05)
  - mouse 14 : 24.4 g (about 17h25)
  - mouse 15 : 25.5 g (about 20h30)
  - mouse 16 : 26.3 g (about 22h50)

29/02/2020 – 01/03/2020

General information

- Acquisitions of Group 3 mice (Cpz12) after 6 weeks of cuprizone diet. The first two and the last four mice were respectively imaged on the 01 March and the 29 February.
- Weighing :
  - mouse 21 : 23.5 g (about 20h28)
  - mouse 22 : 23.5 g (about 17h50)
  - mouse 23 : 23.5 g (about 20h50)
  - mouse 24 : 24.1 g (about 18h23)
  - mouse 25 : 24.0 g (about 16h10)
  - mouse 26 : 22.6 g (about 13h40)

Remarks

- Study Name mismatches : for all the acquisitions performed on the 29 February, the date (year-month-day) should be "200229" instead of "200129" (e.g. Groupe_3_souris_26_200229).

02/03/2020

General information

- Acquisitions of Group 4 mice (Cpz6-Rcv6) after 6 weeks of cuprizone diet.
- Weighing :
  - mouse 31 : 25.9 g (about 19h20)
  - mouse 32 : 22.6 g (about 12h35)
  - mouse 33 : 24.5 g (about 17h05)
  - mouse 34 : 21.3 g (about 14h50)
  - mouse 35 : 23.9 g (about 10h20)
  - mouse 36 : 23.3 g (about 21h30)

Remarks

- ...

—

04/05/2020

General information

- Acquisitions of Group 3 mice (Cpz12) after 15 weeks of cuprizone diet.
- Weighing :
  - mouse 21 : 25.2 g (about 9h50)
  - mouse 25 : 26.8 g (about 12h10)
  - mouse 22 : 26.4 g (about 16h00)
  - mouse 23 : (not imaged)
  - mouse 24 : (not imaged)
  - mouse 26 : (not imaged)

Remarks

- due to an error in the tagging mouse 21 was first wrongly identified as 22. Since, there is a mouse 22 and a mouse 22true. 22 corresponding to the 21

05/05/2020

General information

- Acquisitions of Group 4 mice (Cpz6-Rcv6) at weeks 15.
- Weighing :
  - mouse 36 : 30.8 g (about 9h30)
  - mouse 34 : 29.2 g (about 12h00)
  - mouse 35 : g (about 14h15)
  - mouse 33 : 30.3 (not imaged)
  - mouse 32 : 29.1 (not imaged)
  - mouse 31 : 32.4 (not imaged)

Remarks

- ...

06/05/2020

General information

- Acquisitions of Group 1 mice control at weeks 15.
- Weighing :

- mouse 05 : 31.5 g (about 9h30)
- mouse 06 : 29.3 g (about 11h45)
- mouse 03 : 28.8g (about 14h15)
- mouse 01 : 28.6 (not imaged)
- mouse 02 : 29.7 (not imaged)
- mouse 04 : 30.8 (not imaged)

Remarks

- ...

Appendix D

Miscellaneous results

D.1 Cingulum Analysis results

The full extend of the Analysis can be found below. Jointly (respectfully left to right) the four groups with and without cingulum. All the following graphs are the RGB intensities [255,255,255] as a function of the pixels.

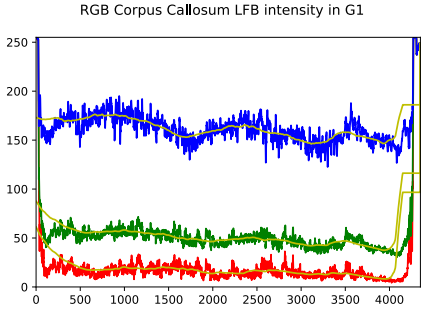

Figure D.1: *RGB analysis on group 1 mice with cingulum*

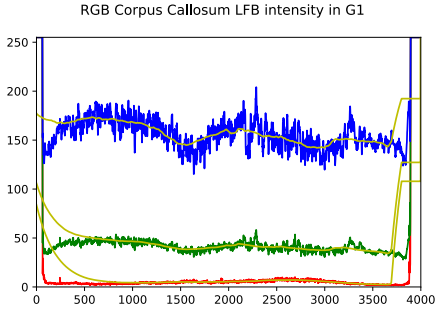

Figure D.2: *RGB analysis on group 1 mice without cingulum*

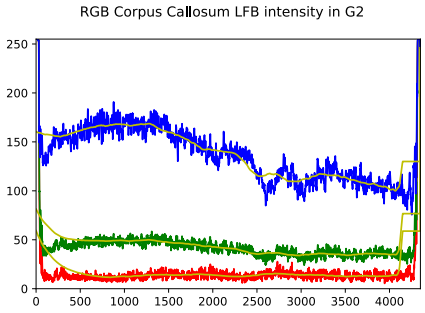

Figure D.3: *RGB analysis on group 2 mice with cingulum*

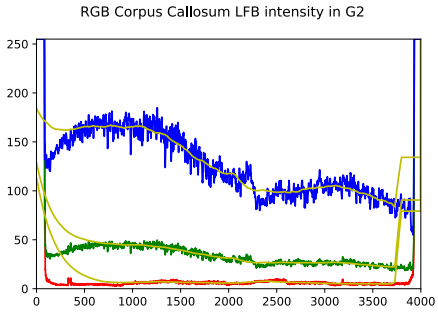

Figure D.4: *RGB analysis on group 2 mice without cingulum*

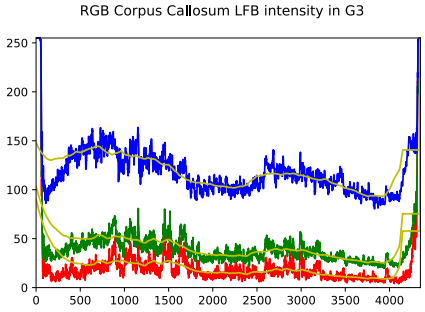

Figure D.5: *RGB analysis on group 3 mice with cingulum*

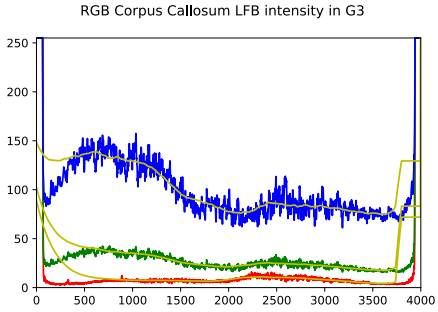

Figure D.6: *RGB analysis on group 3 mice without cingulum*

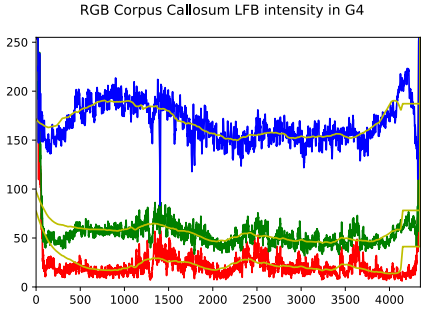

Figure D.7: *RGB analysis on group 4 mice with cingulum*

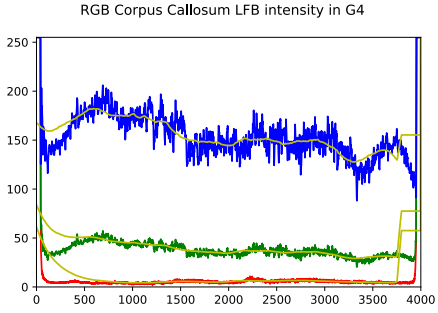

Figure D.8: *RGB analysis on group 4 mice without cingulum*

Along with the group comparison, we can also plot the difference between groups, i.e the intensity difference which would correlate to a myelin intensity difference between groups.

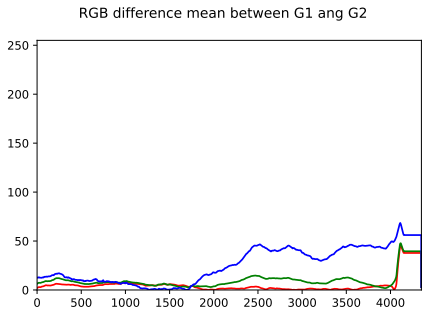

Figure D.9: *RGB intensity difference between group 1 and group 2 with cingulum*

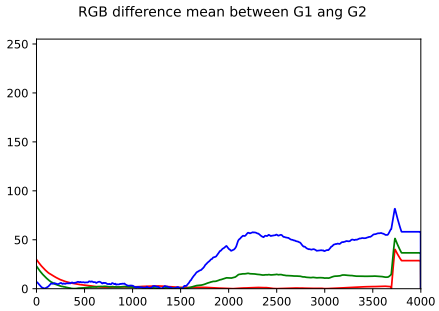

Figure D.10: *RGB intensity difference between group 1 and group 2 without cingulum*

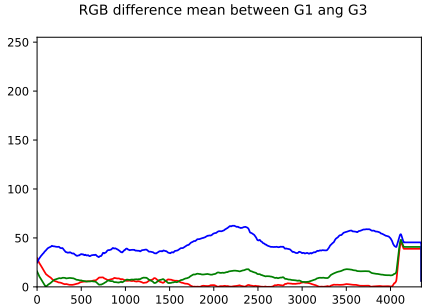

Figure D.11: *RGB intensity difference between group 1 and group 3 with cingulum*

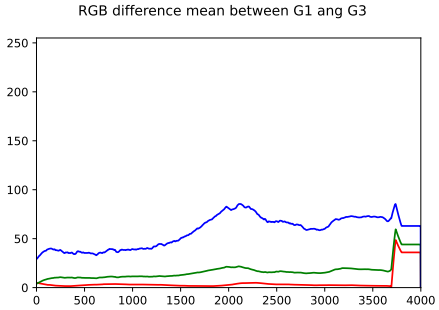

Figure D.12: *RGB intensity difference between group 1 and group 3 without cingulum*

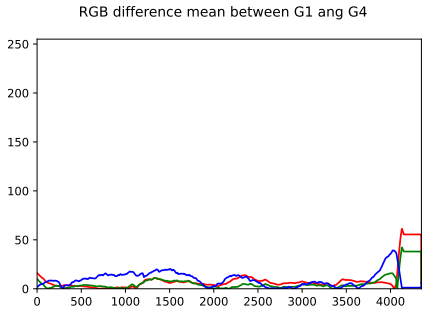

Figure D.13: *RGB intensity difference between group 1 and group 4 with cingulum*

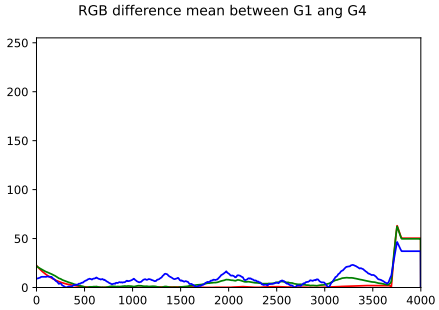

Figure D.14: *RGB intensity difference between group 1 and group 4 without cingulum*

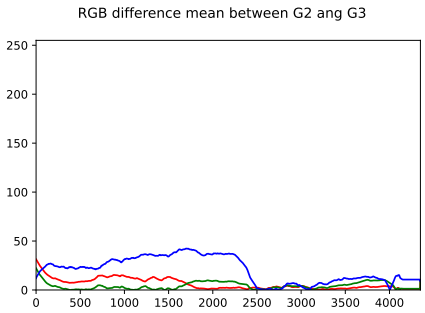

Figure D.15: *RGB intensity difference between group 2 and group 3 with cingulum*

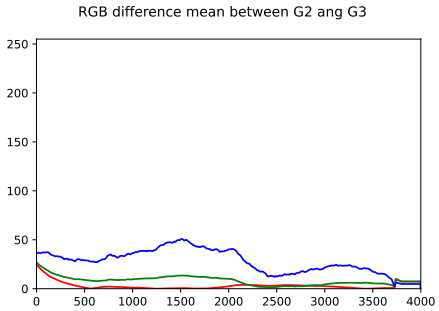

Figure D.16: *RGB intensity difference between group 2 and group 3 without cingulum*

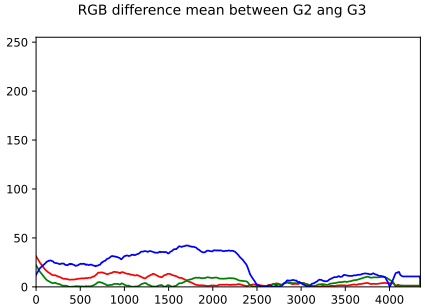

Figure D.17: *RGB intensity difference between group 2 and group 4 with cingulum*

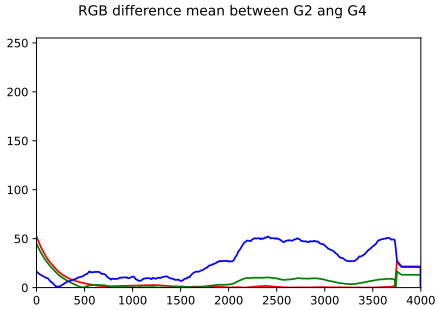

Figure D.18: *RGB intensity difference between group 2 and group 4 without cingulum*

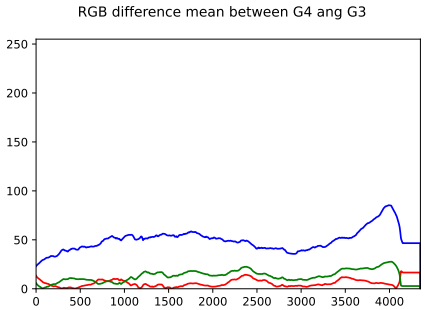

Figure D.19: *RGB intensity difference between group 4 and group 3 with cingulum*

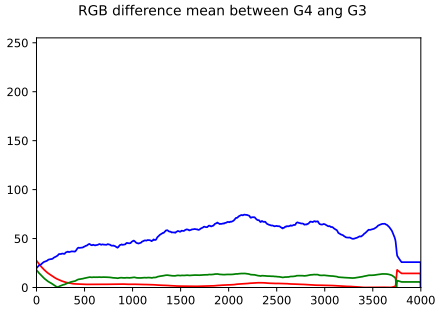

Figure D.20: *RGB intensity difference between group 4 and group 3 without cingulum*

D.2 Histology data

In Section 3.1.2, the main result was presented, i.e the minimax approximation polynomial of the mean histological data. here we will present otehr graphs that are associated to this resukts but yield smaller to no information at all. We will first start with the full signal. Not much more information can be extracted from this graph as noise phenomena induced by the nature of the data source (the image) and the type of anaylsis (pixel averaging)

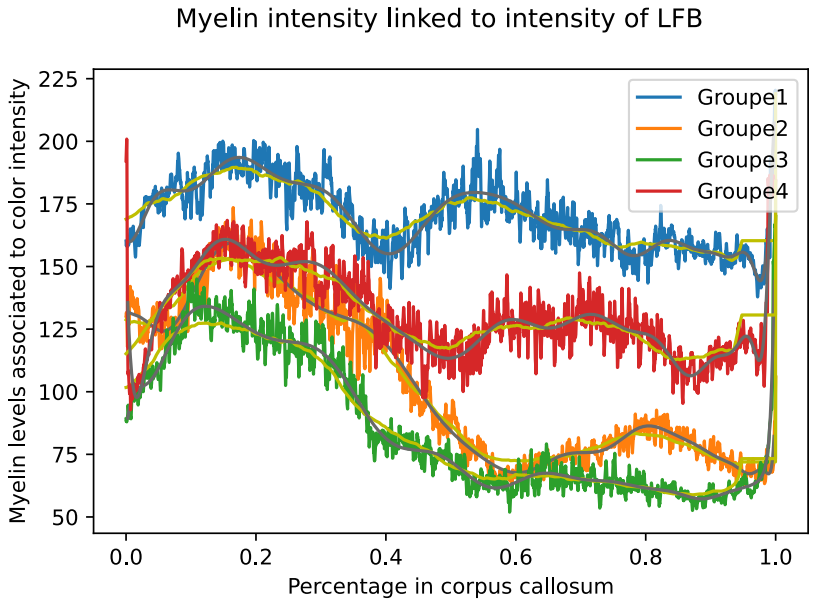

Figure D.21: *Mean histology data for each group with empiric mean in yellow and Legendre polynomial of degree 50 in gray.*

The only extra information we can extract from this graph is that the standard deviation is weak in regards to the mean. This will allow an easy interpolation (along with an approximation) of a higher order polynomial without the presence of Runge phenomena. The empiric mean depicted below is less precise than the Legendre polynomial and will yeild no information whatsoever. The empiric mean is only hear to justify the choice of selection (using Legendre polynomials).

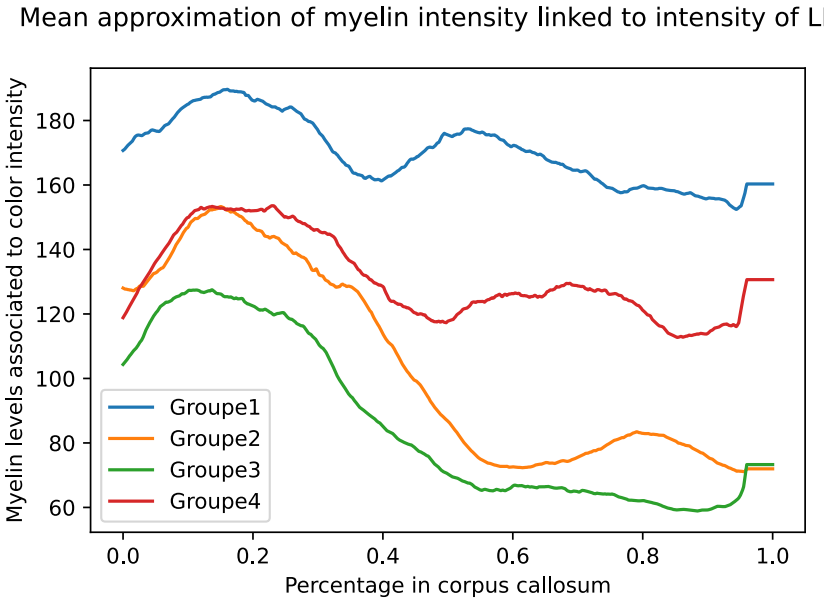

Figure D.22: *empiric averaging of the signal*

The algorithm for this method can be found right under. The idea was to find an easy way to first approximate the signal without going through tedious mathematical properties and formulae in order to get an acceptable estimation.

Algorithm 2: *Finding empirical average of the signal*

Result: $\texttt{mean}(x)$ the empirical approximation of signal $f(x)$

initialization:

Choose precision parameter n which will correspond the number of points used in the empirical mean. Let k be length of signal $y_i = f(x_i)$. Let x_i $i = 0, \ldots, k-1$ be the abcissa. $i = 0$. Let `mean` be the vector of the average

while $i \leq k$ **do**

  $\texttt{mean}(i : i+n) = \frac{1}{n} \sum_{j=i}^{i+n} f(x_j)$

end

Congratulations you've found the empirical average of the signal

We will also present the two other myelin level difference between groups. In Section 3.1.2 we discussed how there is a demyelination difference between region of the CC. The two following graphs show the difference between group 4 and groups 2 and 3 and between group 2 and group 3 respectfuly. These graphs are important as they show the anisotropic behavior of demyelination within the CC.

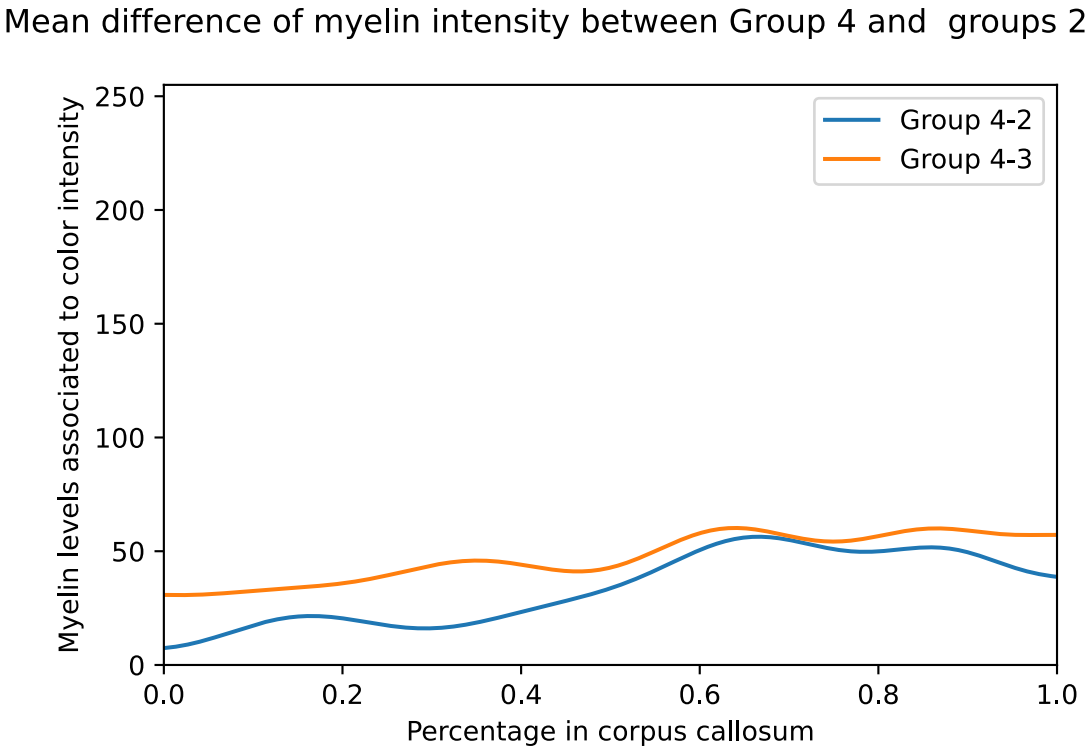

Figure D.23: *Difference in myelin levels between group 4 and groups 2 and 3 as a function of CC section*

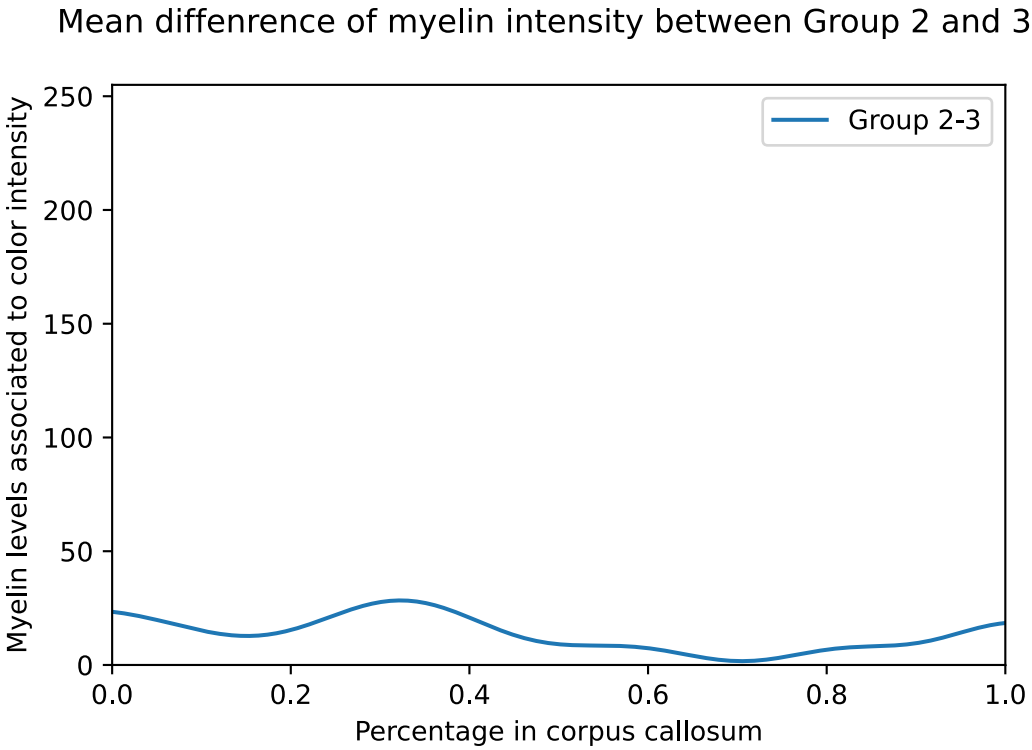

Figure D.24: *Difference in myelin levels between group 2 and group 3 as a function of CC section*

UNIVERSITÉ CATHOLIQUE DE LOUVAIN
École polytechnique de Louvain
Rue Archimède, 1 bte L6.11.01, 1348 Louvain-la-Neuve, Belgique | **www.uclouvain.be/epl**